Silesian University in Opava
Faculty of Philosophy and Science

Doctoral Thesis

Population and investigation of the light neutron rich nuclei in direct reactions

---

supervisor: Prof. Ing. Peter Lichard, DrSc.

Opava 2023   **Muzalevskii Ivan**

Annotation

The work is focused on investigation of properties of the neutron rich light exotic nuclear systems. The studied superheavy hydrogen isotopes ^{7}H and ^{6}H were populated in the direct proton transfer ^{2}H(^{8}He,^{3}He)^{7}H and deuteron transfer reaction ^{2}H(^{8}He,^{4}He)^{6}H respectively. These the most neutron-rich systems with the biggest ratio of mass over charge relate to the modern trends to investigate the most systems as close to the neutron matter as possible.

The ^{7}H states have been observed in the missing mass spectrum at the energy of 2.2(5), 5.5(3), 7.5(3), 11 MeV relative to the ^{3}H+4n threshold. The main novelty of the conducted experiment is the measurement of the triton emitted in the studied system decay, which allowed to reconstruct the momentum and angular distribution of the ^{3}H fragment with good accuracy. The analysis of the reconstructed center-of-mass angular distributions and correlations of the ^{7}H decay products allowed to identify the ground and the first excited states at 2.2(5) and 5.5(3) MeV respectively. The 5.5(3) MeV state was interpreted as the 5/2+ member of the ^{7}H excitation doublet, built on the 2^+ configuration of valence neutrons. The idea of of extreme peripheral character of the ^{7}H ground state population in this reaction was initiated by the experimental data and then also confirmed by the developed theoretical model based on the plane-wave Born approximation.

The measured ^{6}H missing mass spectrum showed a broad bump at $\approx$4–8 MeV above the ^{3}H+3n decay threshold interpreted as a resonant state at 6.8(5) MeV. The obtained missing mass spectrum was practically free of ^{6}H events below 3.5 MeV. The steep rise of the ^{6}H missing mass spectrum at $\approx$3 MeV allowed us to derive the lower limit for the possible resonant-state energy in ^{6}H to be 4.5(3) MeV, which was suggested as the ground state. The obtained results confirm that the decay mechanism of the ^{7}H ground state is the "true" (or simultaneous) 4n emission. The resonance energy profiles and the momentum distributions of fragments of the sequential ^{6}H$\rightarrow$^{5}H(g.s.)+n$\rightarrow$^{3}H+3n decay were analyzed by the theoretically updated direct four-body-decay and sequential-emission mechanisms. The measured momentum distributions of the ^{3}H fragments in the ^{6}H rest frame indicated very strong "dineutron-type" correlations in the ^{5}H ground state decay.

Key words: exotic light nuclei, direct transfer reaction, five-body decay.

Anotace

Práce je zaměřena na studium vlastností lehkých exotických jaderných systémů bohatých na neutrony. Zkoumané supertěžké izotopy vodíku ^{7}H a ^{6}H byly získány v přímých jaderných reakcích transferu protonu ^{2}H(^{8}He,^{3}He)^{7}H a deutronu ^{2}H(^{8}He,^{4}He)^{6}H. Tyto systémy s přebytkem neutronů a s největším poměrem hmotnosti k náboji souvisí s moderními trendy zkoumat co nejvíce systémů co nejblíže k neutronové hmotě.

Stavy ^{7}H byly pozorovány ve spektru chybějící hmotnosti při energii 2,2(5), 5,5(3), 7,5(3), 11,MeV vzhledem k prahu rozpadu ^{3}H+4n. Hlavním přínosem provedeného experimentu je měření tritonu emitovaného při rozpadu studovaného systému, což umožnilo rekonstruovat hybnostní a úhlové rozdělení fragmentu ^{3}H s dobrou přesností. Analýza rekonstruovaných úhlových distribucí těžiště a korelací produktů rozpadu ^{7}H umožnila identifikovat základní a první vzbuzené stavy s energií 2,2(5) a 5,5(3),MeV. Stav s energií 5,5(3),MeV byl interpretován jako vzbuzení 5/2+ izotopu ^{7}H, s 2$^+$ konfigurací valenčních neutronů. Interpretace extrémního periferního charakteru vzniku základního stavu ^{7}H v této reakci byla navržena na základě experimentálních daty a poté potvrzena i vyvinutým teoretickým modelem pomocí Bornovy aproximace rovinné vlny.

Naměřené spektrum chybějící hmotnosti ^{6}H ukázalo široký pík s energií ≈4–8 MeV nad prahem rozpadu ^{3}H+3n, který byl interpretován jako rezonanční stav na 6,8(5),MeV. Získané spektrum chybějící hmotnosti ^{6}H bylo prakticky prázdné pro energie méně než 3,5,MeV. Strmý nárůst spektra chybějící hmotnosti ^{6}H na ≈3 MeV nám umožnil odvodit dolní limit pro možnou energii rezonančního stavu v ^{6}H, který byl navržen jako základní stav s energií 4,5(3),MeV. Získané výsledky potvrzují, že mechanismus rozpadu základního stavu ^{7}H je "pravý" (true) 4n emise. Rezonanční energetické profily a rozdělení hybností fragmentů postupného ^{6}H→^{5}H(g.s.)+n→^{3}H+3n rozpadu byly analyzovány pomocí teoreticky aktualizovaných mechanismů přímého rozpadu čtyřčásticového systému a postupné emise částic. Naměřená rozdělení hybnosti fragmentu ^{3}H v těžišťové soustavě ^{6}H ukázala velmi silné "dineutronové" korelace v rozpadu základního stavu ^{5}H.

Klíčová slova: exotická lehká jádra, přímá reakce přenosu, pětičásticový rozpad.

SLEZSKÁ UNIVERZITA V OPAVĚ

Filozoficko-přírodovědecká fakulta v Opavě

ZADÁNÍ DISERTAČNÍ PRÁCE

Akademický rok: 2022/2023

Zadávající ústav: Ústav fyziky

Student: Mgr. Ivan Muzalevskii

UČO: 52074

Program: Fyzika (čtyřletá)

Obor: Teoretická fyzika a astrofyzika

Téma práce: Population and investigation of the light neutron rich nuclei in direct reactions

Téma práce anglicky: Population and investigation of the light neutron rich nuclei in direct reactions

Zadání: Doktorská dizertační práce se zaměřuje na detailní studium izotopu ^{7}H, který je získán v reakci ^{8}He(d,^{3}He)^{7}H (při energii svazku ~25 MeV/A) s následným pětičásticovým rozpadem ^{7}H –> ^{3}H+n+n+n+n. Cílem práce je analyzovat spektrum chybějící hmotnosti z ^{3}He a korelace rozpadu ^{7}H. K dosažení těchto cílů je nutné vytvořit teoretický model, který popisuje účinný průřez reakce a porovnat ho s experimentálními daty. Tato práce přispěje k hlubšímu porozumění izotopu ^{7}H získaného v reakci ^{8}He(d,^{3}He)^{7}H s následným pětičásticovým rozpadem a přinese nové poznatky o struktuře a vlastnostech tohoto izotopu. Vývoj detekčních metod pro identifikaci neutronů přispěje k lepšímu měření a charakterizaci neutronových korelací v rozpadu ^{7}H. Srovnání teoretického modelu s experimentálními daty umožní ověřit a upravit současné teoretické představy o účinném průřezu reakce.

Literatura: A. A. Korsheninnikov, E. Yu. Nikolskii, E. A. Kuzmin, et al., Experimental evidence for the existence of 7H and for a specific structure of 8He. Phys. Rev. Lett., 90:082501, Feb 2003.
E. Yu. Nikolskii, A. A. Korsheninnikov, H. Otsu, et al., Search for 7H in 2H+8He collisions. Phys. Rev. C, 81:064606, Jun 2010.
M. S. Golovkov, L. V. Grigorenko, A. S. Fomichev, et al., Estimates of the 7h width and lower decay energy limit. Phys. Lett. B, 588:163, 2004.
Yu.B. Gurov, B.A. Chernyshev, S.V. Isakov, et al., The European Physical Journal A, 32(3):261–266, 2007.

Vedoucí práce: prof. Ing. Peter Lichard, DrSc.

Datum zadání práce: 17. 5. 2023

Souhlasím se zadáním (podpis, datum):

....
RNDr. Tomáš Gráf, Ph.D.
vedoucí ústavu

Declaration

I herewith declare that I worked on this thesis on my own and that I used only sources mentioned in the Bibliography section. My principal contributions of this thesis were as follows.

- Participation in development the framework dedicated to the simulation, reconstruction, data acquisition, and analysis. Preparation works for both experiments: construction the neutron spectrometer, configuration the software for the data acquisition of the whole setup. Participation in all experimental runs.

- Development the calibration methods of all detectors and determination their properties (dead layer values, silicon detectors maps of thicknesses). Implementation of them into the developed framework. Based on the results of these works, the article *[I.A. Muzalevskii, et al., Bulletin of the Russian Academy of Sciences: Physics, 84:500–504, 2020.]* was published.

- Processing and analyzing the collected data. Experimental results interpretation. Comparative analysis of the experimental results to the earlier published works. Calculation the reaction kinematics. Development and performance the reaction cross-section calculations, using the theoretical model, based on the plane-wave Born approximation. Writing and publication the articles: *[A. A. Bezbakh, et al., Phys. Rev. Lett. 124, 022502 (2020)]*, *[I.A. Muzalevskii, et al., Phys. Rev. C, 103:044313, Apr 2021]* and *[E. Yu. Nikolskii, et al., Phys. Rev. C, 105:064605, Jun 2022]*. Participation in the establishment of a platform for future experiments at ACCULINNA-2.

Opava, May 20th, 2023 . . . .

Mgr. Ivan Muzalevskii

Acknowledgements

Contents

1 Introduction

The object of nuclear physics investigations is in a link with the topic of a few-body system of strongly interacting fermions. Although, the latter mostly consists of just neutrons and protons (nucleons), the limits of such investigations are very far up to date. However, more than three thousand proton-neutron configurations, isotopes, have been already discovered. And one cannot speak about the exact number of them, because it is continuously growing, adding 2-20 new species each year. The theoretical estimation predicts that from 2000 to 3000 other nuclear systems can be synthesized [1].
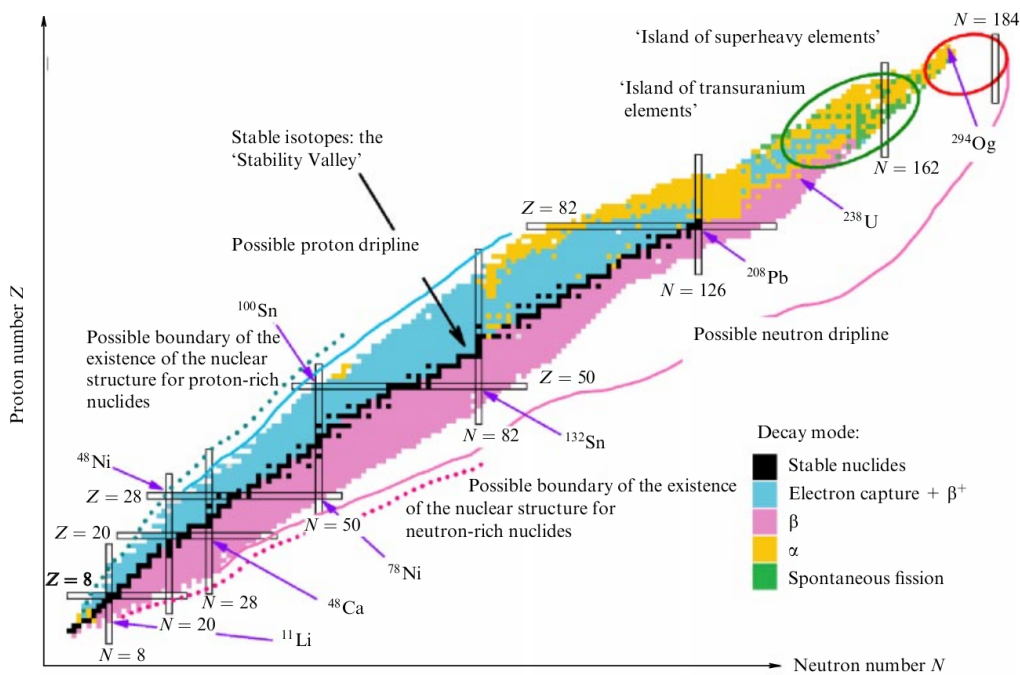
Figure 1: Illustration of global structures in the nuclear chart. The chart of nuclides is an analog of the periodic table for nuclear physics. Vertical and horizontal bands indicate the "magic" numbers corresponding to the number of protons Z and the number of neutrons N. Some "special" nuclides are indicated by arrows: ^{11}Li - a nuclide with one of the most developed "Borromean" two-neutron haloes, the double-magic nuclides in the long isobaric chains; ^{294}Og is the heaviest nuclide known today.

It is known that there are 243 stable nuclei, but in nature one can find about 339 [1]. That means, that some of them are unstable with respect to $\alpha-$, $\beta-$decay or fission (for heavy elements), but they are still bound and live long enough to come down to us from the early universe, or are products of different reactions. Bound nuclear systems are defined by means of single or multiple nucleon separation energy. At some point it becomes energetically favorable to emit one or several nucleons. Such systems are called unbound. The borders between bound and unbound nuclear systems are called driplines, illustrated as colored solid lines in Fig. 1.

Here we should draw the line between the concept of radioactivity and decay. Radioactivity is the phenomenon, related to the atomic systems, which implies the atomic orbitals formation. That is why, the term radioactivity can be used only for systems, living long-enough to form

the electron orbitals (10^{-15} s), while the decay concept applies to the pure nucleon systems. Nucleon structures, located beyond the driplines, exist as resonances having shorter lifetimes. In this work, all the nuclear system, located in the vicinity and beyond the driplines, will be referred to as exotic nuclear systems or exotic nuclei. Usually, the more exotic the system is, the less is its lifetime, which makes such studies more challenging. That is why the location of the driplines was experimentally obtained only for the light nuclei [2]. And moreover, so far there is no answer to a fundamental question about the limits of the nuclear structure: whether the border between unbound nuclear systems and continuous spectra exists? And where such line, beyond which no resonances can be found, is located?

Exotic nuclei differ from the stable not only in mass over charge ratio, but also in the unique phenomena exist here. Halo and skin effects, the difference of magic shell numbers, the new types of excitation and radioactivity make some standard nuclear structure models inapplicable for the description of such unstable systems.

- One can imagine the cluster-core, surrounded by the valence nucleons with smaller separation energy. It leads not only to the abnormally large nuclear radius, see Fig. 2, but to the other anomalies, such as the increase of the reaction cross section narrow momentum distribution of the valence nucleons, etc. For the fist time, the term "halo" was used in Ref. [3], but by the present day, it is well known, that such exotic feature was observed in many neutron-rich (^{6}He, ^{11}Li, ^{17}B, ^{19}B, ^{22}C) and neutron-deficient systems (^{8}B, ^{13}N, ^{17}Ne, ^{26}P, ^{27}S) [4]. In some neutron rich nuclei, for example ^{8}He, valence neutrons form the so-called neutron skin. Such systems are characterized by the increased size, caused by a layer of neutrons on the surface of a nucleus. But it turned out, that the systems with neutron skin are more compact than neutron halo-nuclei, see Fig. 2. ^{8}He is a well known example of the light isotope with neutron skin [5].

- In weakly bound neutron-rich systems, the pairing interaction in conjunction with the valence nucleon excitations invalidates the traditional two-body problem for the nucleon motion and leads to the appearance of new collective modes [6].

  The spatial transformations of nucleons lead to the new degree of freedom, the so-called soft dipole excitation mode, which can be described as the oscillation of the valence nucleons with respect to the core cluster. Such excitation type can be discussed as a low-energy split-off from the giant dipole resonance, which is the collective oscillation of all protons against all neutrons in a nucleus. The scope of the soft dipole excitation phenomenon is smaller, and therefore more difficult to be observed. However, those excitations may play unexpectedly important role in the nuclear astrophysical applications.

- Some core-halo nuclear systems may represent the so-called "Borromean nuclei" named after the Borromean rings - the mathematical object consisting of three topologically linked curves, which cannot be separated, except for the case without any binary link between each other. Removing any part of it, one disintegrates the whole system. In other words, a Borromean nucleus is bound only as many-body system, while all its
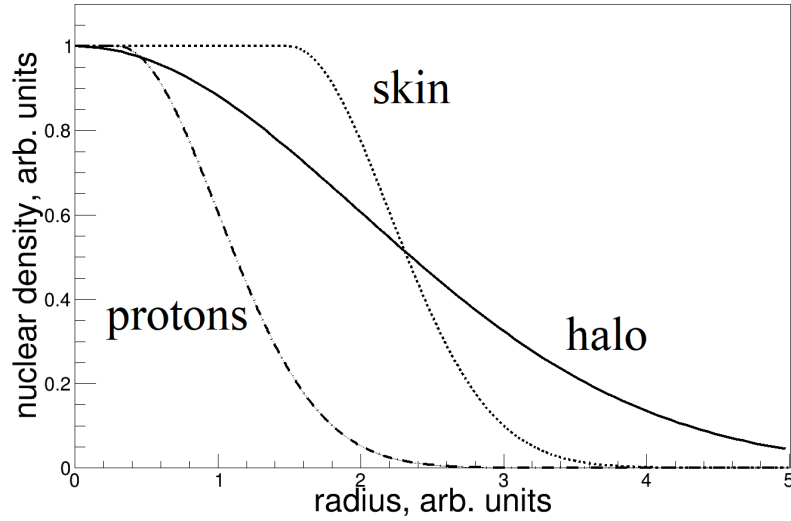
Figure 2: Illustration of nuclear matter density for nuclear halo and skin. Density of proton matter is depicted by dashed-and-dot line; nuclear skin presented by dashed line is characterized by larger radius than core matter; and matter distribution of nuclear halo depicted by dotted line is less compact and more spread in comparison with nuclear skin. Haloes are typical for 1-2-4 neutrons separated from the core, while skins are for the heavy nuclei with large neutron asymmetry.

subsystems are unbound (see review Ref. [7]). This leads to the simultaneous many-body decays of some exotic nuclear systems, which can not occur sequentially, due to the separation-energy conditions.

Studies of the light exotic nuclear systems play a particularly significant role in the modern nuclear physics. The small number of nucleons in light isotopes allows to highlight the contribution of the studied phenomena effects to other processes. This is extremely convenient for the reactions of exotic system production characterized by low cross sections. On top of that, in the light isotopes the extreme mass-over-charge ratio can be reached. These short-lived systems are usually characterized by many-body decay channels.

Investigation of such simultaneous many-body decays is the only way to get experimental information about the many-body capture processes, which can be considered as the time reversal reactions to the observed decays. These processes may occur only under extreme conditions of very high temperatures and densities, that is why the investigations of exotic nuclear systems may have a significant contribution to astrophysics. The role of rare isotopes in astrophysical environments, is described in details in [6], which shows the application of the nuclear experimental techniques to the modern astrophysical tasks and objects of interest (novae, supernovae, s and r process, occurred in compact objects, X-ray bursts, the problem of neutron matter, etc.) One of the example is study of the neutron-deficient systems in the vicinity of the proton dripline, which can be an instrument to study the nucleosynthesis of fast proton-capture, so-called rp-process, occurred on the surface of a neutron stars of hydrogen burning reactions [2, 8, 9, 10, 11]. The features of this rp-process at waiting points, where the single proton capture is forbidden, can be explored using the phenomenon of multi-proton decays [12]. On

3

the other hand, the rapid neutron-capture process, also known as the r-process, proceeds along the neutron dripline in supernova core-collapse processes. It is similarly studied in reactions with neutron-rich isotopes. Therefore, the investigation of multi-nucleon emitters is a good test for developing theoretical models, which are supposed to provide the equation of state of the nuclear matter at extreme conditions.

1.1 Experimental techniques for exotic nuclear research

Due to the short lifetime, exotic nuclei can not be found in nature. And even with modern technologies, studies of such abnormal systems is a great technical challenge due to low cross sections of the reactions of interest, extremely short lifetimes of the systems of interest and overwhelming production of unwanted species at the same time. New isotopes can be products of either the direct nuclear reactions or the compound-nuclear decays.

The compound nucleus is formed as a result of slow-collisions occurring at the so-called adiabatic conditions [13]. In such collisions the target-projectile relative speed is incomparable to the Fermi momentum (the momentum of a nucleon within the nucleus), which allows to share the total energy of projectile and target among the numerous nucleons of the compound system. In such **fusion reactions** the compound nucleus system with N+Z combination, approximately equal to the sum of the numbers of protons and neutrons in the initial beam and target nuclei, is produced. Due to the increasing asymmetry of mass over charge for heavy nuclei, such reaction mechanism is commonly used in studies of neutron-deficient isotopes. If the compound nucleus has too much energy to be stable, it decays into two or many fragments, and thus can produce nuclei with big mass-charge asymmetries.

At the opposite extreme are the direct nuclear reactions, in which the projectile interacts with only few fragments of the target, involving only small number of degrees of freedom. All direct reactions are characterized by the transfer momentum of the highlighted orientation, along which the alignment is formed. The direction of the transfer momentum vector is also used in Treiman-Yang criterion, one of the most powerful experimental tests for verifying the pole approximation prediction [1]. Here, we want to list the most common direct reaction mechanisms used in studies of exotic nuclear systems.

- **Pickup or stripping transfer reactions** are widely used mechanisms, especially for light system research, in which the beam exchanges the nucleons with a target. Stripping is transfer from the projectile to the target, and pickup from the target to the projectile [14].

- In the **knock-out reactions**, the isotopes can be produced in a single nucleon or a light cluster removal process from the projectile by a collision with the target [15].

- In order to obtain exotic nuclei, the **charge-exchange reactions** can be applied. In these reactions predominantly the ground state of exotic product is populated by replacing of one or two protons (neutrons) with neutrons (protons) [16].

Direct reactions occur with high probability with light particles, and can be easily identified. Due to the very small amount of involved degrees of freedom, only few final states of the studied system can be populated, which makes experiments with such reactions one of the best tools to selectively study the properties of specific states.

This thesis is devoted to studies of light neutron-rich exotic nuclear systems, primarily super-heavy hydrogen isotopes ^{6,7}H, produced in direct transfer reactions induced by the radioactive ^{8}He beam obtained at the ACCULINNA-2 fragment separator. The high quality secondary beam of the light neutron excess isotopes allows to synthesize the systems with the biggest ratio of mass over charge, approaching the neutron matter study [17]. This huge unique asymmetry allows different exotic features described above to be observed by the developed experimental techniques.

2 Historical overview: light neutron-rich systems

Search for the limits of existence of unbound neutron-rich systems is one of the main trends in modern nuclear physics. Probably, the most significant recent results in this field are the works on ^{7}H, ^{10}He [18, 19, 20, 21], ^{13}Li [22, 23], ^{16}Be [24], ^{21}B [25], ^{26}O [26, 27, 28] and the on-going quest for ^{18}Be, ^{28}O, ^{33}F [29] (and analogous very exotic species). One can find that these experiments, requiring extreme technical efforts, nevertheless, often suffer from the poor data quality, characterized by the low statistics, poor resolution and, consequently, the numbers of unresolved data-interpretation questions. One can also find conflicting results, related to the same exotic nuclear system, see, e.g. the heavy helium cases in review works [1, 30]. The typical feature of such systems, close to the neutron dripline, is the multineutron (at least two-neutron) emission. And of course, among all the neutron rich nuclear systems, ^{6,7}H being the isotopes of the lightest chemical element, draw the attention of physicists because of their biggest neutron-to-proton ratio which can be imagined.

2.1 ^{7}H studies

The ^{7}H structure is the closest one to the neutron matter, which makes it the key isotope among all neutron rich systems. The first prediction of the ^{7}H existence was made more than 50 years ago [31]. The authors performed the first theoretical estimations coming to the prediction that the ^{7}H nucleus could be even bound.

Few experiments, dedicated to search for the long-lived ^{7}H were conducted. We mention the attempts to produce this system in the pion double charge-exchange reactions, described in works [32, 33]. Although such technique was effective to populate and identify the ground states of ^{8,9}He, it only allowed to obtain the cross-section limits for the population of both ^{5}H and ^{7}H. The sophisticated approach was used in the work [34] dedicated to the search for the long-lived quasistable ^{7}H. Speculative suggestions about the ^{7}H decay energy and lifetime led to the assumption of possible existence of ^{7}H having very low (50-100 keV) decay energy. The estimated lifetime of such state would exceed 1 ns, and therefore could be measured directly. The experiment was conducted at ACCULINNA fragment separator with a beam of 20.6 AMeV ^{8}He and very thick (5.6 cm) liquid deuterium target. The ^{7}H nuclei, supposed to be produced in the ^{2}H(^{8}He,^{3}He)^{7}H reaction within $0° - 50°$ c.m. angular range, were assumed to be detected by the ΔE-E assembly located behind the target. The absence of detected ^{7}H events with lifetime less than 1 ns gave a limit for the cross section of the ^{2}H(^{8}He,^{3}He)^{7}H reaction, $\sigma < 3$ nb/sr, which is by several orders of the magnitude less than the expected value. The lifetime estimates made in Ref. [34] led to the conclusion that the obtained limit of the ^{7}H production cross section implies a lower limit of $E_T \gtrsim 50 - 100$ keV for its decay energy (here and later we denote the system excitation energy above the decay threshold as E_T).

The observation of the ground state resonance in ^{5}H [35] revived theoretical interest to the possible existence of a low-lying ^{7}H state near the ^{3}H+4n decay threshold. And on top of that, the population of the ^{5}H ground state in the proton transfer reaction ^{1}H(^{6}He,^{2}He)^{5}H pushed to

use the same reaction mechanism and ^{8}He beam in search for ^{7}H.

Calculations using the seven-body hyperspherical functions formalism [36] evaluated the ^{7}H ground state energy as $E_T \approx 0.84$ MeV. But at the same time, based on the assumption, that four valence neutrons of ^{7}H occupy the same orbitals as in ^{8}He, the simple estimations of the binding energy of the ^{7}H ground state were performed in Ref. [37]. The obtained value turned out to be ≈ 5.4 MeV, which means that this resonance state is expected at about 3 MeV above the ^{3}H+4n decay threshold. The authors also emphasized that the ^{7}H ground state should undergo the unique five-body decay into ^{3}H+4n with very small width. The experiment was aimed to search for ^{7}H in the proton transfer reaction from the 61.3 AMeV ^{8}He beam, produced by the RIPS fragment separator. Although, the experimental results of Ref. [37] did not give a chance to identify any suggested states in a structure of ^{7}H, the evidence of the ^{7}H ground state resonance near the ^{3}H+4n decay threshold was obtained for the first time. The missing-mass spectrum of ^{7}H obtained in that work showed a sharp increase starting from the ^{3}H+4n threshold. This observation was an important step towards solving the ^{7}H problem, it did not allow the authors to give quantitative information about the resonance parameters because of low energy resolution (of ≈ 2 MeV) and complicated background conditions.

We should also mention the phenomenological estimates, made in Ref. [34] pointing to $E_T \approx 1.3 - 1.8$ MeV for the ^{7}H ground state. The early pioneering theoretical works suffered from the low computation power and that is why mostly provided were the low quality estimations made by some kind of extrapolation methods. This is clearly seen in works [38] and [39] where the same approach provided $E_T \approx 7$ and $E_T \approx 4$ MeV, respectively. The authors used so-called antisymmetrized molecular dynamics and gave analysis of the dineutron correlations in heavy helium and hydrogen isotopes.

The modern attempts of search for the superheavy hydrogen isotopes in the reaction of stopped pion absorption by light nuclei, are described in works Ref. [40, 41]. In contrast to the early works [32, 33], the new approach was aimed to observe the short lived neutron-rich resonances. Although the results indicated the existence of ^{7}H as a resonance near the threshold of the supposed five-body breakup, the authors of these works concluded that the ^{7}H issue remains open.

The ^{7}H existence was investigated by the authors of Refs. [42, 43] in the transfer reaction ^{12}C(^{8}He,^{13}N)^{7}H. The authors considered the measurement of ^{13}N in the time-charge projection chamber (TPC) in coincidence with ^{3}H detection by the segmented wall of cesium-iodide (CsI) scintillator detectors. However, the obtained identification plots could not promise to perform the particle selections without risk of mix up of other elements. Although in this work only seven events could be attributed to the desired reaction channel and despite the poor ^{7}H spectrum resolution, a very narrow ^{7}H resonance was announced, with $E_T = 0.57^{+0.42}_{-0.21}$ MeV.

The authors of Ref. [44] searched for ^{7}H in the ^{2}H-^{3}He proton transfer reaction realized with the ^{8}He beam and CD$_2$ target. (Here and in the following, D$_2$ denotes ^{2}H$_2$.) The authors made conclusion that there was an indication of a ^{7}H resonance state in the measured missing-mass spectrum at $E_T \approx 2$ MeV. However, because of the narrow energy window, allowed for

the ^{7}H population, the obtained spectrum from the ^{2}H(^{8}He,^{3}He)^{7}H reaction looks very similar to the spectrum of the carbon-induced background from the CD$_2$ target. This made the authors cautious about their observations.

The next attempt to discover ^{7}H using the already traditional reaction ^{2}H(^{8}He,^{3}He)^{7}H was performed in Ref. [45] at RIKEN. The RIPS fragment separator provided the 42 AMeV secondary ^{8}He beam. The beryllium beam was used in a reference ^{2}H(^{12}Be,^{3}He)11Li reaction, used to test the reliability of the results, related to the system of interest. The energy resolution of the missing-mass spectrum, reconstructed from the low-energy recoil ^{3}He turned out to be ≈ 1.9 MeV. The obtained missing-mass spectrum, reconstructed from the detected ^{3}He recoil nuclei demonstrated a rise at low energy. However, no indication was obtained for the resonance peak revealed in the measured ^{7}H spectrum. But it gave another evidence for the low-energy ^{7}H resonance existence, close to the ^{3}H+4n decay threshold. Some peculiarity was found in the missing-mass spectrum at ≈ 2 MeV, in addition, to another one at about 10.5 MeV that could be a manifestation of the ^{7}H continuum excitation. The authors reported a value of about 30 μb/sr for the cross-section of the reaction populating the low-energy part in the ^{7}H spectrum, which, according to Distorted Wave Born Approximation (DWBA) calculations, turned out in contradiction with the announced in Ref. [42] value. The question concerning the reason of this discrepancy remained open, but in order to make the obtained results more plausible, the authors mentioned the work [39], which showed, that the admixture of dineutron components in ^{7}H is possible. Such effect doubts the assumption about the similarity of the valence nucleons in ^{7}H and ^{8}He due to a small overlap between their wave functions in the ^{2}H(^{8}He,^{3}He)^{7}H reaction, and that is why the cross-section of this reaction is small.

2.2 ^{6}H studies

The first experimental result on ^{6}H was reported in Ref. [46]. This system was searched in a "bidirectional transfer" reaction ^{7}Li(^{7}Li,^{8}B)^{6}H. Despite the poor statistics and complicated background conditions, some evidence of ^{6}H existence as a resonance at $E_T = 2.7 \pm 0.4$ MeV (above ^{3}H+3n decay threshold) was reported for the first time.

Another attempt to produce the ^{6}H resonance in the ^{9}Be(^{11}B,^{14}O)^{6}H reaction was described in Ref. [47]. The authors declared the indication of the ^{6}H existence with a low-lying resonance at $E_T = 2.6 \pm 0.5$ MeV.

There have been attempts to search for ^{6}H in the pion double exchange reaction ^{6}Li(π^-,π^+)^{6}H, [48]. However, no evidence for the ^{6}H existence up to 30 MeV above the decay threshold was found.

The theoretical description of ^{6}H is an extremely challenging task. All the methods, which successfully worked in the ^{5}H case, could not be applied for the $t + n + n + n$ system. Even the seven-body hyperspherical functions formalism, realized in Ref. [36] did not allow to estimate the ^{6}H energy, due to the computational obstacles. The only one theoretical prediction, described in Ref. [49], offered the ^{6}H decay energy 6.3 MeV. Also, similar result was obtained with the AMD approach applied in Ref. [38]. The authors evaluated the ^{6}H ground state energy

as $E_T \approx 6\,\text{MeV}$, however, both predictions did not satisfy any experimental results.

The next conducted experiments dedicated to the ^{6}H search in the reaction of stopped pion absorbtion on ^{9}Be and ^{11}B targets were described in Ref. [40]. The collected statistics allowed the authors to report the observation of few ^{6}H resonant states at E_T=6.6(7), 10.7(7), 15.3(7), 21.3(4) MeV for the first time.

Search for the ^{6}H isotope, described in Ref. [43], was performed by impinging a secondary beam of ^{8}He at 15.4 AMeV on the isobutane (C_4H_{10}) target. The ^{6}H ground state energy was assigned in this work as 2.9(9) MeV with resonance width of 1.52 MeV.

The search for the ^{6}H resonant states is an exciting challenge in itself, however, here we face two important questions related also to our understanding of the neighboring systems.

i What are the decay mechanisms of ^{7}H? For example, it could be either the true ^{7}H->^{3}H+4n decay, or sequential ^{7}H->^{5}H g.s.+2n, or, else, the ^{7}H->^{6}H g.s.+n decay, depending on the initial state of ^{7}H and ground state energies of the ^{5,6}H systems. While for ^{4}H and ^{5}H there are some relatively modern data, the spectrum of ^{6}H is too uncertain.

ii What is the decay mechanism of the ^{6}H ground state? Intuitive vision of the situation, also confirmed by the theoretical estimates of the mentioned works, predict that the ^{6}H ground state decay is likely to have a sequential ^{6}H->^{5}H g.s.+n -> ^{3}H+3n character. In such a situation, by studying the ^{6}H decay, one also gains access to the decay properties of the ^{5}H ground state.

2.3 Neutron clusters

As can be seen, the studies of neutron rich isotopes are closely linked to the multineutron system search. The first suggestion about the stability of such systems was made in works [50, 51]. Although in most of the experimental works no bound states of the neutron clusters were observed (e.g. 2n in Ref. [52], 3n in Ref. [53], 4n in Ref. [54, 55]), the issue of bound neutron nuclei existence is still addressed in the modern theoretical works, see Ref. [56, 57, 58].

Among all the hydrogen isotopes, the most promising candidate, which can be a tool for the neutron clusters studies is undoubtedly ^{7}H. In the discussion of such works, dedicated to the search for ^{7}H, as Ref. [43], the authors point out that the investigations of this isotope may be useful for the tetraneutron studies. Among the large number of works made on the 4n system, we emphasize the breakthrough work [54], which sparked the interest of this topic. Those 6 events, related to the indication of the bound tetraneutron were obtained in the breakup reaction of the 35 AMev ^{14}Be beam on the carbon target. But in parallel with the progress in radioactive beam techniques, new evidences for the 4n resonance existence appeared. The recent experimental results, reported in Ref. [55], did not confirm the preliminary claim for a bound tetraneutron. The indication of the resonance state was observed in the missing-mass spectrum following the double charge-exchange reaction of the high energy ^{8}He beam bombarding the liquid helium target. The observed peak, related to the 4n resonance, was formed from four events, lying near the four body decay threshold. These results were in agreement with the

future theoretical work [59, 58] which offered the explanation of the observed low-energy state. Nevertheless, one can see that the information about the 4n nuclear system is very limited, and requires new experiments and theoretical approaches.

Thus, in the field of light neutron-rich systems the ^{6,7}H issues remain relevant and probably the most intriguing. The accumulated experience shows that the proton transfer reactions from the radioactive neutron-rich system is the best tool for the studies of ^{6,7}H and even two or four neutron clusters. Based on the the assumption of the structure similarities of the valence neutrons in the ^{7}H and ^{8}He systems, the last results on ^{7}H of the highest quality were obtained. However, in order to solve these important tasks, the possibilities of new high-level experiments offer themselves.

3 Experiment

This work presents the results of two experiments, dedicated to the ^{6,7}H studies and one reference measurement of the same reaction mechanisms, performed to control all the setup parameters and to test the reliability of the obtained results. All the experiments were conducted at the ACCULINNA-2 fragment separator [60], recently constructed in the Flerov Laboratory of Nuclear Reaction of the Joint Institute for Nuclear Research. In this chapter, we briefly present the main features of the ACCULINNA-2 facility and describe in more details the experimental setups, employed for the investigations of the isotopes of interest.

3.1 ACCULINNA-2

The idea of the ACCULINNA-2 in-flight separator is to create, separate and transport the low-energy (from 10 to 40 AMeV) radioactive ion beams of high intensity and purity. We note, that it is not appropriate to compare its properties with those of such large in-flight facilities as FRS [61] and SuperFRS [62, 63] at FAIR, ARIS at FRIB [64], BigRIPS at RIKEN [65], or famous fragment separators using the ISOL technique [66, 67, 68]. The scientific uniqueness of the ACCULINNA-2 facility is illustrated in Fig. 3. One may see, that among all other in-flight separators, ACCULINNA-2 is able to provide the light radioactive beams of exotic nuclei with mass number <50 with energy 10-40 AMeV, which is indispensable for the certain experimental issues. The technical approach of the facility allows one to provide high quality secondary beams [60], which in conjunction with high-efficiency correlation measurements allows the user to analyse multiple kinematic conditions of the projectile and the reaction products. That is why the selection of the studied reaction channel can be carried out reliably, which, afterwards, leads to the spin-parity identification for the excitation spectra of the systems of interest.
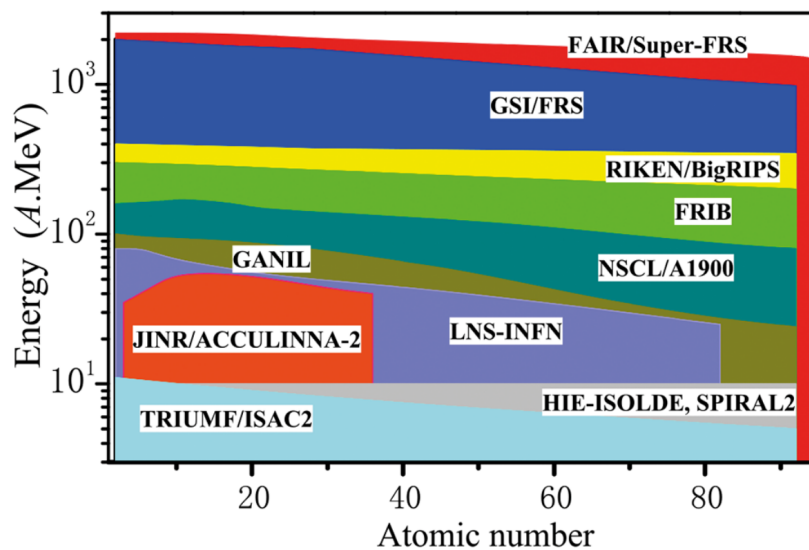

Figure 3: Landscape of the present-day facilities on the diagram where for radioactive beams, specified in terms of their atomic numbers, the available RIB energy ranges are shown.

The ACCULINNA-2 facility is coupled to the U400-M cyclotron, which provides high intensity primary beams of ^{7}Li, ^{11}B, ^{13}C, ^{15}N and ^{18}O of energies between 30 and 50 AMeV [69]. The fragment separator ACCULINNA-2 can be also configured in a mode to form the mentioned stable beams and deliver them into the reaction chamber. It is 36 meters long, and consists of two 45-degree dipole magnets, 14 quadrupoles, eight multipoles (three octupoles and five sextupoles) and four steering magnets, see Fig. 5. The high intensity primary beams are delivered from the U-400M cyclotron to the rotating production target module installed in the first intermediate focal plane F1 to produce radioactive ion beams in fragmentation reactions via the in-flight method.

The production target module, integrates a vacuum chamber with a water cooled beryllium target mounted on a rotating disk and a set of water-cooled diaphragms. The target module is designed to work with primary beam heating power up to 2 kW. Radioactive nuclei leaving the production target are captured by the short-focusing quadrupole triplet Q1–Q3 and are transported through the magnetic dipoles D1–D2 and magnetic quadrupoles Q4–Q14 up to the final focal plane F5. The magnetic multipoles with the corresponding sextupole and octupole components are used for correction of second- and third- order aberrations occurring otherwise in the F2 and F3 planes (see in Fig. 5).

The selection of the reaction fragments is achieved by separation based on a magnetic-rigidity analysis and energy loss in the degrader material. The D1 dipole magnet filters the fragments by their magnetic rigidity B, providing dispersion at the focal plane F2. Relation between the magnetic rigidity of the first bending magnet and the A/Z number is given by $B\rho = 3.3356 \times p/q$ (here $B\rho$ units are given in T×m and fragment movement p in GeV/c). Further purification is achieved by the separation of the fragments by their energy losses in the wedge-shaped degrader. The second dipole D2 compensates the dispersion occurring in the focal plane F2 and collects the fragments at the achromatic focal plane F3. Identification of the reaction products is performed by the measurement of their time of flight and energy loss (ΔE). Both of them are measured by two BC404 plastic scintillation detectors installed at the F3 and F5 focal planes at the 12.3-meter distance, see in Fig. 5. Each scintillator is coupled with four Hamamatsu R7600-200 photomultiplier tubes. With these devices the time resolution of 100 ps can be reached, which determines the accuracy of the beam kinetic energy reconstruction. The selection, made for the thicknesses of the production target and wedge-shaped degrader in accord with the position determination, made for the momentum slits standing in focal planes F2–F5, have direct influence on the yield and purity of the required radioactive ion beam. This is typically sufficient for the production of quite pure radioactive ion beams of light neutron-rich exotic nuclei. Proton-rich radioactive ion beams need additional purification from a large amount of contamination. The reason for that is the fragmentation mechanism leading to the low-energy tails obtained in the energy spectra of the well-produced undesirable less proton-rich nuclei. Adding the velocity separation to the magnetic-rigidity analysis one can reduce the effect of this contamination. For this purpose a radio-frequency (RF) kicker is installed on the beam-line between the F3 and F4 focal planes (see in Fig. 5).
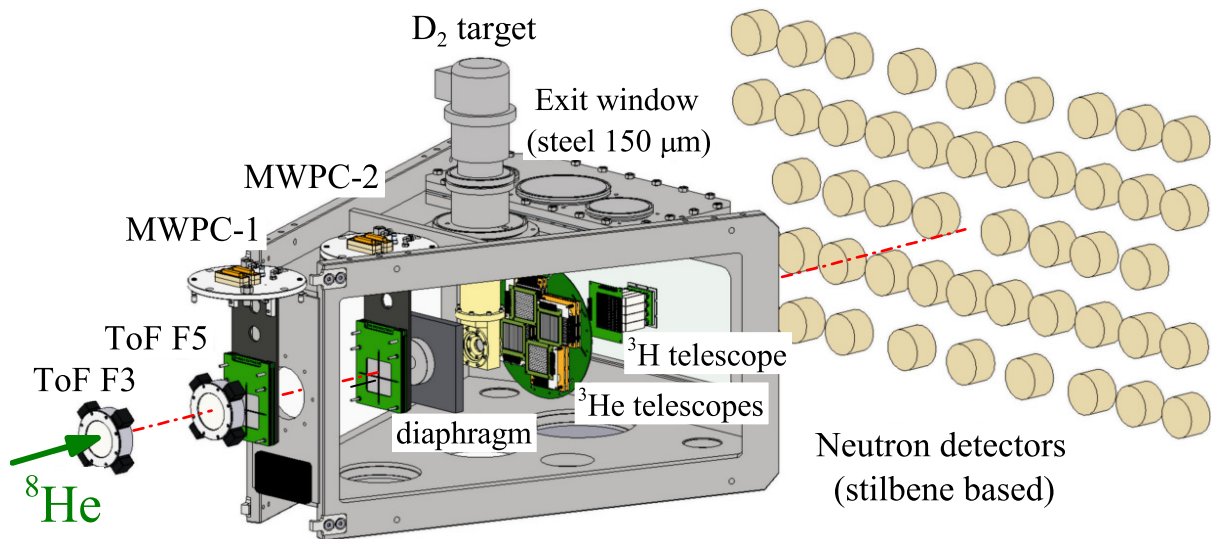
Figure 4: Experimental setup, common for the experiments 1 and 2, installed at the final focal plane F5 of the ACCULINNA-2 fragment separator. Detectors of the beam projectile positions (MWPC-1,2) and time-of-flight (ToF) are described in the text. There is no common scale along the beam axis in this plot. The telescope detectors of the reaction products are also shown in Figs. 6 and 7.

The secondary beam tracking is realized by the pair of the multi-wire proportional chambers (MWPC), illustrated in the sketch, see Fig. 4. These detectors were placed at the distances of 28 and 81 cm upstream of the experimental target, located in the reaction chamber. The MWPCs are filled with CF_4 and CH_4 gas mixture with a ratio 9 to 1 and atmospheric pressure. Each detector consists of two layers, 32 wires each, installed with interval of 1.25 mm. This allows to determine the radioactive ion interaction points in the target plane with a 1.8 mm precision. Also, this beam-tracking installation determines the inclination angles of individual radioactive ion beam projectiles to the ion optical axis with accuracy ≈ 0.15 degrees.

The desired beam (secondary radioactive or stable primary), passing through the described beam diagnostics system, reaches the stainless steal vacuum reaction chamber, located in the experimental room. The latter is well shielded by the 2 m thick concrete wall in order to get rid of the background from the cyclotron. The conditions created inside the reaction chambers allow to use the cryogenic gaseous targets (even tritium) and all the modern detector types. Moreover, the space inside the experimental hall allows to use such large facilities as the zero angle magnetic spectrometer (recently installed) and neutron detection walls. The described items make the ACCULINNA-2 facility a powerful tool for research made in the fields of light exotic nuclei near the nucleon stability borders.

3.2   Experimental setup

All the experiments were performed in the so-called inverse kinematics, which means that the studied nuclear reactions are induced by a heavy radioactive ion beam projectile colliding with the lighter target nuclei. The technique of using reversed kinematics significantly simplifies the
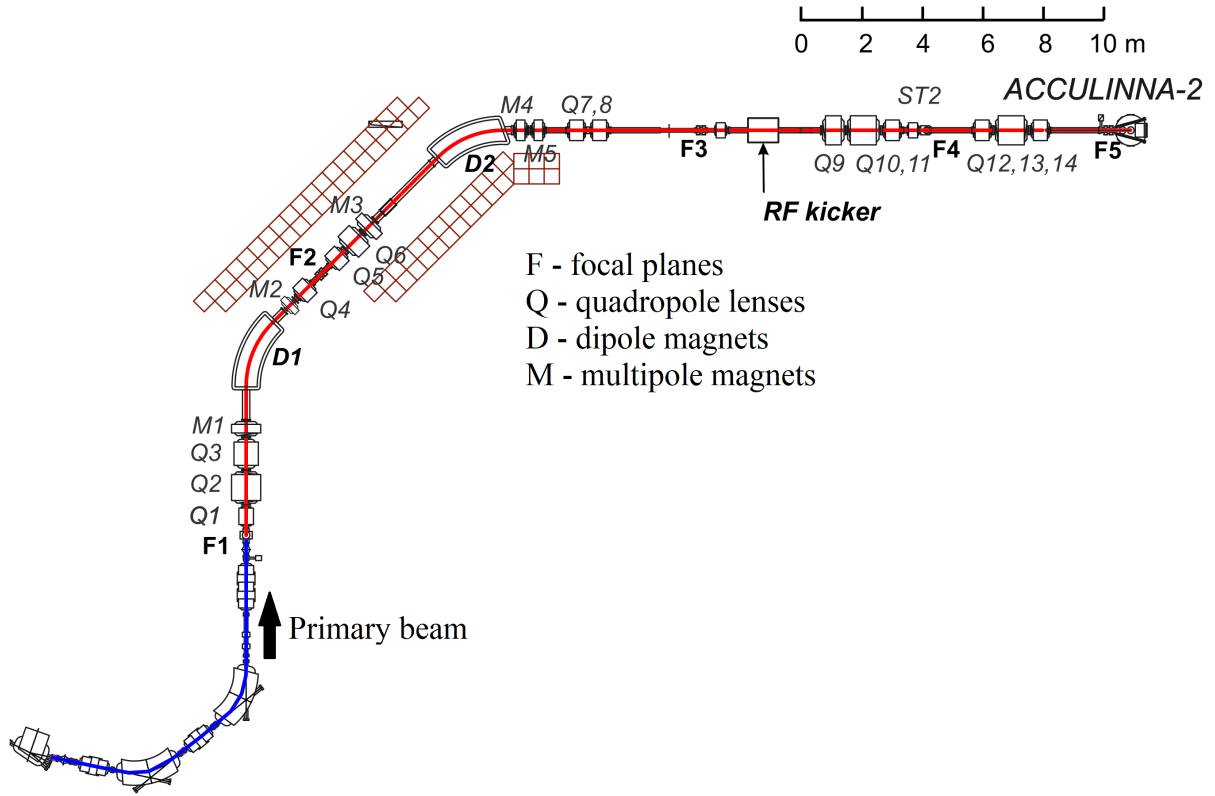
Figure 5: Lay-out of the fragment-separator ACCULINNA-2. F1 – production target installed in the primary beam focal plane; F2 – the intermediate dispersion plane; F3, F4 – the achromatic focal planes; F5 – the final focal plane.

experimental setup. In such conditions, most of the projectile's energy goes into forward motion of the reaction products in the laboratory system. That is why, mostly, all the reaction products move forward in relatively narrow cone along the secondary beam direction in laboratory frame, which in most cases, allows to detect all the products with reasonable efficiency, and therefore, to study the occurred reaction in relatively wide angular ranges.

It is well known, that in direct transfer processes, the reaction cross section has a maximum at very forward angles [15]. The concept of both experiments on heavy hydrogen isotopes investigations was to obtain a vital statistics by measuring the reaction products at very forward angles. One can find out, that this idea was one of the motivations to modify the detector system after the first experimental run, see the detector's systems schemes, described below.

3.2.1 Experiment 1

The first experiment was performed in 2018 using the ^{8}He beam with purity $\approx 90\%$, intensity $\approx 10^5$ pps and the energy in the middle target plane spread within ± 7 AMeV around the mean value 26 AMeV. This secondary beam was produced by the collision of the ^{11}B primary beam (≈ 1 pμA, 33.4 AMeV) bombarding the 1-mm thick beryllium production target. The shown in Fig. 4 target cell, 25 mm in diameter and 4-mm thick, was filled with deuterium gas (D_2) at temperature of 30 K at atmospheric pressure. Target was equipped with 6 μm thick stainless
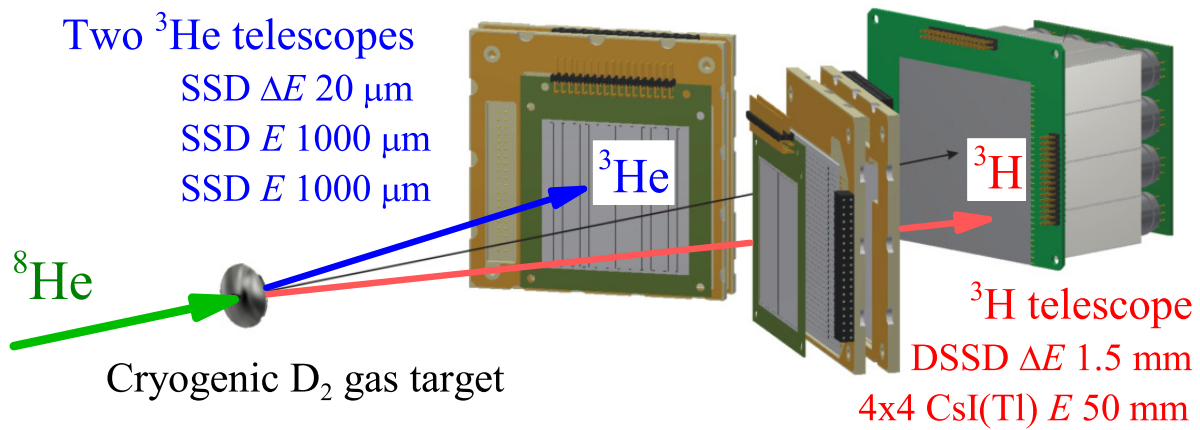
Figure 6: Charged particle detector telescopes used in the experiment 1.

steel entrance and exit windows. The cell was also concealed in a screened volume having a pair of $3.5\,\mu$m thick aluminum-backed Mylar windows and kept cooled to the same temperature to ensure thermal protection. The entrance/exit target windows, deformed by the gas pressure, took the near-lenticular form, so that the maximum target thickness turned out to be 6 mm. In the described conditions, the D_2 target thickness was $\approx 3.8 \times 10^{20}$ cm^{-2}. To ensure a homogeneous thickness of the target, only those events when the secondary beam hits the central part of the target with a circular shape of the diameter of 17 mm were taken into account. This selection ensured also the rejection of the reactions with the material of the target frame, made of stainless steel.

In addition, about 20% of the beamtime was used for the measurements with empty target. It allowed to estimate the contribution of the background random coincidences to the studied spectra. The methods of the background subtraction and scaling for the acquired spectra are described further.

For the detection of the low energy recoil particles, emitted from the target, two identical ΔE-E-E single-sided silicon strip detector telescopes were used. The telescopes allowed to measure the energy with accuracy of $\approx 1\%$ for the expected energy range and to reconstruct the emission angle of the passing particles with resolution of $\approx 1^\circ$.

Therefore, these assemblies provided high quality identification and tracking of charged particles with energies from few up to 100 MeV. The described side telescopes were located 166 mm downstream the target and covered angular range between 8° and 26° in the laboratory system, see Fig. 6. Each telescope consisted of three layers of silicon strip detectors (SSDs). The front 20-μm thick Si ΔE-SSD, had a sensitive area of 50×50 mm^2, divided into 16 strips. The pair of identical 1-mm thick (60×60 mm^2 with 16 strips) SSDs were placed on the second and third positions. In order to track the particles with such telescopes, the strips of the first (20-μm) and the second layer detectors were set to be perpendicular to each other. The third SSD was used as a veto detector to eliminate signals coming from the particles penetrating through the second layer.

Detection of the high-energy particles was realized by the central telescope, installed at the

beam line at the distance of 280 mm behind the target and covered angles $\leq 9°$ in the laboratory system. In the proton transfer reaction ^{2}H(^{8}He,^{3}He)^{7}H supposed for the ^{7}H population, it was intended to detect high energy tritons emitted from ^{7}H. This central telescope consisted of the 1.5 mm thick double-sided SSD (64 × 64 mm^2, with 32 strips on each side) followed by a square array of 16 CsI(Tl) crystals. The crystals had a cross section of 16.5 × 16.5 mm^2 and thickness 50 mm each, which allows to stop the beam and all charged reaction products in the sensitive volume of the telescope. Each crystal was covered with a 3.5 μm-thick aluminized Mylar on its entrance and was coupled with its Hamamatsu R9880U-20 photomultiplier tube by the optical grease. In order to increase the light collection and avoid the light cross-talks, each crystal was wrapped in a 100 μm-thick VM-2000 reflector.

3.2.2 Experiment 2

The second experiment, dedicated to studies of the proton transfer reaction mechanism, realized with the ^{8}He beam of the same properties as in experiment 1, and with the ^{10}Be beam with energy 42 ± 7 AMeV. The latter was used for the reference-reaction study in order to test the reliability of the obtained experimental data and to control calibration parameters and all setup configurations. These measurements were performed just after the main run with ^{8}He beam and all conditions related to the experimental setup (experiment 2) were kept the same. As for the reference reaction measurements, during 64% of the ^{10}Be beam time the target cell was filled with deuterium gas of the same properties (30 K and atmospheric pressure), 26% of this run was used for the background measurements with the empty target cell and in the rest 10%, the pressure of the target gas was decreased by factor 2. Further, we will call these runs the thick, empty and thin target measurements. The latter allowed to study the missing mass spectra with improved energy resolution, albeit at reduced target thickness and, therefore, lower statistics. More than 16% of the total ^{8}He beam time was used for the background measurements carried out with empty target cell.

The most important task of the second experiment was to increase the statistics obtained and to expand the measured angular range of the recoils to lower values in the laboratory system. For this purpose, the detector setup was modified, see Fig. 7. The new side-telescope assembly was installed at distance 179 mm from the target. It consisted of four identical ΔE-E-E telescopes made of the same SSDs as described in Section 3.2.1. The side telescopes for low energy recoil particle detection covered angular range from $\approx 6°$ to $\approx 24°$ in the laboratory system.

The high-energy particles, emitted at forward angles, were measured in experiment 2 within more narrow cone in comparison with experiment 1. For this purpose, the central telescope, the same as in experiment 1, was placed at a distance of 323 mm downstream from the target. As a result of the made modifications, considered together with the fact that the beamtime of the second experiment was ≈ 2 times longer, we could expect to increase the statistics of the reactions of interest by a factor of ≈ 2.5.

Significant advantage of the second experiment was the neutron detection, realized by the spectrometer, made of 48 organic scintillator stilbene modules [70]. The measurement of cor-
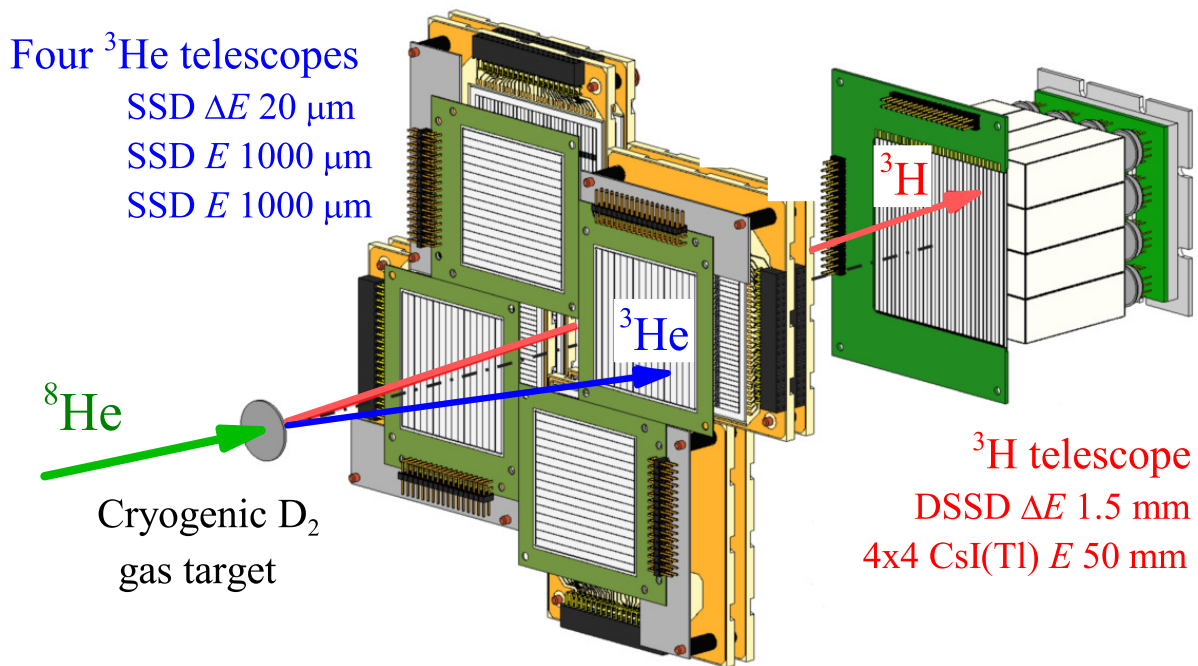
Figure 7: Charged particle detector telescopes used in the experiment 2.

relations, i.e., the detection of the neutrons in coincidences with the charged reaction products, not only allows to verify the consistency and plausibility of the obtained results but also provides unique information obtained in the study of many body decays. The spectrometer detects and identifies neutrons by measuring the light produced by the interaction of the recoil charged particles (mainly protons) within the stilbene scintillator. Its center was located at zero angle, approximately 2 meters behind the deuterium target. The distance between the neighboring stilbene modules, each module having its 8-cm diameter and 5 cm thick stilbene crystal, was approximately 12 cm, which allowed to well cover the forward angles for the neutrons emitted at the ^{7}H decay. One can see in Fig. 7, that we left empty the central area, corresponding to the most forward angles.It was made in order to avoid the beam produced signals, which are expected to be dominated for so located detectors.

The sensitive part of each module was cylinder made of stilbene monocrystal, $C_{14}H_{12}$. Each cylinder had 8 cm diameter and 5 cm thickness and was oriented by its axis to the target. Each crystal, covered with reflective MgO powder, was inserted into the 0.5 mm thick aluminum housing and connected to the photomultiplier tube by the glass window and optical grease. Two types of photomultiplier tubes were used: Philips Photonics XP 4312 and ET-Enterprise 9822B. In order to decrease the background, the photomultiplier tube-crystal systems were put into the steel tubes with 0.5 mm entrance windows. Such assembly of the stilbene crystal, a photomultiplier tube and a voltage divider in a metal case is called neutron spectrometer module and is shown in Fig. 8.
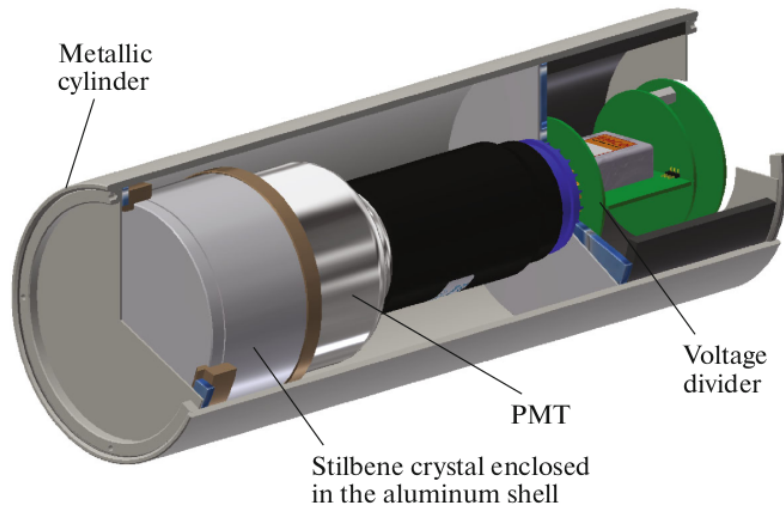
Figure 8: The 3D-model of the detecting module in the neutron spectrometer.

3.3 Data acquisition system

The signals coming from the silicon and scintillation detectors were split into the two-channel branches and processed by either constant-fraction or leading-edge discriminator. The readout system allowed to use both, the time-to-digital converter (TDC) and the amplitude-to-digital converter (ADC) for all channels of the detector system. The signals, coming from the neutron spectrometer, were also processed by the time-to-amplitude converter, which provides the data for neutron identification [70].

We used the same logic of the data acquisition, trigger formation and event building, for all conducted experiments. In order to fulfil both functions of beam diagnostic and selection of the desired events, two different triggers with "OR" coincidence logic, were used for the data acquisition. In the next chapters, we refer them as the "beam" and "experimental" triggers. If both of them were fired, the system saved the experimental trigger value. The beam trigger corresponded to those events, where any particle interacted with the ToF scintillation detector, located at F5 focal plane. Obviously, one can expect, that the beam trigger fires significantly more often than the experimental one. Moreover, the data acquisition system has its own processing time, called "busy" status, during which no new coming data can be collected. That is why the beam trigger was connected to the scaler block, which allowed to reduce the count rate of the corresponded events by a factor of 1024. The experimental trigger signal was formed by the signals coming from the second layer of the side silicon telescopes. If any of the trigger signals was fired, and the data acquisition system is not busy, the data from all connected blocks was read out by a front-end VME controller RIO4, controlled by the Multi-Branch System (MBS) data acquisition software [71]. The written data, consisted of more than 500 signal parameters, had the event structure and were stored into binary files.

4 Kinematics and simulations

As in the previous works [37, 45, 43], we assumed that the desired ^{7}H has a cluster structure of tritium core and four valence neutrons. Moreover, the idea of all our experiments was based on the assumption, that all valence neutrons of the ^{7}H ground state occupy the same orbitals as in the ground state of the ^{8}He [37], used as the secondary beam. The latter assumption did not only promise the relatively high probability of the desired system population, but also allowed us to estimate the differential cross section of the ^{2}H(^{8}He,^{3}He)^{7}H binary reaction by FRESCO code [72]. The FRESCO algorithms are based on the Distorted Wave Born Approximation applied for the d-^{3}He reaction mechanisms under the assumption that the ^{7}H ground state is populated by the one-step proton transfer from the bare ^{4}He core of ^{8}He. Similarly, the same procedure was conducted for the ^{2}H(^{8}He,^{4}He)^{6}H reaction. In this chapter we are mainly focused on the kinematics of ^{2}H(^{8}He,^{3}He)^{7}H reaction and the subsequent 5-body decay of ^{7}H, because the original idea of the ^{8}He+^{2}H experiment was the population low-energy ^{7}H states, and the deuteron transfer was a satellite reaction channel. The multiplier factors 1.45 and 1.3 were assumed for getting Woods-Saxon potential radii of ^{7}H and ^{2}H, respectively, with the diffuseness factor 0.55 taken for the both potentials. The potential strengths were adjusted to match the proton bounding energies in ^{8}He and ^{3}He. On the basis of data given in Ref. [73] the proton spectroscopic amplitude of ^{8}He was taken SA = $\sqrt{2}$, as it is for ^{4}He, and SA = $\sqrt{1.5}$ was assumed for ^{3}He. The entrance-channel (^{8}He+d) optical model parameters were obtained on the ground of data given in Ref. [74], and the exit-channel (^{7}H+^{3}He) ones were taken from the appropriate case given in Ref. [75].
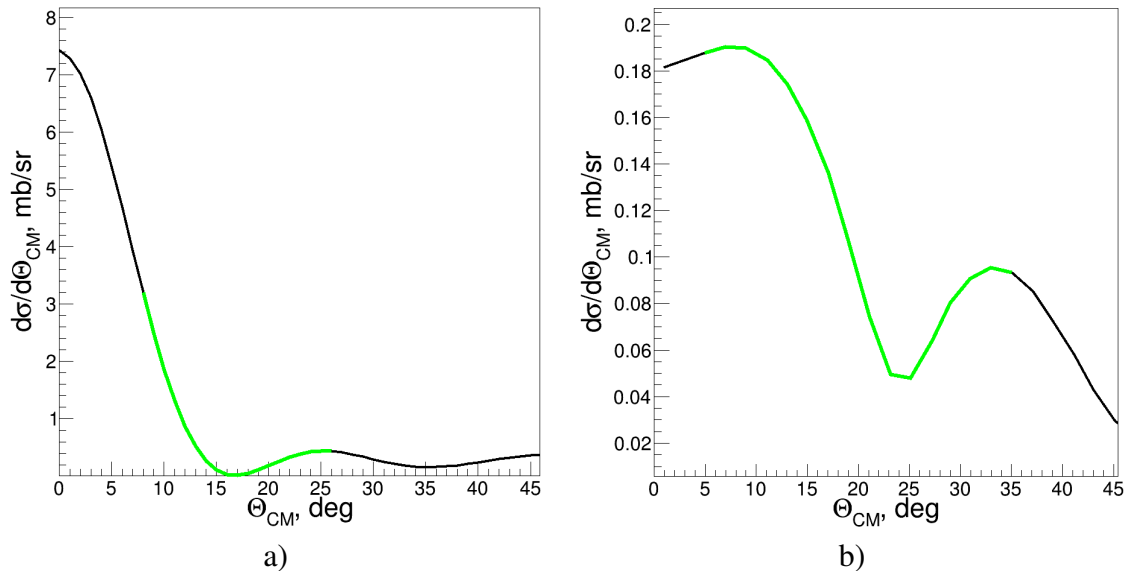
Figure 9: Angular distribution obtained by FRESCO code calculations for both ^{2}H(^{8}He,^{3}He)^{7}H(g.s.) a) and ^{2}H(^{8}He,^{4}He)^{6}H with the $\Delta l = 1$ b) reactions. On both panels green color refers to the angle areas covered by the side telescopes.

The calculated angular dependence of the one-step ^{2}H(^{8}He,^{3}He)^{7}H reaction differential cross section, populating the ^{7}H ground state, is shown in Fig. 9 a). When the optical model parameters were varied within 10-percent limits the position of the first cross-section minimum

changed within 1.5°. A similar alteration of this minimum was obtained with the optical model parameters taken from the compilation [76]. The variation of the mentioned input parameters did not result in an appreciable change of the position obtained for the second diffraction maximum of the ^{2}H(^{8}He,^{3}He)^{7}H (g.s.) reaction. The relevant calculations performed for the ^{7}H excited states assumed their two-step production going through the proton transfer from the ^{8}He(2^+) state appearing due to the collective [$\beta(2^+) = 0.45$] excitation.

Similar method was used for calculation the ^{2}H(^{8}He,^{4}He)^{6}H, $\Delta l = 1$, reaction cross-section. The result is shown in Fig. 9 b). The cross section features a broad peak at about $\theta_{c.m.} \sim 8°$, the rapid fall after $\theta_{c.m.} > 14 - 16°$, and the diffraction minimum around $\theta_{c.m.} \sim 24°$.
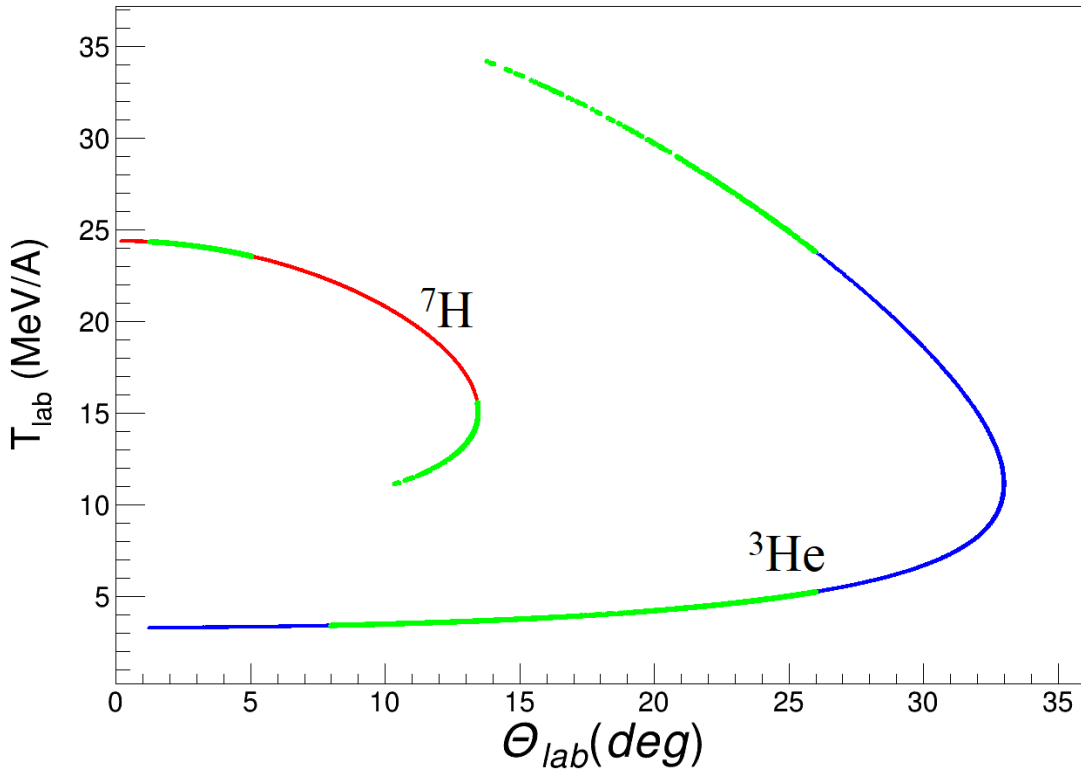
Figure 10: Dependence of the kinetic energy per nucleon of the ^{7}H and recoil ^{3}He on the angle in the laboratory frame of reference. The red and blue curves relate to the ^{7}H and ^{3}He respectively. Green color refers to the angle areas covered by the detectors.

For the studied binary reaction ^{2}H(^{8}He,^{3}He)^{7}H and the expected decay ^{7}H$\rightarrow^3$H+4n the kinematic calculator software was used [77]. The latter was configured to be able to calculate kinematics of both binary reactions and many body decays. As far as the many body kinematics (5 body decay of ^{7}H in our case) represents the complicated mathematical problem, the kinematics algorithms were based on the Monte-Carlo methods. The developed calculator allowed to adopt all necessary input parameters, such as the reaction angular distributions, nuclear mass distributions, including the corresponding excitation level schemes, etc. First, as for the binary proton transfer reaction, the masses of all known particles (^{8}He, ^{2}H and ^{3}He) were taken in consideration in their ground states and taking the corresponded binding energy values from the National Nuclear Data Center [78]. The mass of ^{7}H was calculated as excitation energy above

the mass of the ^{3}H+4n system. The corresponding excitation energy was randomly generated for each event and adopted by the Monte Carlo algorithms of the kinematic calculator. Taking into account the angular distribution, obtained by FRESCO, Fig. 9, the ^{2}H(^{8}He,^{3}He)^{7}H reaction kinematics was calculated, by the well known binary reaction kinematics equations, see Ref. [79]. The results are presented in Fig. 10. The latter shows that at all angles covered by the detector setup, the recoil ^{3}He particle should be expected at relatively low energies (from 9 to 15 MeV) in laboratory frame of reference. That is why the side telescopes, intended for tracking, identification and reconstruction of the recoil nuclei, had very thin silicon strip detectors in the first layer (claimed $\approx 20\,\mu$m by the manufacturer). As for the short-lived ^{7}H, it moves at forward angles with higher energies (up to 175 MeV, Fig. 10), and according to Ref. [34], decays before leaving the target volume, and is measured indirectly by means of detection of its decay products. The latter, moving forward along the ^{7}H direction in narrow cone which is shown in Fig. 11. These calculations were based on works [80, 81] and realized with Monte Carlo algorithms, applied for the 5-body phase space distributions of the t+4n decay products.
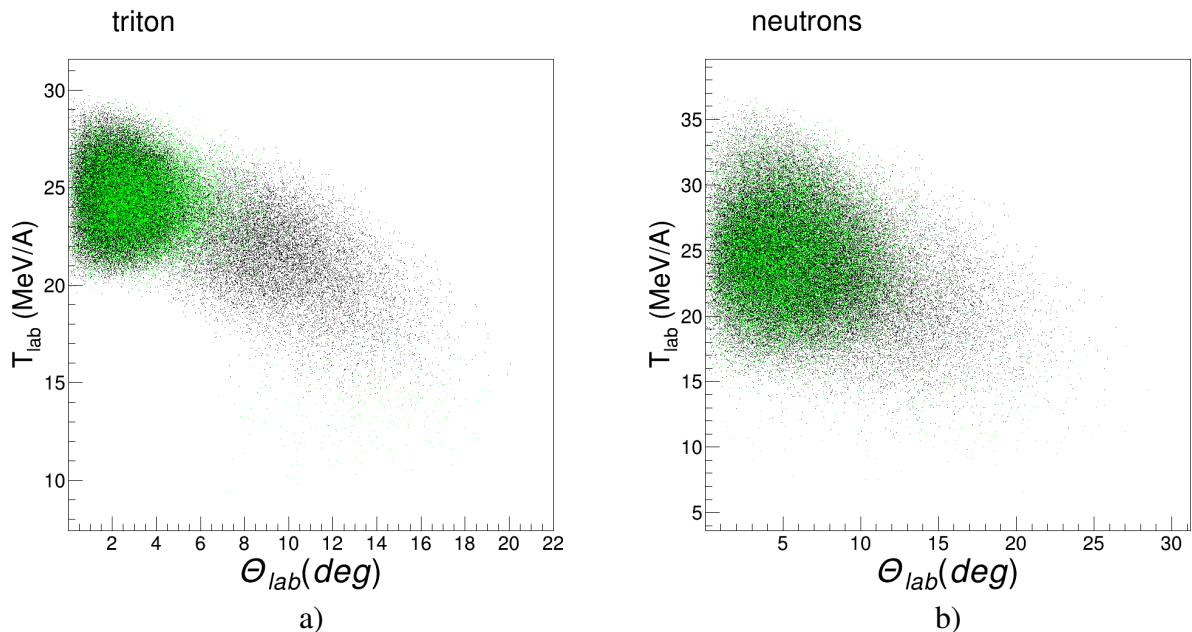
Figure 11: Kinematic correlations of energies with the angle in lab for tritons (left) and neutrons (right). Green color refers to the angle areas covered by the detectors.

The presented kinematics shows that the used detector system geometry is the most appropriate for revealing all reaction products and thus promises the high detection efficiency of double t-^{3,4}He coincidences and admissible probability of neutron registration.

4.1 Experimental resolution

The complete Monte-Carlo simulations of the experimental setup were performed and extensively used in the interpretation of the data. Here we address the question of experimental resolution. Fig. 12 shows Monte-Carlo simulations for the center-of-mass angle distributions of the binary reaction (θ_{cm}) vs. ^{7}H excitation energy (E_T) defined by the product of δ-functions

at the corresponding energy and angle. The projections of the plotted structures either on the energy or the angle axis reflect the respective resolutions at a certain place of the kinematical plane, see Table 1. It is possible to find out that at $\theta_{cm} \to 0$ the *energy resolution* is defined mainly by the target thickness. The relative importance of this factor decreases with the increase of the ^{7}H energy E_T taken above the ^{3}H+4n decay threshold: the energy resolution varies from ~ 800 keV at $E_T = 2.2$ MeV to ~ 250 keV at $E_T = 14$ MeV. The *angular resolution* at $\theta_{cm} \to 0$ is defined by the beam tracking precision and granularity of the ^{3}He telescopes. It is clear from Fig. 12, that for large θ_{cm} the Monte-Carlo "spots" are tilted and, thus, both the energy and the angular resolutions aggregate the two mentioned factors. Consequently, the best resolution for the ^{7}H g.s. missing-mass energy is obtained for small center-of-mass reaction angles, and for the larger angles it considerably degrades.
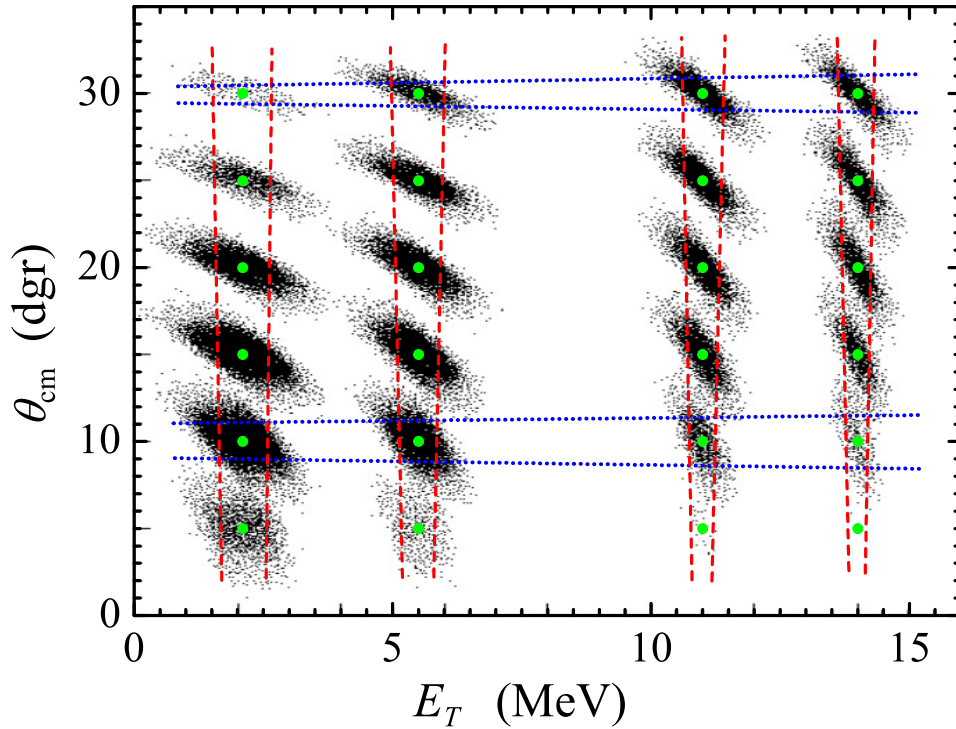
Figure 12: The Monte-Carlo simulations demonstrating the experimental resolution for the ^{2}H(^{8}He,^{3}He)^{7}H reaction of the second run. The simulations are performed for a set of fixed center-of-mass reaction angles θ_{cm} and ^{7}H decay energies E_T indicated by green dots. The red dashed lines guide an eye along the contours defining the full width at half maximum for the energy resolution, while blue dotted lines do the same for the angular resolution.

Table 1: Experimental resolution in the second experiment as a function of ^{7}H excitation energy and center-of-mass angle θ_{cm} based on the Monte-Carlo simulations, presented in Fig. 12. The first and second values in each cell are the FWHM energy and angular resolutions given in MeV and degrees, respectively.

E_T	2.2 MeV		5.5 MeV		11 MeV		14 MeV	
10°	0.95	2.2	0.73	2.3	0.48	2.5	0.38	2.8
20°	1.10	1.6	0.93	1.8	0.64	2.2	0.52	2.6
30°	1.13	1.2	0.99	1.3	0.77	1.8	0.69	2.0

5 Data analysis

Data analysis consists of several important steps. First of all the collected binary files should be converted into the data of ROOT format taking into account the specifics of all readout blocks and all channel mappings. We call such converted but unprocessed files - raw data, because these files contain information about the signals in arbitrary units, channels. That is why, such data can not be physically interpreted. The recalculation of the raw data into the physical units is called calibration procedure, which is one of the largest and important methodical problems. In order to obtain the calibration parameters used for the values recalculation procedure, the special calibration measurements are conducted. Data collected in such measurements allows us also to analyse the fine properties (dead layers thicknesses, detector thickness homogeneity, channel numeration, etc.) of the corresponded detector. Irradiating the detector by the beam may cause damage to their sensitive part. Thus, assuming the possible drift of the detector properties, we performed the calibration measurements before and after the main experimental run, which allows us to make corrections for the possible parameter variations. Then, the detector background signals are cut off. Realized by the analysis are the following indicators: the time (for example signals, caused by other beam bunches, but registered inside the accepted trigger window, etc.), amplitude (noisy channels, broken strips, etc.) and tracking information (multiple hits, etc.) of all detectors. The remained signals are used for particle reconstruction, which allows to obtain the four vectors of the particles in different setup planes (detector plane, central target plane, beam interaction plane, etc.). The energy deposits are calculated by the energy deposits of the predefined particles on the determined tracks of the virtual geometry. The latter contains all information about the detector positions, peculiarities discovered in the calibration data analysis and all passive and sensitive volumes information. The energy deposits in the sensitive parts of the charged particle detectors are used for the particle identification by $\Delta E\text{-}E$ method [82]. The particle identification method is based on the signal shape and amplitude analysis and will be described further. The information, obtained in the reconstruction step is used for the further analysis of the desired system and all possible reaction channels.

5.1 Beam detector

Here we present information about the properties of the produced ^{10}Be and ^{8}He beams. Such diagnostic always forms part of the preliminary analysis during the experimental run and provides such information, related to the beam, as: secondary beam integral, its components identification, beam energy in the central target plane and precision tracking.

The ΔE-ToF identification plots obtained in the main and reference experiments are shown in Fig. 13. It is clearly seen, that both beam particles are well separated and make up the largest part of the beam cocktails. The purities of the ^{8}He and ^{10}Be beams turned out to be 94% and 81% respectively.

For all identification plots of all the used detector systems, the particle selection was performed by the graphical cuts of ROOT package [83], which provides the functionality for pre-
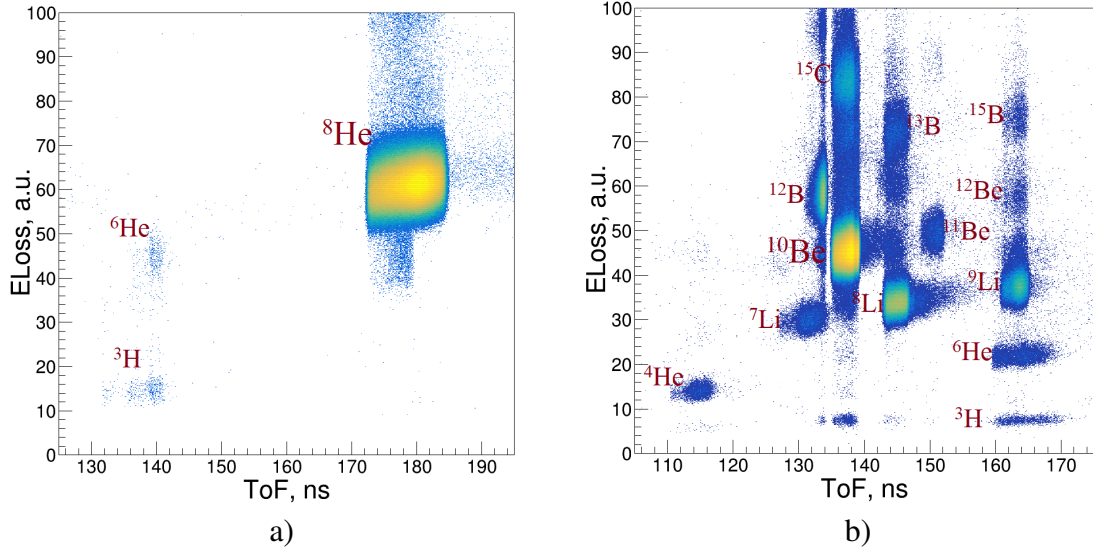
Figure 13: Beam identification plot showing the energy loss in plastic scintillator (250 μm thick) versus time of flight in the F5 plane. Left figure a) corresponds to the main experimental run with the ^{8}He beam with energy $\approx$26.5 MeV per nucleon. Right figure b) shows the identification of the ^{10}Be in the secondary beam, used in the reference measurements. The ^{10}Be beam had a mean value of energy in the central target plane $\approx$42 MeV per nucleon.

cise selection of the events on any type of two dimensional plot.

The tracking of the beam particles in the central target plane was performed with accuracy of $\approx$1.25 mm. The two-dimensional plots, typical for all conducted experiments, measured in this focal plane are presented in Fig. 14. The left distribution a) on the latter shows, that the beam was well focused on the target plane, so that $\approx$60% of the beam particles hit the central target area (no further than 8.5 mm from the center of the target). The intensive halo around the physical target, see the right b) distribution, is produced by the beam interaction with the 4-mm thick stainless steel boundaries of the target cell. The width of this halo is based on the beam tracking accuracy, which, as it was mentioned, made 1.25 mm for the central target plane. Those events obtained in halo with the experimental trigger are of no physical interest and should be excluded from the further analysis. Obviously, the location of four discernible halo areas, corresponding to different side telescopes, allowed to determine the target position and also allowed to verify the applied beam tracking selection.

All the mentioned beam information, being taken in combination, allowed us to reconstruct the four-vector of the beam particle in its state before passing through the second, F5 scintillator. Here we should mention that we are using the assumption that the studied reaction occurs in the central target plane. In order to implement the missing mass method, used for the reconstruction of the systems of interest, we need to obtain ^{8}He and ^{3}He four-vectors in the studied binary reaction in the interaction point. The latter is calculated by the developed software, which transports the corresponding particle through the all layers of the virtual setup geometry using the methods of G4EmCalculator, which was inherited from Geant4 [84]. Fig. 15 shows the kinetic energy in the two mentioned planes and energy losses of the ^{8}He beam particles, produced in the second experimental run.
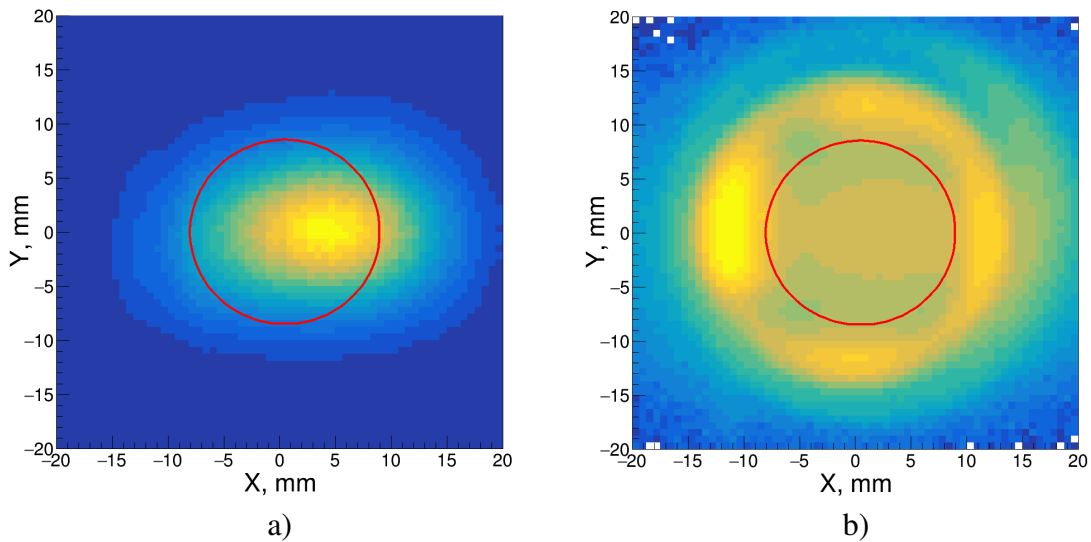
Figure 14: Beam profile at the central target plane, measured by the two MWPC detector planes, shown in Fig. 4. Left a) and right b) distributions correspond to the events detected with the beam and experimental triggers, respectively. The red circle on both figures demonstrates the selection of the events for the further processing.

5.2 Neutron detector

Among all the used particle detectors, only the stilbene wall is characterized by indirect technique of particle registration, based on the measuring the ionization losses of recoil protons and other particles (mainly recoil alphas) produced in the interactions of $\approx 30\,\text{MeV}$ neutrons with the carbon (hydrogen) nuclei making the composition of the detector material. Since the energy of the recoils is related to the neutron energy only indirectly the energies of neutrons detected by the stilbene neutron wall were calculated from their time of flight from the interaction point to the certain stilbene detector.

The fact, that the neutron wall with the described module configuration is located relatively far from the experimental target, leads to the fact that, during neutron detection, the main background is produced by γ-rays that can be attributed to nuclear interactions of the beam and the radioactivity of the materials surrounding the detector. The n-γ discrimination method is based on the difference between the signal shapes, produced by recoil particles (protons or alphas) and electrons. For each photomultiplier tube output signal has been independently read and provided three digital signal information: time, amplitude and so-called time-amplitude converter (TAC) signal. The latter value is proportional to the stilbene signal length, which in combination with the signal amplitude (giving information about the energy deposit obtained in stilbene) provides the n-γ discrimination. One example of the obtained identification plot is shown in Fig. 13.

It can be seen that the loci of neutrons and γ-rays are separated well for all energies of interest.
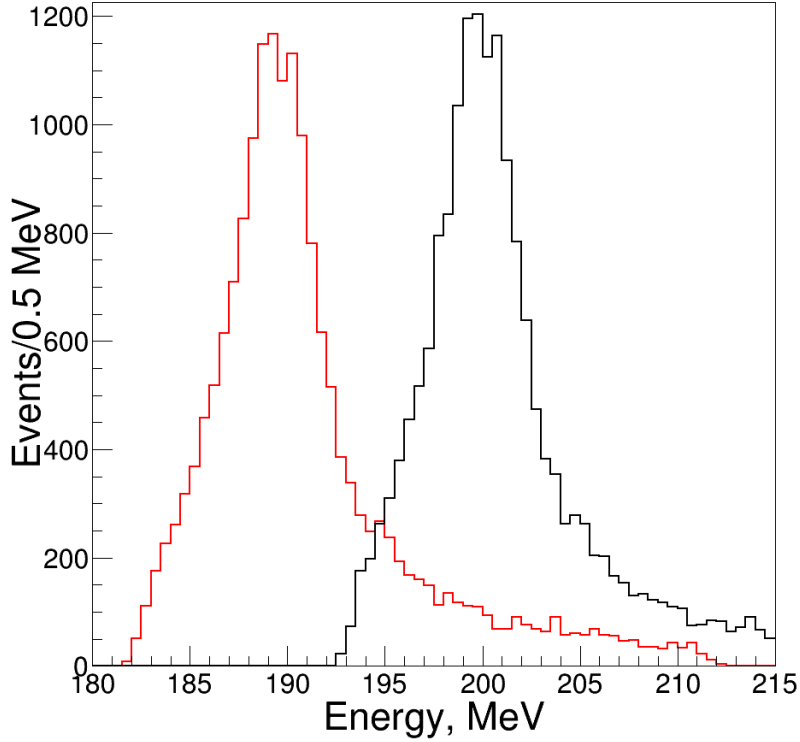
Figure 15: Kinetic energy distributions of the ^{8}He beam projectiles, obtained in the second experimental run. Black line relates to the energy value, directly calculated from the time of fight, which corresponds to the beam particle state before passing through the F5 scintillator. Red line shows the calculated beam energy in the central target plane.

5.3 Energy calibration

For both types of charged particle detectors (silicon strip and CsI(Tl) scintillator detectors) we assumed the linear dependence between the signal amplitude (N), directly proportional to the collected charge, on the energy loss ($E(N)$) of the particle inside the sensitive volume of the detector.

$$E(N) = aN + b, \tag{1}$$

where a,b are calibration parameters. According to the silicon detector properties, see Ref. [82], the calibration correlation, and therefore set of a,b parameters, is unique for each channel and does not depend on the particle charge and mass. The calibration measurements, dedicated to the determination of the calibration parameters and such properties as dead layers on the surfaces of all silicon detectors and their energy resolution, were carried out with the use ^{226}Ra. The measurements were conducted with different geometry of the detector and source layout. The detailed description of the whole process of the silicon strip detector calibration, developed by our group, given in Ref. [85]. This technique allowed to determine the dead layers with uncertainty of $\approx 0.1\,\mu$m and reach the energy resolution making $\approx 0.5\%$.

Although we have conducted the calibration measurements of the CsI(Tl) detectors with the ^{226}Ra source, the genuine calibration of these detectors was based on the main experimental-run data. The key reason for this approach is that the scintillator detector response behavior is not
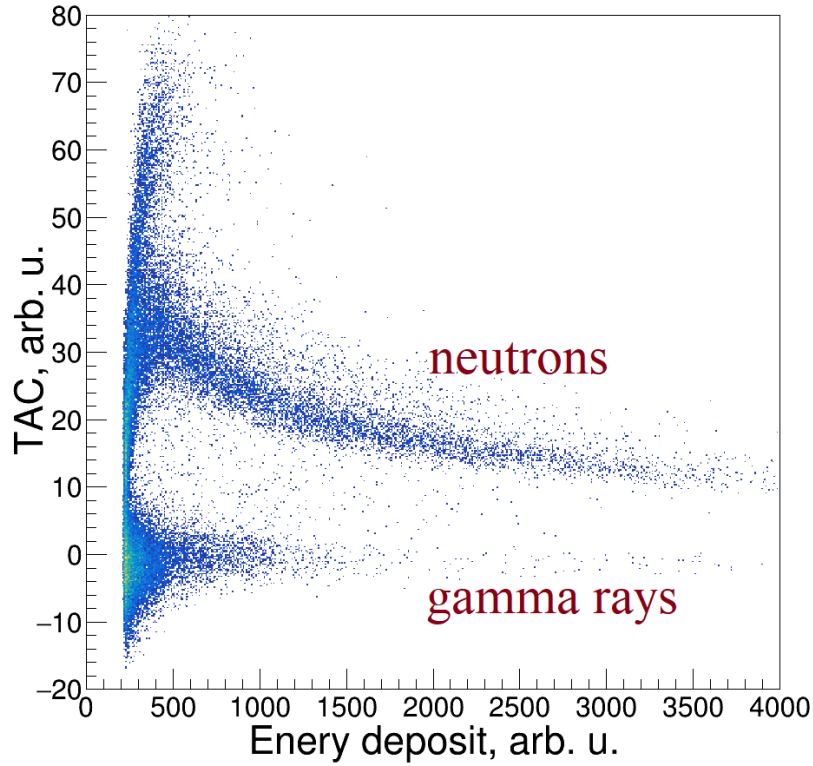
Figure 16: The discrimination of γ and neutron events.

the same for different types of particles, see Ref. [82]. That is why, for the precise measurements of the certain particles (p, d, ^{3}H, ^{3}He, ^{4}He, etc.), the calibration should be performed using the same particles, registered in the wide range of energies. According to the kinematics, described in Chapter 4, the studies of all reaction channels of interest required that the central telescope is utilized for the detection of the high energy particles, which allows one to use the linear approximation of the detector response. The energy loss of the selected particles (^{3}H in our case) inside the sensitive volume of the CsI(Tl) crystals was calculated from the energy deposit in the double side silicon strip detector, the first layer of the central telescope. Although, such technique is based on the non-direct energy determination, which suffer from errors increasing with energy, it allowed to reach energy resolution of $\approx$1.5%.

5.4   Central telescope

The first problem associated with the work of the central telescope was that the scintillator detector response changed over the whole beam time. That is why the application of the same set of calibration parameters for the whole experimental data was not appropriate and the energy resolution for the detected particles became worse during the experiment. That is why, the whole collected statistics was divided into 6 equal parts, which were used for the individual CsI(Tl) calibration procedures.

The main problem was that the multiplicity (by this we mean the number of time-amplitude signal pairs written) turned out not single in more than 80% of events. And compared to the silicon sensors, where the multiplicity did not exceed 1 in 98% events after the offline amplitude
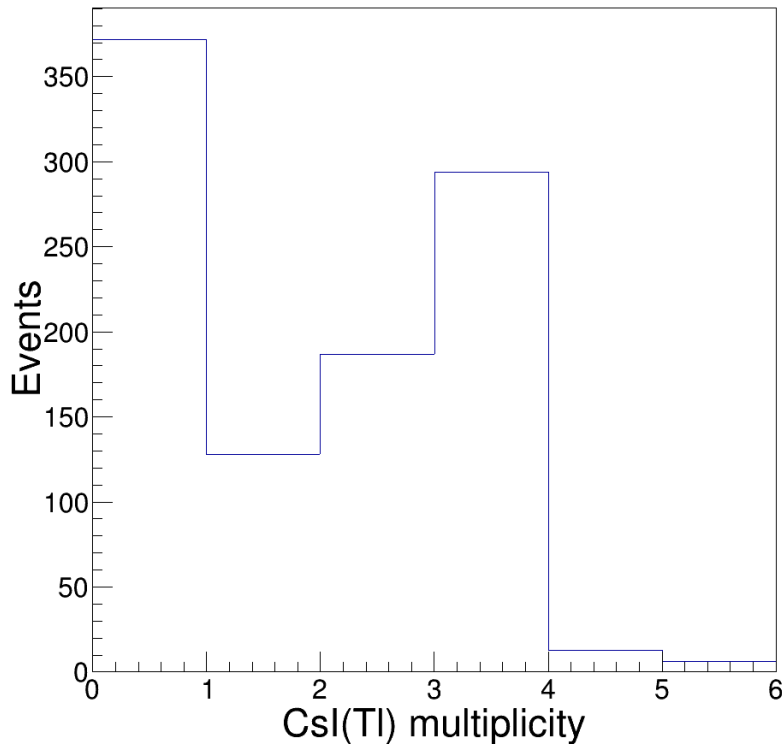
Figure 17: Obtained multiplicity of the CsI(Tl) detector.

thresholds and complex time selections were applied, the CsI(Tl) detector multiplicity remained non-trivial, see Fig. 17. One of the reason for such multiplicity were the optical or/and electronic crosstalks, occurred in the crystal-photomultiplier tube assemblies. The crosstalk effects, led to the identification problems by the ΔE-E method, and these effects remained in the final cleaned data shown in Fig. 18.

In order to perform the particle identification in the central telescope in the situation of multiple signals obtained in the second layer, we have determined the true amplitude, based on the tracking. The trajectory and the true scintillator interaction point of the particle emitted from the target were reconstructed in linear approximation, using the particle coordinates in the central target plane and in the double-sided SSD plane. Eventually, we found out, that for all events (>90% of the collected data) the crystals, determined by such reconstruction, had the maximum energy deposit. Such method allowed us to get rid of the major part of crosstalk contribution, and the reminder does not harm the identification quality, see Fig. 18.

For particle selection, we used 16 graphical cuts corresponding to each of 16 CsI(Tl) crystals. A typical example of the obtained particle identification is presented in Fig. 18. The latter was obtained from the data of the second experimental run carried out with the ^{8}He beam, which produced the most intensive locus, caused by the elastic scattering of the beam particles. The applied ΔE-E method provided the clear identification of all detected nuclei, and in particular ^{3}H, measured for the ^{2}H(^{8}He,^{3}He)^{7}H reaction studies.
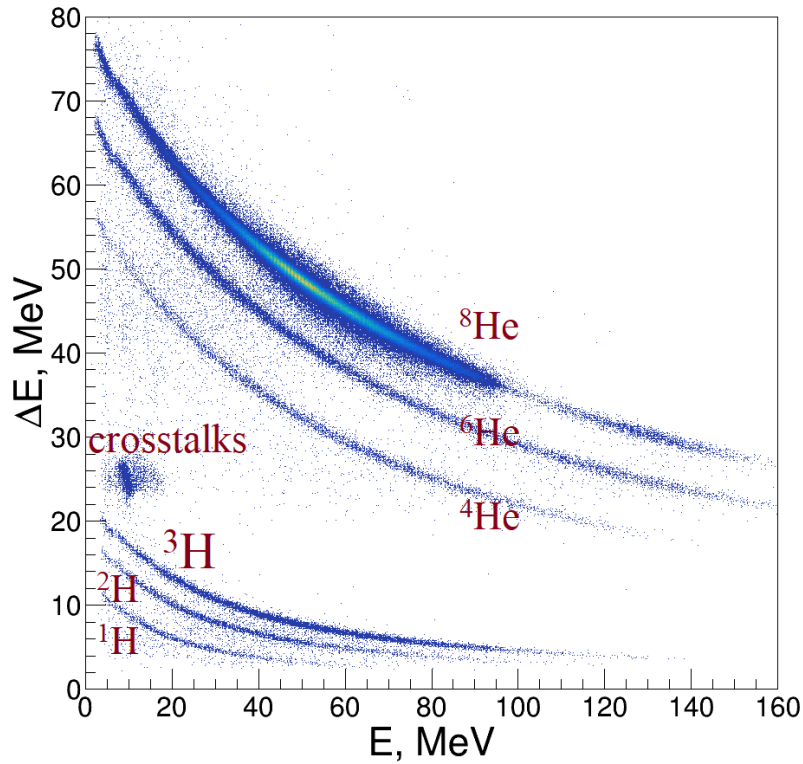
Figure 18: Identification plot obtained by the ΔE-E method in the central telescope, corresponded to one of the scintillator crystals. The remained crosstalks contribution is localized and covered the small area, which does not affect the particle distinction quality.

5.5 Side telescopes

The silicon detector assembly, used for detection of the recoil ^{3,4}He, produced in the studied binary reactions, was the key element of the setup. As it was mentioned above, the collected statistics came essentially from the detection efficiency of the recoil particles. Moreover, the main contribution to the resolution of the determination missing mass-spectra is the accuracy of the recoil four vector reconstruction in the interaction point.

Energy calibration of all telescope layers has been conducted with the same ^{226}Ra alpha source. All calibration measurements have been conducted consecutively with telescopes construction, starting with the third, veto layer. However, the described in Chapter. 5.3 energy calibration methods could not be applied for such thin detectors, as we have used for the telescopes' first layers. The developed methods of silicon detector calibration are applicable if all emitted alphas are stopped in the sensitive volume of the calibrated sensor. But alpha particles with initial energy $\approx$7.68 MeV penetrate $\approx$46 μm of silicon, which suggests that the Bragg peak locates deeply in the sensitive area of the second layer of the telescope. That is why the spectra obtained in the measurements with a alpha source located so that the emitted particles hit the detector center at approximately 90°, shown in Fig. 19, did not allow to apply the mentioned calibration algorithms.

The developed solution for the thin detector calibration consists of two steps. First of all, the preliminary parameters were calculated from the linear approximation applied to the base of
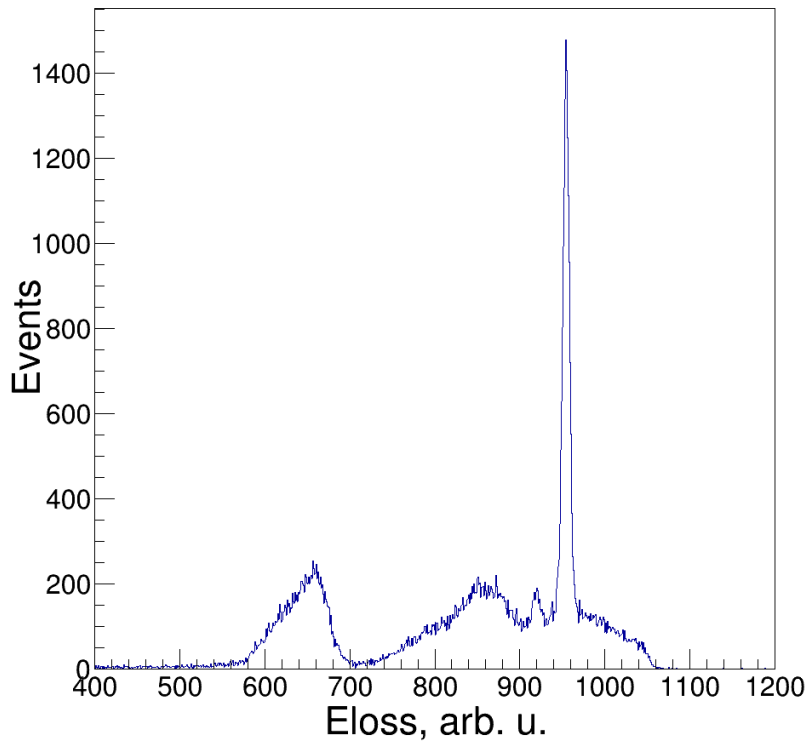
Figure 19: Typical spectrum of the energy deposit in 20-μm thick detector, obtained in the calibration measurements. The distinct peak corresponds to the only one stopping particle of initial energy 4.78 MeV in the sensitive volume of the detector.

two experimental points: the peak position of the stopped alpha particle and the position of the electronic noise signal. The latter is collected from all channels corresponding to the detector strips which were not irradiated in the certain event. The first stage calibrating signals coming from the thin detectors are used to obtain the cumulative spectra of the energy deposits in the first and the second telescope layers. Obviously, the first peak, corresponding to the stopped particle in the thin detector, was at the expected position: 4.7843 MeV. The second calibration step is the modification the current thin detector calibration parameters, so that the peaks of the alpha particle with the highest (7.68 MeV) energy had the same position in the spectrum obtained in each channel.

In the obtained spectra only the first peak of the lowest energy turned out to be obtained at its expected position, and the whole spectrum differs from that, obtained in the thick detector calibration. The main reason is that the effective dead layers were not equal for particles of different energies, and, moreover, the collected data did not allow us to determine the backside dead layer thickness of the thin detectors. However, the identical structure of the presented spectra is a confirmation of the correctness of the obtained calibration parameters, which eventually allowed to identify all particles of interest, see the identification below.

The first attempt of the particle identification by means of the ΔE-E plot was not satisfactory. In Fig. 21 the identification obtained from one of the side telescopes is presented. One can see that the hydrogen isotopes can be distinguished from the helium group, but, the desired ^{3}He cannot be observed being mixed up with ^{4}He.
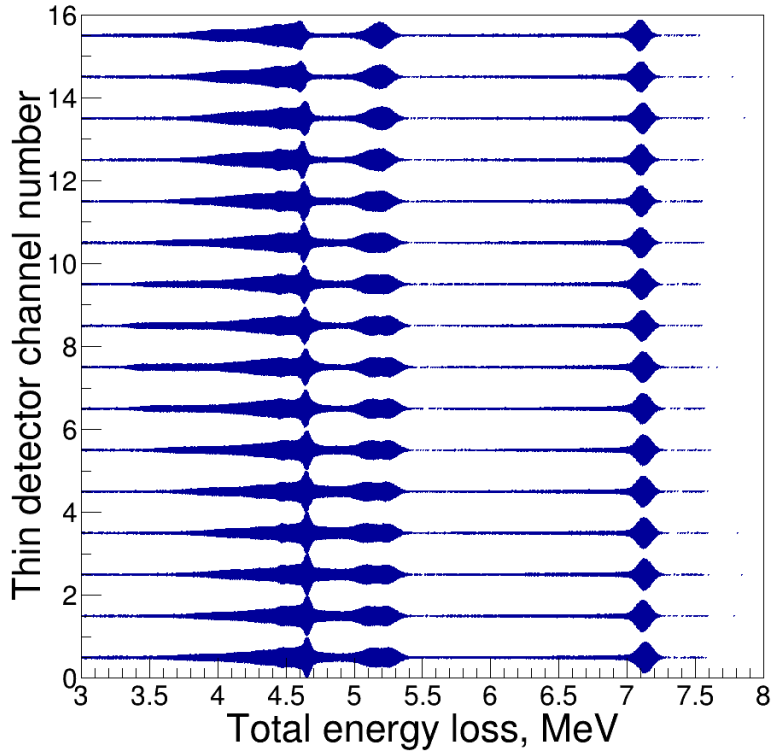
Figure 20: Obtained spectra of the total energy losses in 20μm and 1 mm-thick silicon detectors, typical for all four telescopes. 16 spectra are corresponded to different thin detector channels, plotted on the vertical axis.

Our idea to improve the identification quality was to examine the thickness inhomogeneity of the 20 -μm thick detectors. It happened for a reason. During the calibration of the thin detector, we found out that the spectra of energy-deposit, registered by the second layer, i.e. by the 1-mm thick detector differs for different strip numbers of thin and thick detectors, see Fig. 22. This led to the only conclusion that the thickness of the 20 -μm detector is heterogeneous.The thickness inhomogeneity maps were determined as follows. Here, we will call a pixel the part of the i-th strip number of the first-layer detector corresponding to the j-th strip (oriented orthogonally) of the second-layer detector. Thus each first-layer silicon detector has i×j pixels in total.

For the thickness map determination we used the same data processed for the thin detector calibrations. The silicon telescopes were located at the same positions, as in the certain experimental run, and the alpha source was installed into the deuterium target position. Obviously, the geometry of the division of the thin detector into the pixels depends on the position of the irradiating particle source. That is why the described telescopes and source position allowed us to be sure, that the layout and size of the pixels, examined in the calibration measurements correspond to those considered in the experiment.

The energy loss in the 20-μm detector as a function of the fired strips numbers in the first- and the second-layer detectors was derived from the shift of the peaks in the 1-mm detector compared to measurements made without the 20-μm detector. Alpha particles with energy ≈7.68 MeV penetrate ≈46 μm of silicon, which suggests that the Bragg peak locates deeply
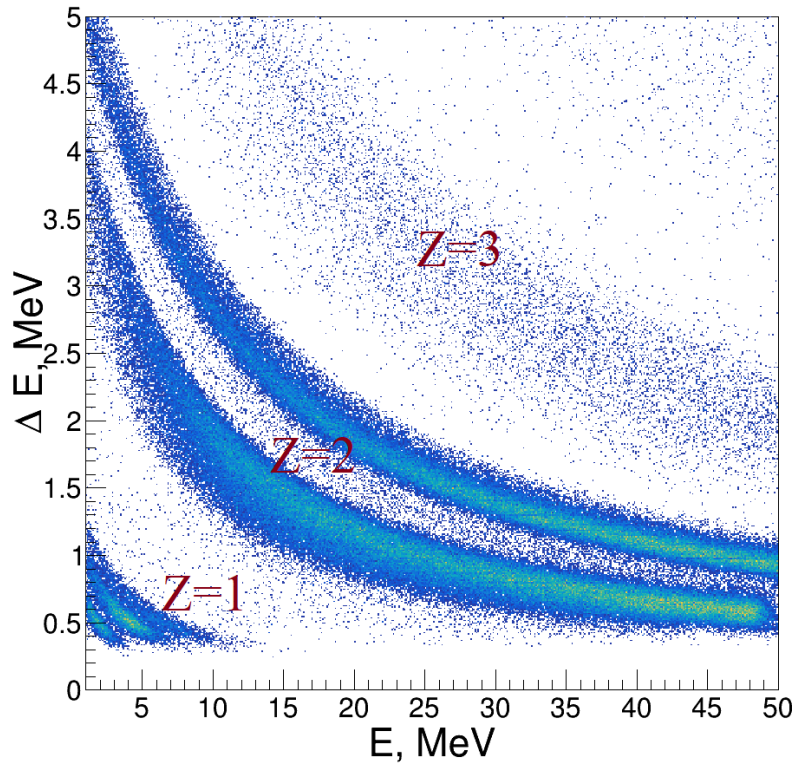
Figure 21: ΔE-E particle identification plot, typical for all telescopes. Vertical and horizontal axes show the energy deposit in the 20 -μm thick (ΔE) and 1-mm thick (E) detector, respectively. One may see that only isotope groups with different charge (Z = 1, Z = 2, Z = 3) can be distinguished.

in the sensitive area of the second layer detector. It was observed that among all the particles emitted by the source only these particles with the highest energy could always penetrate the thin detector and the dead layer of second sensor giving in the latter the signals with amplitude above the noise threshold. That is why only these signals were used for the thickness analysis.

The obtained values of the energy losses were converted into the thickness using the G4EmCalculator parameterization.

The obtained thickness distribution of all four used 20-μm thick ΔE detector is shown in Fig. 23. Although the number of strips of the first and the second layer detectors is 16, one may see that the obtained thickness map consists of less than 16×16 pixels. It is caused by the shading of the second layer sensor by the supporting frame of the thin detector. The obtained thickness distribution turned out to be quite non-uniform. Although it was declared by the manufacturer that such detectors have thickness variation not more than 2 μm from the nominal value (20 μm), one can see that the investigated detector does not meet this criterion. In order to check the results, the thickness non-uniformity was also verified with the LISE++ energy loss parameterization. The thickness maps obtained by both methods are consistent within less than 1 μm.

The thickness maps were used to improve the isotope separation obtained in the ΔE-E identification plot. Note that poor statistics did not allow us to build the identification plots individually for each pixel. Under the assumption of the small thicknesses, the energy loss of a particle

| a) Pixel (7,7) | b) Pixel (1,14) |

Figure 22: Spectra of the energy losses in the 1-mm thick detector of the first telescope, corresponding to different fired pixels (different strips in the first and second layer detectors, shown in bra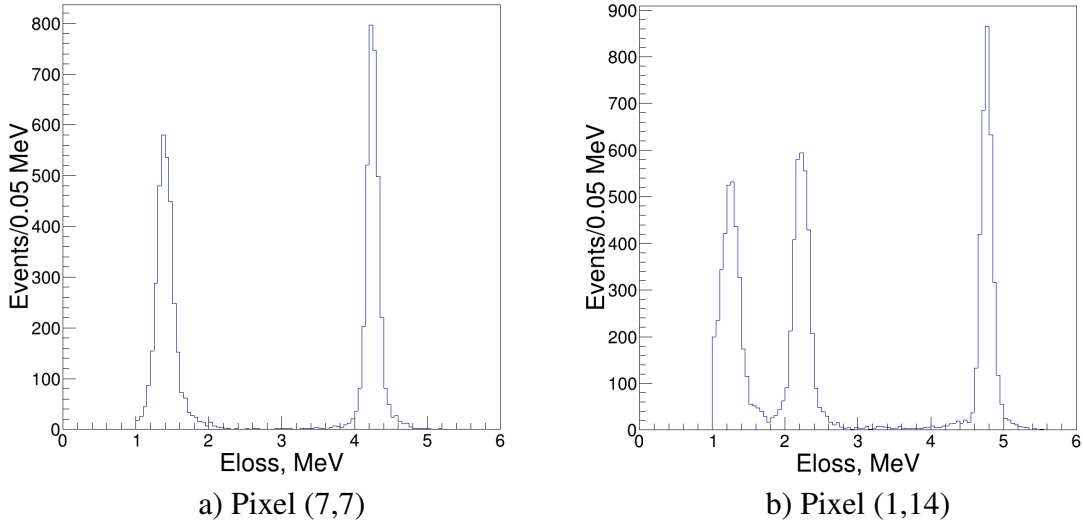ckets). It is clearly seen, that the structure and the position of the peaks, corresponding to the same initial energies, are different confirming suggestion that the thicknesses of the corresponding pixels are different. Pixel (7,7) is obviously thicker than (1,14).

per unit path ($\Delta E/\Delta X$) can be considered as constant. The energy losses occurring for different ΔX are proportionally related, which fact was used for the ΔE normalization performed in the following way:

$$\frac{\Delta E_k}{\Delta E_{corr}} = \frac{\Delta X_k}{\overline{X}},$$ (2)

where ΔX_k and ΔE_k represent the thickness of the k-th pixel and the energy loss in its sensitive area; ΔE_{corr} is the corrected energy; $\overline{X}$ is the normalization thickness value (20 μm in our case). An amendment to the ΔE_k was used to correct the energy deposit in the second layer SSD:

$$E_{corr} = E_k + \Delta E_k - \Delta E_{corr},$$

where ΔE_k and ΔE_{corr} denote, respectively, the energy deposits in the 20-μm thick detector, obtained before and after correction.

The particle identification plot obtained by the described correction method is presented in Fig. 24 where the same experimental data as used in Fig. 21 were processed. One may observe that all the helium and hydrogen isotopes are clearly distinguishable, and the loci of the desired ^{3}He and ^{4}He are well separated.

The energy of the recoil particle at the interaction point was calculated using the implemented in G4EMCalculator class methods. It is essential that the same energy-loss parameterization was used both for the determination of the thickness map and calculation made of the energy of detected particles. For this reconstruction the passive parts of the target and dead layers of the detectors were taken into account going consecutively along the particle trajectory. The particle emission angle was also taken into account. As an additional cross check, we used two methods for the energy reconstruction in the interaction point, see Ref. [86].

34
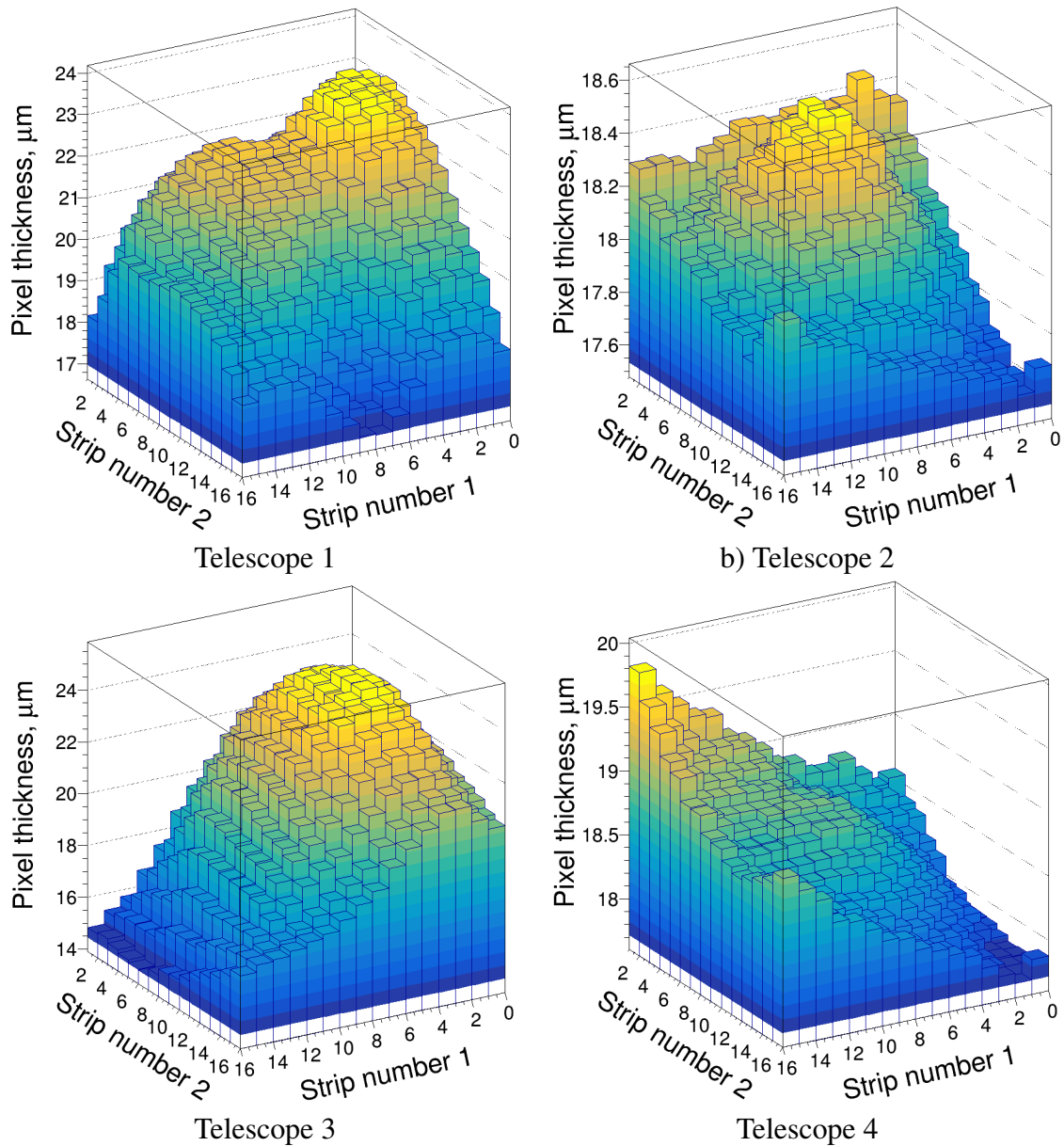
Figure 23: The thickness map for all used 20-μm thick detectors. Vertical axis shows the calculated pixels' thickness in micrometers. Strip numbers 1 and 2 represent the strips fired in the 20-μm thick and 1-mm thick detector, respectively. Unlike strip number 1, which takes values 1–16, strip number 2 accepts values from 1 to 15 which is due to the fact that the first strip of the second detector layer was shaded by the housing frame of the corresponded thin detector.

In the first method, the reconstruct kinetic energy in the interaction point was taken as a sum of the energy deposits in the first and second telescope layers and added to this the calculated average energy losses in all the passed passive volumes (detector dead layers, target cell and gas volume). In the second method, the reconstructed kinetic energy of the studied particle in the interaction point included only the sum of the energy measured in the second, 1-mm thick detector and the calculated average energy losses in the entire thickness of the corresponding pixel of the front thin detector and target volumes. We have shown in Ref. [86] that the difference of the results provided by these two methods is just about 70 keV, which is comparable with the detector resolution. The latter confirmed the correctness and plausibility of all results,
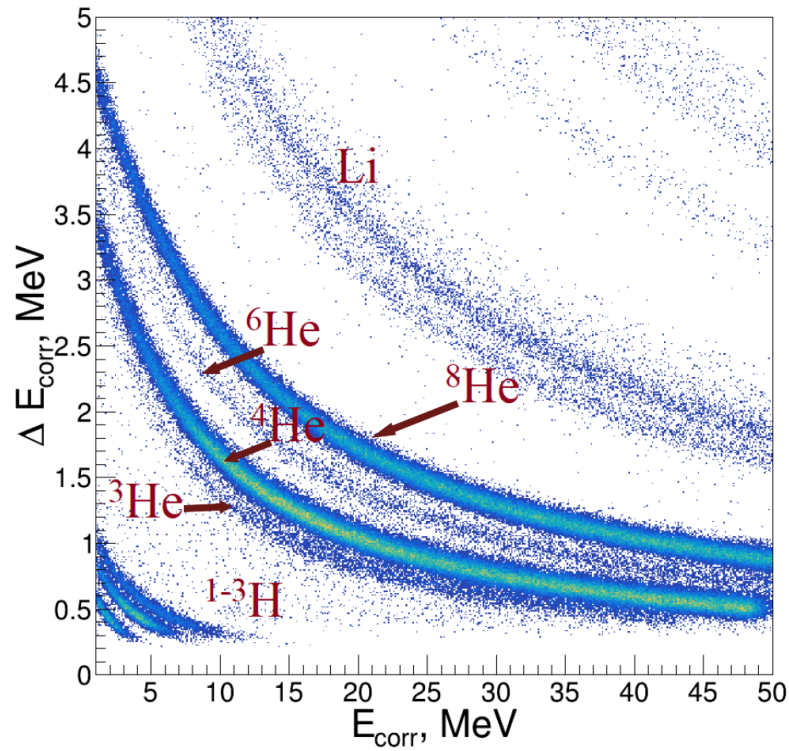
Figure 24: Corrected ΔE–E identification plot after thin detector thickness normalization. Vertical and horizontal axes show the energy deposits in two silicon detector layers with the thickness correction as described in the text. All isotopes are nicely separated from each other. Desired ^{3,4}He nuclei can be also observed.

presented in this chapter: the calibration of the thin detectors, their thickness map determination and the obtained particle identification. Further, for the missing mass reconstruction, the energy of the particle, registered by one the side telescopes, is reconstructed by mean of the second method described above. Such approach allowed us to get rid of such unknown parameters as thin detector dead layers and do not rely on the thin detector calibration parameters obtained by non-traditional method.

6 Results: reference experiment

The proton pick-up reaction ^{2}H(^{10}Be,^{3}He)^{9}Li was studied with a 42 AMeV ^{10}Be secondary beam in order to test the reliability of the data obtained in the principal experiments, to control calibration parameters, and to get an experimental estimations of the missing mass resolution. These measurements were performed just after the second ^{8}He beam run, keeping the same and all conditions were satisfied related to the experimental setup.

During the reference measurement the measured ^{10}Be beam-integral turned out $\sim 17 \cdot 10^9$, $\sim 2.5 \cdot 10^9$ and $\sim 7 \cdot 10^9$ for thick, thin and empty target runs, respectively. The recorded events satisfied all the beam reconstruction (all sensors were fired in the expected time range; only one beam particle was reconstructed in each event) and the tracking conditions (the ^{10}Be particle passed through the aperture of the diaphragm and hit the central part of the deuterium target: circle 17 cm in diameter).

The total amount of the registered ^{3}He recoil nuclei with their reconstructed kinetic energies in the central target plane less than 25 MeV was 11744, 1294 and 2941 for the thick, thin and empty target runs, respectively. We suggest that all ^{3}He were obtained by the d-^{3}He reaction mechanism, which produces the studied ^{9}Li. The obtained ^{9}Li excitation spectra, later E_T(^{9}Li), shown in Fig. 25 for all 3 runs, are presented with respect to the mass of the well-known ground state of 8406.869 MeV [78].
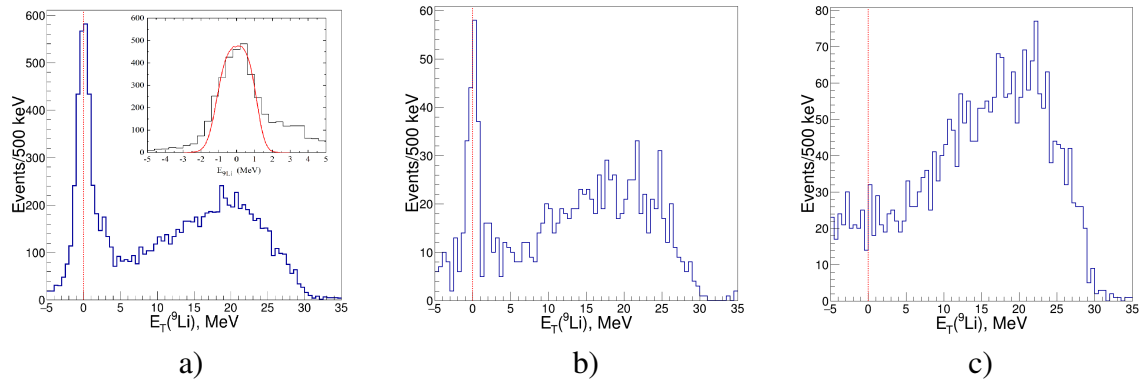
Figure 25: Excitation spectrum of ^{9}Li derived from all ^{3}He registered by the side telescopes with energy < 25 MeV produced in the ^{2}H(^{10}Be,^{3}He)^{9}Li reaction. The insert in the left a) figure shows the part of the measured ^{9}Li spectrum near the ground state. The red lines show the ground state position. a) - thick target run, b) - thin target run, c) - empty target run.

All spectra in Fig. 25 show a well-pronounced peak corresponding to the ground state of ^{9}Li populated in the ^{2}H(^{10}Be,^{3}He)^{9}Li(g.s.) reaction. On the right slope of this peak the population of not well-resolved first excited state of ^{9}Li (E* = 2.69 MeV) is also observed. The insert in Fig. 25a) shows the part of the ^{9}Li spectrum near the ground state. The red curve demonstrates the Monte Carlo calculation for the ground state of ^{9}Li using parameters of the experimental setup. It is clearly seen, that the Monte-Carlo simulation reproduces quite well the shape of the ^{9}Li ground state peak demonstrating the experimental resolution of $\approx$2.2 MeV (FWHM). The corresponding calculations of the missing mass spectrum resolution of ^{7}H at energy near 2 MeV gave FWHM$\approx$1.1 MeV. The reason for this $\approx$2 times better resolution in the ^{7}H experiment is
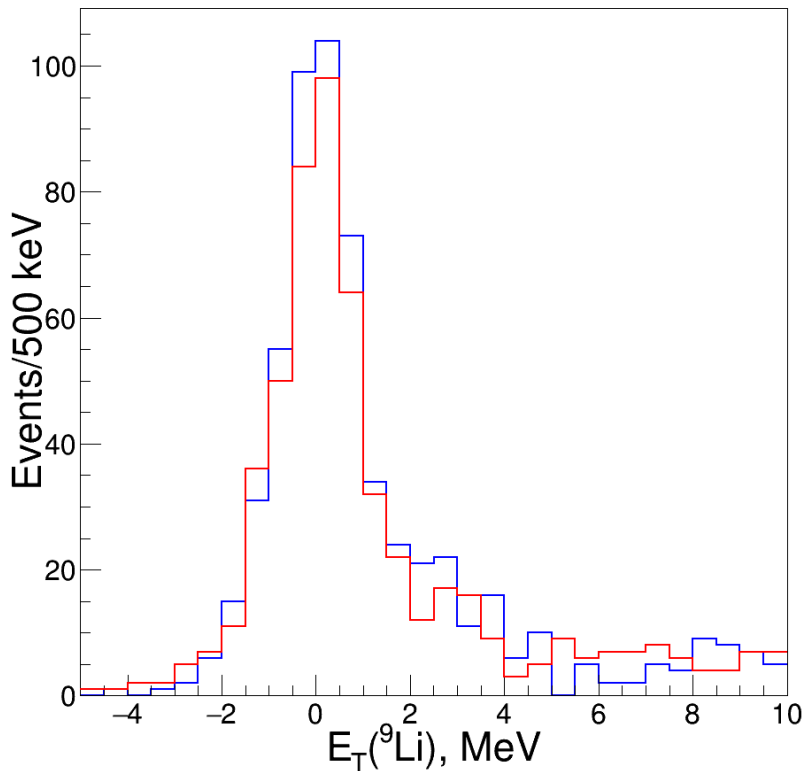
Figure 26: Excitation spectra of ^{9}Li, obtained from different side silicon telescopes; shown in different colors.

caused by the larger energies of the ^{3}He recoils, as compared to the ^{2}H(^{10}Be,^{3}He)^{9}Li reaction, and, therefore, the smaller energy losses in the target. It is also a demonstration that the target thickness makes the main contribution to the energy resolution in this energy range.

Before the detailed data analysis, we compared the results, obtained from the identical detectors (side silicon telescopes in our case). Such procedure in conjunction with simulation results, allowed to check and adjust within the error limits the layout of all detector systems and used calibration parameters. Fig. 26 presents the comparison of the results related to different side telescopes (two typical telescope are selected) and shows the complete agreement of the reconstructed missing mass spectra. The latter ensured the reliability of the cumulative spectrum from all detectors, analyzed below.

One can expect to detect the long-lived ^{9}Li moving towards at forward angles with approximately same as beam energies 42 AMeV. However, the registration of those, suffered from the low efficiency, caused by the CsI(Tl) crystals overload, high level of crosstalks and low resolution, especially for those crystals, focused by the beam. Never the less, the condition of the single particle registration in the central telescope, also significantly improves the quality of the spectra, drastically reducing the amount of random coincidences at higher energies (E_T(^{9}Li)>5 MeV) and making distinctive the ground and the first excited states (the ^{9}Li first excited state is located at 2.691 MeV above the ground one [78]), see Fig. 27. The latter is particularly apparent in Fig. 27 b), corresponding to the thin target run characterized by the higher energy resolution. Those events, for which the ^{9}Li identification was achieved, are shown in
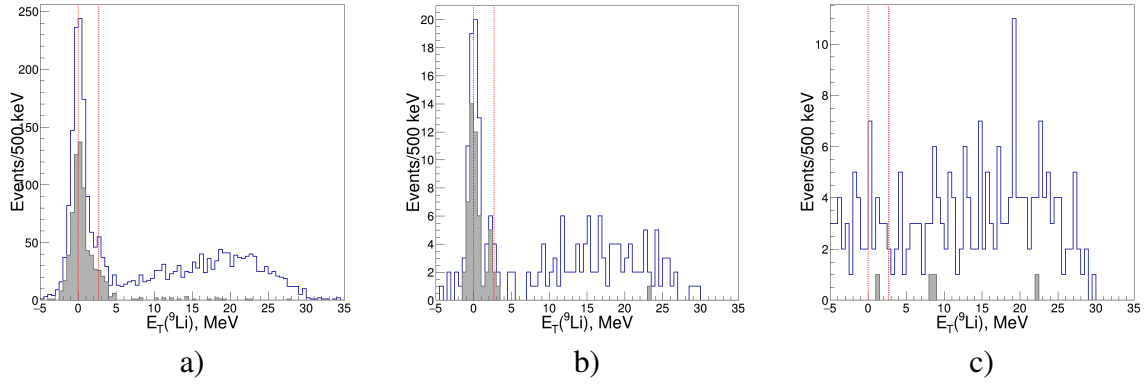
Figure 27: Excitation spectrum of ^{9}Li derived from the recoil ^{3}He detected in coincidence with the single particle tracked in the central telescope. Gray spectra show the events with ^{9}Li identification. The red lines show the positions of the ground and the first excited states. a) - thick target run, b) - thin target run, c) - empty target run.

gray color and confirm the mentioned structures.

Fig. 28 shows the angular distribution extracted from the experimental data obtained at the forward center-of-mass angles $(3^\circ\text{-}13^\circ)$ for the ^{9}Li ground state populated in the ^{2}H(^{10}Be,^{3}He)^{9}Li reaction.

The differential cross sections were analyzed with the Coupled Reaction Channels Calculations approach using the code FRESCO [87]. For the entrance (d+^{10}Be) and exit (^{3}He+^{9}Li) channels the Global Wood-Saxon optical potential models were used, see Ref. [74, 75]. In the calculations, spectroscopic factor (SF) for the ^{3}He=p+d clustering was set as SF=1.32, according to the value obtained by in work [88].

It should be noted that before our research, the SF for the system ^{10}Be(g.s.)=p+^{9}Li($3/2^-$) was unknown. To evaluate corresponding SF we used the shell-model Hamiltonian based on the monopole universal interaction, see Ref. [89]. The latter provided the spectroscopic factor of 1.74 for the ground state ^{10}Be=p+^{9}Li(3/2-) clustering while for the p+^{9}Li(1/2-) configuration it was found to be 0.207. As it is seen from Fig. 28, the red curve, which corresponds to the FRESCO calculation with the mentioned above SFs for the ^{3}He and ^{10}Be(g.s.) clustering, perfectly describes the experimental data. Thus, the measured differential cross sections of the ^{2}H(^{10}Be,^{3}He)^{9}Li(g.s.) reaction at forward center-of-mass angles confirm the modern theoretical approach for the ground-state structure of the ^{10}Be nucleus.

As for the total cross-section of the ^{9}Li ground state population, at the covered forward angles in the center-of-mass system the obtained value turned out $\approx$7–10 mb/sr.

Thus, the data obtained with the ^{10}Be beam provide an independent cross-check of the missing mass spectrum calibration in the second ^{8}He beam run. The presented results represent an important support in the data interpretation and analysis.

Figure 28: The angular distribution obtained for the ^{2}H(^{10}Be,^{3}He)^{9}Li(g.s.) reaction (black squares). The error bars are statistical only. The red curve shows the results of the FRESCO calculation.

7 Results: experiment 1
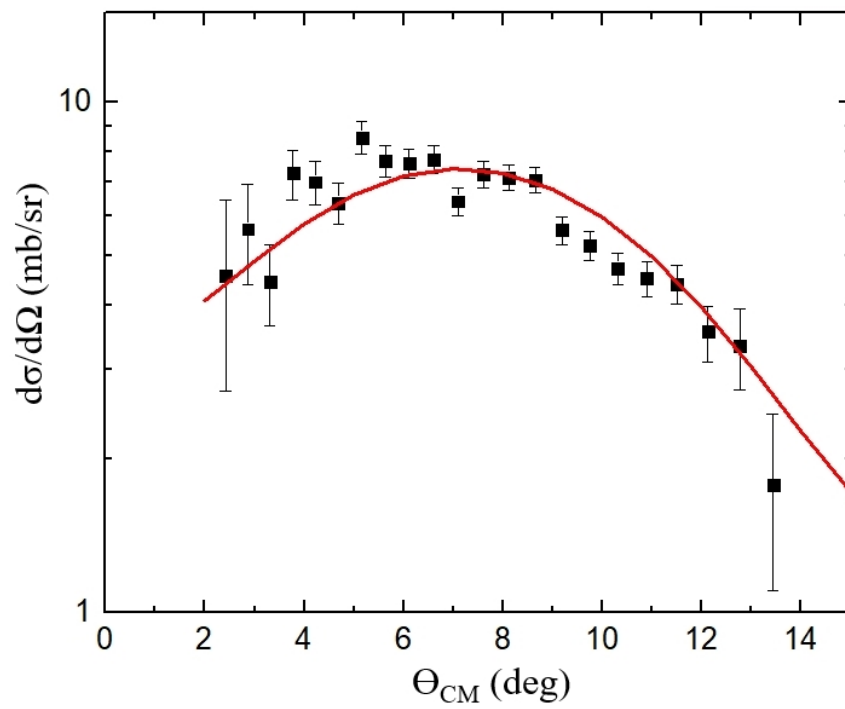
Technical conditions of the first ^{8}He run allowed to achieve $\sim 90\%$ purity and intensity $\sim 10^5$ ^{8}He projectiles per second. This satisfied the same conditions which were used in the reference measurements.

The amount collected during the whole run ^{8}He beam integral flux was $\sim 6.4 \cdot 10^9$. As in the case of ^{9}Li, the desired ^{7}H is calculated as a missing component of the binary reaction. The obtained missing mass spectrum is further presented with respect to the cumulative mass of its decay components (above ^{3}H+3n decay threshold).

The total number of ^{3}He-^{3}H coincidences found in the recorded data was 113. But, due to the kinematic selection, only 105 of these events were identified as the population of ^{7}H. The correlation we used for this selection is shown in Fig. 29 a). This is the correlation of the ^{3}H kinetic energy in the ^{7}H center-of-mass frame with the reconstructed ^{7}H excitation energy E_T. Such correlation of the kinetic energy of the emitted particles in the reference frame, attached to the decayed system, we refer as "kinematical triangle". The latter is based on the simple energy and momentum conservation laws and allows to consider all events, lying above the kinematic border, y=3/4 x in the case of ^{7}H$\rightarrow$^{3}H+4n decay, as not physical and deserving hence to be cut off in the further data analysis. By analyzing the amount of events above and below the kinematic border, the described selection also served as a reaction channel identification. Let us note that such information was provided due to the precise measurements of the emitted tritons, which was the main novelty and advantage of both conducted experimental runs.

It can be seen from Fig. 29 a) that the majority of obtained data satisfied the kinematics condition, and therefore is in agreement with the idea of the ^{7}H production in the ^{2}H(^{8}He,^{3}He)^{7}H experiment and its subsequent decay with the emission of ^{3}H. Another evidence for the ^{7}H population is that the experimental data acquired with the empty target showed that the contribution of the background, caused by the beam interactions on the target windows was at a level of 10%.

7.1 First excited state; the first observation

The reconstructed missing mass spectrum of ^{7}H is shown in Fig. 29 b). In this spectrum the peak with energy $E_T = 6.5(5)\,\text{MeV}$ and width Γ=2.0(5) MeV is identified. For the description of this peak, see the dashed and dotted curves in Fig. 29 b), we used the Lorentzian profile with the energy-dependent $\Gamma(E_T)$ [90]. The standard statistical χ^2 tests of the hypotheses provided in Fig. 29 b) give confidence level 0.9–0.95 for the presence of the 6.5 MeV peak within the energy interval $3 < E_T < 11$ MeV. Moreover, in contrast, the assumption that this spectrum can be described by some smooth distribution gives confidence level 0.05–0.25 depending on details [91]. Thus, all the above-mentioned allowed us to conclude the observation of the 6.5 MeV resonance state of ^{7}H in the reconstructed missing mass spectrum. We interpret this peak as the first excited state of ^{7}H, which can be formed by the doublet, built on the 2^+ configuration of valence neutrons. The suggestion to resolve this peak as a possible $5/2^+$ and $3/2^+$ doublet, located at 5.5-7.5 MeV above the decay threshold, was made in the second experiment, see Ref.
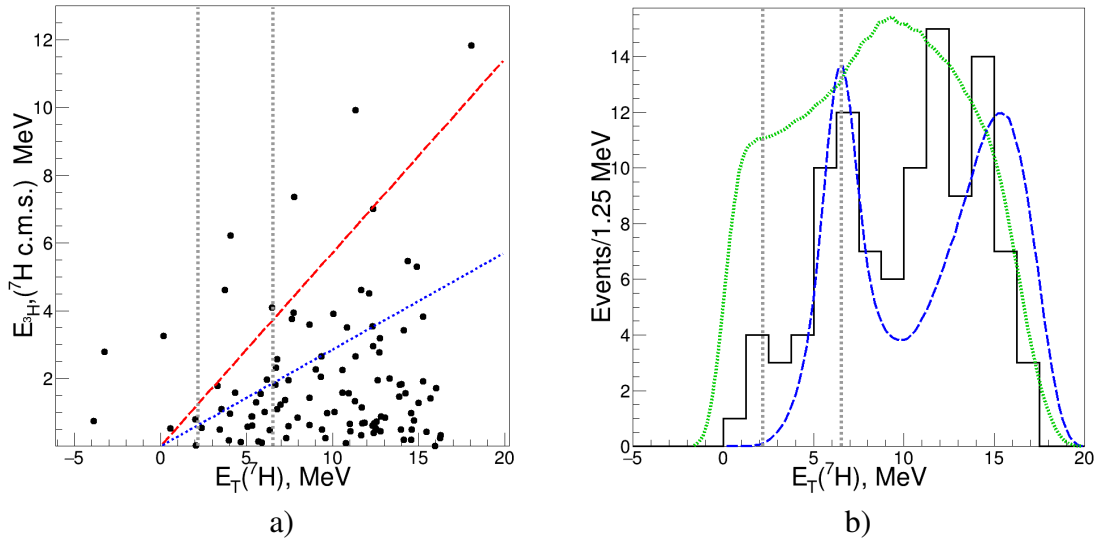
Figure 29: a) Correlation between the ^{3}H kinetic energy calculated in the ^{7}H in center of mass frame with the ^{7}H excitation energy. The red dashed line shows the kinematical limit for tritons coming from the ^{7}H decay. The blue line corresponds to the $E_{3H} < 2/7 E_T$ selection discussed later. b) The ^{7}H missing mass spectrum reconstructed from the events satisfying the triton kinematics selection. The blue dashed curve in b) shows the fit to the data by the 6.5(5) MeV resonant state with $\Gamma = 2$ MeV plus the contribution of the rising $t+4n$ five-body phase space distribution (forming the spectrum at high energy part $E_T > 11$ MeV). Green dotted curve illustrates the setup efficiency. Two vertical dotted lines corresponded to the declared ground and first excited states.

[92], described further.

7.2 Indicators for the ^{7}H ground state

In Fig. 29 b), another group of events the lower ^{7}H energy E_T is observed. This group located at $E_T \sim 1.8$ MeV was interpreted as first indication of the population of the ground state of ^{7}H. Despite to the obviously low statistics, multiple consistency checks for these ^{7}H ground state candidate events were performed, see Ref. [91]. Moreover, in work [91] we have shown that the angular and energy distributions of the emitted tritons relative to the retrieved ^{7}H flight direction in the laboratory frame showed that all collected 5 candidate events are located in excellent consistency with the theoretically predicted behaviour in Ref. [81].

The obtained in experiment 1 ^{7}H low-energy spectrum is in accord with the results of Ref. [45], see Fig. 30. Let us mention that the latter was obtained in the same reaction at different energy but with worse energy resolution. Multiple reasons did not allow authors of work [45] observe the ^{7}H first excited state, however, the peculiarity at $E_T \approx 2$ MeV was pointed out. Such fact is another important evidence of the reliability of the declared results, making this work a logical successor to its predecessors in resolving the ^{7}H problem.

The spectrum behaviour at energy $E_T > 10$ MeV, is not an object of discussion in this work, due to rapidly rising phase space and drastically decreasing energy resolution at high excitation energies. The conjunction of this factor with the setup efficiency shown in Fig. 29 b) with the green dotted curve may provide a variety of spectrum shapes, thus making this area of
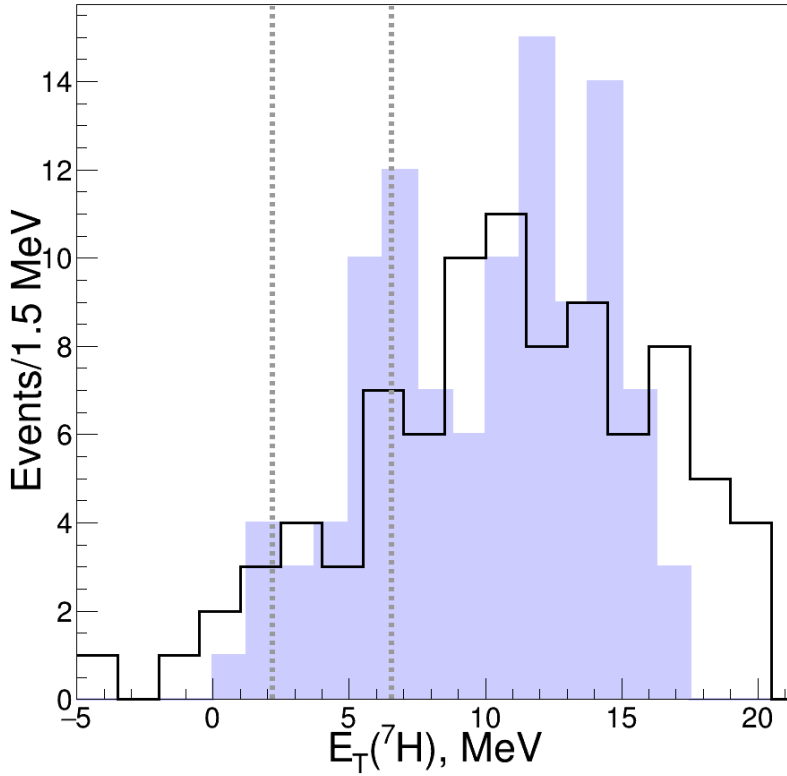
Figure 30: The black histrogram is the ^{7}H missing mass spectrum, reported in Ref. [45], which is drawn on a blue background of the Ref. [91] result. The same as in Fig. 29 b) two vertical dotted lines correspond to the reported in work [91] states.

high energies meaningless for interpretation. The blue dashed line in Fig. 29 illustrates the contribution of the five-body $t+4n$ phase space to the obtained ^{7}H spectrum.

The observed ^{7}H first excited state also fits the systematics of the lowest excited states of all light nuclei with the closed $p_{3/2}$ neutron orbital, for more details see Ref. [91]. This not only proves the presence of the 6.5(5) MeV resonance, but also can be considered as an additional argument supporting our interpretation of the low lying events indicating the ^{7}H ground state at 1.8 MeV above the decay threshold. The cross section angular dependence of observed excited state population is shown in Fig. 31a). The obtained distribution was expected to be not that much angular dependent as the one, shown in Fig. 9 for the ground state. That is why, such analysis could only be the test of data reliability. The calculation results for the suggested ^{7}H $3/2^+$ and $5/2^+$ excited states are shown in Fig. 31b). The population of these states goes via the proton transfer from the ^{8}He(2^+) state appearing due to the collective excitation with β_2=0.45.

Eventually, all the presented results allowed us to claim that for the first time the ^{7}H excited state was observed at $E_T = 6.5(5)$ MeV of the 2 MeV width. The observed peak was formed by 27 events of ^{3}He-^{3}H coincidences satisfying the triton kinematic selection, see Fig. 29 a). In the center-of-mass frame of reference of the ^{2}H(^{8}He,^{3}He)^{7}H(g.s.) binary reaction all events were registered in the 10°-45° angular range. Taking into account the geometrical efficiency of the detector system, the cross section of the found excited state population was $\sim$30 μb/sr.

As for the desired ground state, 5 collected events have been collected, indicating its pop-

43
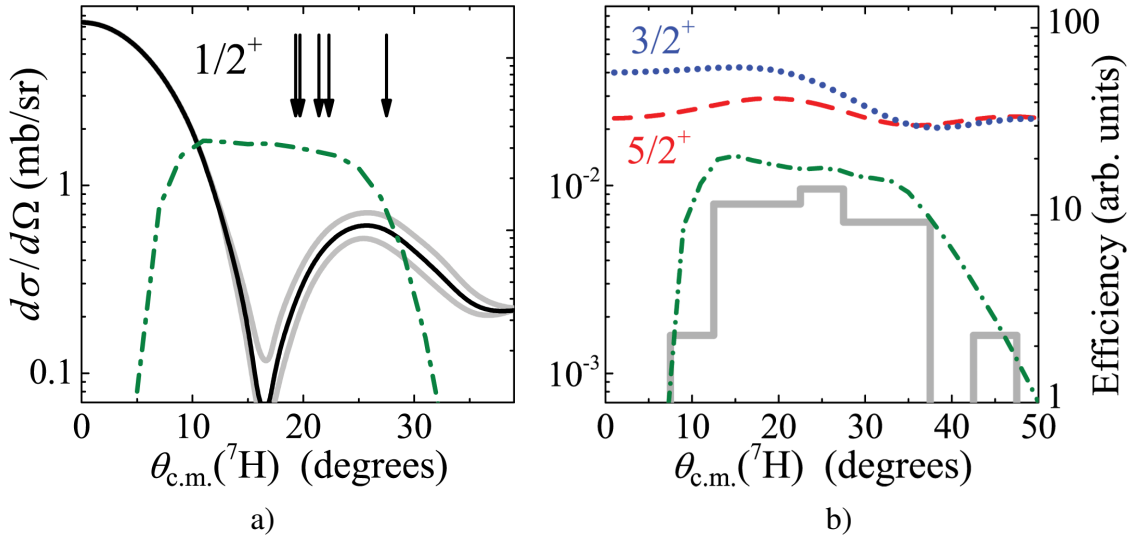
Figure 31: The angular distributions calculated for the ^{2}H(^{8}He,^{3}He)^{7}H reaction channel for both ground and first excited states. a) The angles of the five registered ^{7}H ground state candidate events are indicated by arrows in the right figure. The gray curves in the right figure show the $1/2^+$ cross section for ± 300 keV variation of the ^{7}H ground state energy. The green dash-dotted curves, drawn in both figures, associated with the arbitrary-scale right axes, show the calculated setup efficiency for the registration of ^{7}H with E_T=1.8 MeV and E_T=6.5 MeV, respectively. b) The gray histogram in the right figure shows (in arbitrary units) the experimental angular distribution in the E_T=5–8 MeV range for the collected 27 events, corresponded to the observed first excited state.

ulation at 1.8 MeV above the five body decay threshold. As it was expected, all of them are characterized by the very forward angles of the binary reaction. The total cross section at angles $17°$-$27°$ in the center of mass system turned out about 25 μb/sr. This corresponds to a weak population of the ^{7}H ground state with experimental spectroscopic factor of 0.1. The explanation of such unexpected extremely low cross observed section is that all the ^{7}H ground state candidate events, shown by arrows in Fig. 31 b), are located in the area of the second diffraction maximum. It can be seen that all events are concentrated in the region predicted to be the second diffraction maximum for the calculated cross section of the $1/2^+$ state. In principle, one might expect the detection of the same number of the ground state events in the range of $6° < \theta_{c.m.} < 12°$. However, we do not think that the nonobservation of events in this region is an important fact. The position of the first cross section minimum varies within $1.5°$ in our calculations, that is why the absence of the events in the first diffraction maximum, which was supposed to be covered by layout of the side telescopes, see Fig. 9, leads to assumption that the first minimum actually is located at lower angles as it was expected. Such a small angle of the first diffraction minimum might also provide an evidence for the extreme peripheral character of the ^{7}H ground state population in the studied ^{2}H(^{8}He,^{7}H)^{3}He reaction. That is why, the obtained results also clarifies why the task of search for the ^{7}H ground state task remained relevant for more than 50 years and required so much time and efforts without bringing reliable assignments of such a remote isotope.

8 Results: experiment 2. d-^{3}He channel for ^{7}H population

During the second experimental run the ^{8}He secondary beam had the same properties (energy, purity, intensity) as in experiment 1. However, the two times longer beamtime allowed one to increase the integral flux of the ^{8}He particles up to $\sim 25 \cdot 10^9$. During the measurements conducted with the empty target the integral of the ^{8}He particles turned out $\sim 4 \cdot 10^9$. As it was mentioned in chapter 3.2.2, the performed detector setup modifications, in conjunction with the achieved beam integral, promised to increase the statistics by the factor of 2.5. However, instead of the expected ≈ 280 ^{3}He-^{3}H coincidences, during the second run, we have registered 404 such events. This was mainly caused by the improved energy resolution of the detector systems, and hence the particle identification quality. The latter, once again, demonstrates the impact of the reference measurements, which allowed to check and slightly correct some of the initial setup information (mostly the detector and target positions).

The collected statistics allowed to perform more detailed analysis, including several gate conditions which we could not apply to the data from the first run. The most important and informative data surveys of the reconstructed ^{7}H spectrum are given in Fig. 32. From these spectra we assign the ^{7}H ground state at $E_T =2.2(3)$ MeV, the first excited state at 5.5(3) MeV, and the higher-energy resonances at 7.5(3) and 11.0(5) MeV.

Comparing to the first run, the second one was characterized by the considerably smaller background, i.e. $\sim 8\%$ of ^{3}He-^{3}H coincidences. Fig. 33 and the factorized missing mass spectrum given in Fig. 32 b) with green histogram, shows the collected data with the empty target in two main correlations: triton kinematical triangle and the correlation of the center-of-mass binary reaction angle with the calculated missing mass energy. In the distribution of empty target events, see Fig. 33 a), a "dangerous region" can be spotted with $7.5 < E_T < 10.5$ MeV. Fortunately, these events are all concentrated in a certain angular range $18° < \theta_{cm} < 35°$. Concentration of empty target events in this area can hardly be explained by statistical fluctuations, see the distribution of the complete data in Fig. 32 c). This situation was one of the reasons, motivating to avoid the "dangerous region" in the interpretation of the data and enhance the confidence in the rest of the data. As in the experiment 1, the correlation presented in Fig. 32 a) shows that the majority of data satisfies the kinematics condition, and therefore is in agreement with the idea of the experiment assuming the definition of ^{7}H by its missing mass measurement and its subsequent decay with the emission of ^{3}H.

At first glance, the declared resonance features in the ^{7}H missing mass spectrum in Fig. 32 b) are not very pronounced. In order to make it clear the reconstructed spectrum was studied based on two suggestions: either the presented structures are formed by the broad overlapping resonant states or by the combination of the background contribution and statistical fluctuations in conjunction with the detection efficiency cutoff.

Let us try to interpret the spectrum, presented in Fig. 32 b), without assumption about the population of the declared resonant states. The possible statistical fluctuations are tested analyzing the ^{7}H missing mass spectrum in different representations with the varied binning factors and bin offsets. The ^{7}H decay events with $\theta_{cm} < 18°$ were selected, see Fig. 32 c), and we

a) Kinematic triangle

b) Spectrum for 4/7 cut-off

c) Reaction angle correlation

d) Spectrum with angular cut-off
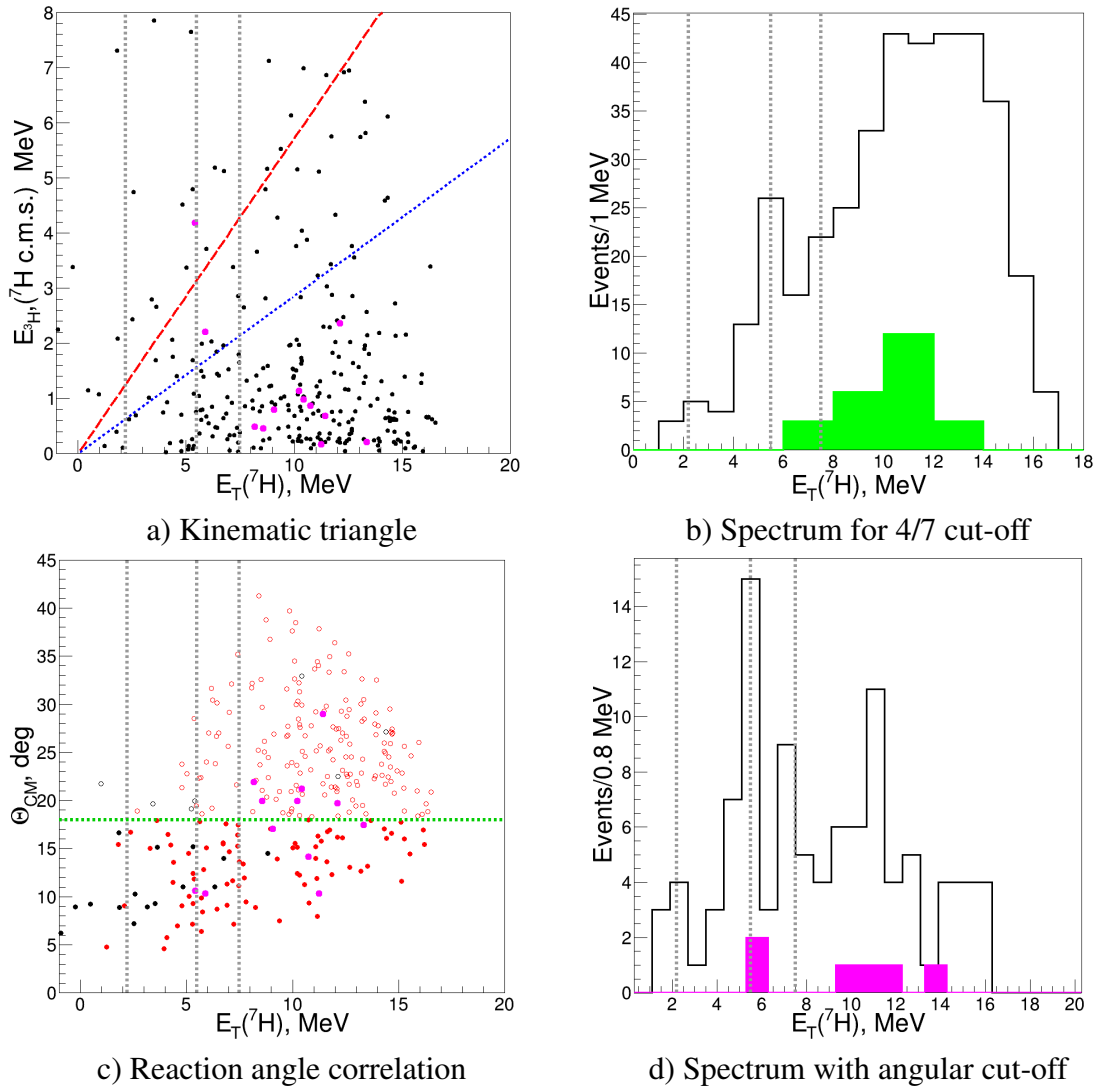
Figure 32: a) Correlation between the ^{3}H energy in the ^{7}H frame and the ^{7}H decay energy derived from the data of experiment 2 (black circles). The large magenta circles show triple coincidence ^{3}He-^{3}H-n events. As in Fig. 29 a), the red and blue lines correspond to 4/7 and 2/7 kinematical borders. b) The ^{7}H missing mass spectrum, reconstructed from events satisfying the triton kinematical triangle condition with cutoff $E_{3H} < 4/7E_T$. The green-filled histogram shows the background normalized by the factor of beam integral ratio (≈ 6.6 in our case). c) Correlation between the center-of-mass reaction angle and the ^{7}H excitation energy. The horizontal green dotted line shows the applied gate for the selection of the small center-of-mass reaction angles events ($\Theta_{CM} < 18°$), see solid and open circles. The large magenta circles show triple coincidence ^{3}He-^{3}H-n events. The red color circles relate to the events within the "kinematical triangle"; the black ones show the rest of the data. d) The ^{7}H missing mass spectrum constructed from the events satisfying both, the kinematic triangle and small reaction angle gates. The magenta-filled histogram indicates the triple coincidence ^{3}He-^{3}H-n events. The vertical gray dotted lines indicate the assumed positions of the ^{7}H resonant states (2.2, 5.5 and 7.5 MeV).

accordingly split the data in two parts in Fig. 34. One motivation for $\theta_{cm} = 18°$ selection is illustrated in Fig. 12: the best energy resolution of the ^{7}H spectrum is obtained for the small center-of-mass reaction angles, and it considerably deteriorates at larger angles. The selected $\theta_{cm} < 18°$ range is also consistent with the cutoff needed for the elimination of the "danger-
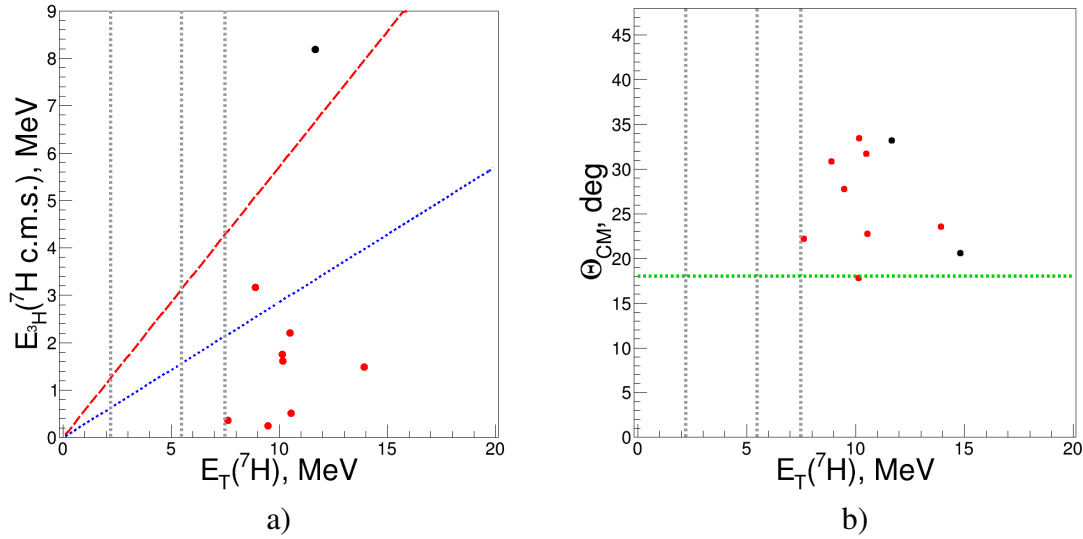
Figure 33: Data obtained with the empty target in the second experiment for E_{3H} vs. E_T for ^7H in the left figure a) and θ_{cm} vs. E_T in the right figure b). The same as in Fig. 32 vertical gray lines indicate the assumed positions of the ^7H resonant states. In both figures the red dots show the distribution for the events within the "kinematical triangle", see Fig. 32; additional black dots show the rest of the data. The green dotted line in corresponds to $\Theta_{CM} < 18°$ and, as in Fig. 32 c) shows the used border of the small center-of-mass reaction angle.

ous background region" specified in the measurements with empty target, see Fig. 33 b). For $\theta_{cm} < 18°$ the three resonant structures at 2.2, 5.5, and 11 MeV are well identified in all representations in Fig. 34. The evidence of the 7.5 MeV peak may be statistically insignificant in some representations, but it is typically present. So, the assumed resonant structures are at least not the statistical artefacts of the histogram arrangement. The spectra with the $\theta_{cm} > 18°$ selection gate are dominated by a smooth "phase volume"-like contribution. Only the 5.5 MeV peak can be clearly seen on the top of the smooth component. Some resonance contributions can be suspected at energies $E_T > 10$ MeV, but their manifestation on the top of the large smooth component is statistically insignificant.

Then we turn to statistical analysis. It shows that the description of each spectrum in Fig. 32 merely by some smooth underlying continuum is possible with values of root-mean-square deviation (RMSD) for the spectrum in Fig. 30 with RMSD ~ 1, for the spectrum in Fig. 29 b) with RMSD $\sim 1 - 2$, for both spectra in Fig. 32 with RMSD $\sim 2 - 3$. These are statistically tolerable values of the mismatch, which does not exclude a "smooth scenario". However, the following general points should be clarified.

If the real spectrum of ^7H is smooth, then, due to the small-statistics data, a purely random mockup of several peaks is possible. In such a case data with very large statistics (e.g. $10^3 - 10^4$ events) are required in order to exclude such accidental "resonances" with a high confidence level. In contrast, if the real ^7H spectrum contains narrow resonant peaks, then reliable identification of these resonant states becomes possible even with few measured decay events. We assume that the $1/2^+$ ground state of ^7H and the lowest excitations, such as $5/2^+-$ $3/2^+$ doublet are located at $E_T < 10$ MeV. The width estimates for such ^7H states provided in the related article [93] show that the widths are likely to be quite small with the expected values
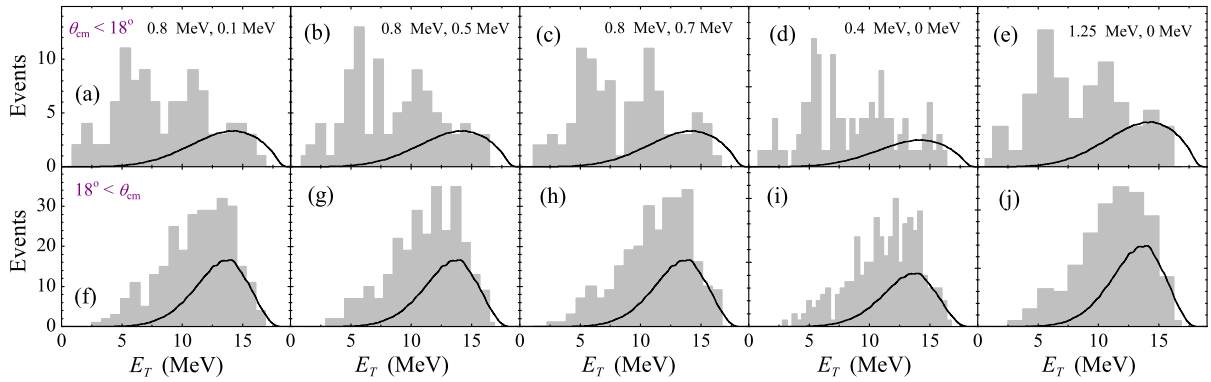
Figure 34: Different representations of the experiment 2 ^{7}H missing mass spectrum selected in two center-of-mass angular ranges: the top row shows events selected by the gate $\theta_{cm} < 18°$, the bottom row shows spectra selected by $\theta_{cm} > 18°$. The binning factor and bin offset are shown for each column in the top row. The "phase space" curves $d\sigma/dE_T d\Omega \sim E_T^5$ with experimental bias accounted by Monte-Carlo procedure are shown in the both rows (normalization is arbitrary).

of $\Gamma \lesssim 1\,\text{MeV}$. So, the narrow resonant-state scenario seems to be physically reasonable and even unavoidable, at least for $E_T < 10\,\text{MeV}$.

We may claim that the same peaks may be spotted in all three experimental datasets of the ^{2}H(^{8}He,^{3}He)^{7}H reaction, see Figs. 29 b),30,32 b). The individual statistics of the datasets of the order $100 - 400$ events can not exclude a pure statistical origin of these peaks in each case. However, it is extremely improbable that the same statistical artefacts could arise in the three different, totally independent experiments (works [45], [91] and [92]). This is a strong general argument supporting the data interpretation of this work. Below we provide an in-depth view in different aspects inherent to each structure and also demonstrate that all these aspects can be interpreted in a consistent way.

8.1 Ground state at 2.2 MeV

The events with $E_T < 3.2$ MeV were selected as candidates to represent the ^{7}H ground state. There are 9 such events with the mean energy value of 2.2 MeV and the dispersion of 0.6 MeV. These values agree well with the results of experiment 1 reported in Ref. [91], where the ^{7}H ground state energy $E_T = 1.8(5)$ MeV was obtained. The events are well separated (there is $\sim$ 0.5 MeV gap) from nearest event connected with the higher ^{7}H excitation. There are 4 possible reasons to get these events here: (i) background events, (ii) "contamination" by events from higher excitations of ^{7}H, (iii) some smooth phase-space distribution, (iv) narrow resonant state. We insist on option (iv), but we have to comment on the other points as well.

(i) Possible background contribution in the E_T region of interest can be estimated based on the empty target measurements. No background events were observed in proximity, see Fig. 33 (a,b). Another way is to estimate it from the density of background counts beyond the kinematical triangle in Fig. 32 a). Here we can expect ~ 1 background event in the 2.2 MeV group.

(ii) The observed width of the 2.2 MeV event group is assumed to be entirely defined by the

energy resolution of the experiment. This is true even if the intrinsic width of this state is larger by a factor $100 - 500$ as compared to the theory estimate giving $\Gamma \lesssim 1\,\text{keV}$ for the ^7H ground state [93]. The discussion of the energy profiles of the ^7H first excited state is provided in the next Section and in Ref. [93]. Various theoretical estimates agree that there should be an empty "window" between the ground state and the first excited state from $E_T \sim 3\,\text{MeV}$ to $E_T \sim 4.0 - 4.5\,\text{MeV}$. Any events emerging in this energy range should be connected with backgrounds or/and the poor missing mass resolution. The Monte-Carlo simulations of the ^7H missing mass spectrum are shown in Fig. 37. They confirm that even the poorly populated ^7H ground state can be reliably separated from the "tail" of the first excited state, and that such a separation is the best for small angles in the center-of-mass frame of reference of the $^2\text{H}(^8\text{He},^3\text{He})^7\text{H}$ binary reaction.

(iii) The phase space for the true core+4n decay at $\sim 2.2\,\text{MeV}$ is

$$dW/dE_T \sim E_T^7. \tag{3}$$

The ordinarily expected five-body phase space is $\sim E^5$, but the antisimmetrization requirement among four neutrons modifies it to formula (3), see [90]. At about $2.5 - 3\,\text{MeV}$ a turnover may occur from the true 4n emission to the sequential emission via the ^5H ground state (located at about $1.8\,\text{MeV}$ above the $^3\text{H}+n+n$ breakup threshold [35, 94]). After that the dependence

$$dW/dE_T \sim E_T^2, \tag{4}$$

is expected. In any case, the "phase space" behavior that can be expected for^7H is a strongly growing function of energy, not something smoothly rising from the threshold.

An additional support for the interpretation of the group of events at $2.2\,\text{MeV}$ as a resonant state is provided by three types of distributions which were analyzed for the events of the $2.2\,\text{MeV}$ group: (i) ^7H center-of-mass angular distribution of the binary reaction, (ii) ^3H energy distribution in the ^7H frame (iii) ^3H lab system angular distribution relative to the ^7H flight direction. Statistics, which we have for the ground-state candidate events is small. However, all the mentioned distributions demonstrate correlated character, expected for the ^7H ground state decay, in contrast with the casual behavior expected for background events.

8.1.1 Center-of-mass reaction angle distribution

The center-of-mass angular distributions for the $^2\text{H}(^8\text{He},^3\text{He})^7\text{H}$ reaction are further discussed in Section 8.5. Here we comment on the distribution of the $2.2\,\text{MeV}$ event group.

In the group of events, declared as the ^7H ground state, there is a gap from $9.5°$ to $15.5°$, see Fig. 32 c). This feature is consistent with the results of the first experiment, see Fig. 31 b), where 5 ground candidate events were localized in the range $18° < \theta_{\text{cm}} < 27°$. Such observed angular distributions can be problematic from the point of view of theoretically predicted angular distributions because theory typically predicts the diffraction minimum at $\theta_{\text{cm}} \sim 16° - 18°$. Considerably lower values $\theta_{\text{cm}} \sim 13° - 14°$ are suggested by the data. If the latter is true, then

the observed angular distribution provides important tip for the following problems. Here we once again should pay attention to the results of the first experiment, described in Section 3.2.1. (i) Although, the detector system allowed to register the ^{7}H ground state events in angular range $\theta_{cm} > 6°$ covering the predicted first diffraction maximum, see Fig. 9, all the collected events were located at higher angles, see Fig. 31 b). The suggestion made was that the actual diffraction minimum covers a range of $10° < \theta_{cm} < 18°$.

(ii) the DWBA/FRESCO calculations with standard parameters fail to provide the diffraction minimum at $\theta_{cm} \sim 13° - 14°$. Such an angle of the minimum might provide an evidence of the extreme peripheral character of the ^{7}H ground state population in the ^{2}H(^{8}He,^{3}He)^{7}H reaction. Such an extreme peripheral character of the reaction gives a natural explanation of the extremely low cross section observed for the ^{7}H ground state population (~ 25 μb/sr within the angular range $\theta_{cm} \sim 17° - 27°$). See also Ref. [93] for extended discussion of this point.

How statistically significant is the $\theta_{cm} \sim 9.5° - 15.5°$ gap in the ground state angular distribution? One can assume, that the actual angular distribution is homogeneous, and experimental efficiency is constant and nonzero in the ranges $\theta_{cm} \sim 8° - 26°$ and $\theta_{cm} \sim 6° - 24°$ in the experiments 1 and 2, respectively. In that case, the estimated probability of non-population of the $\theta_{cm} \sim 9.5° - 15.5°$ range in both the experiments simultaneously is $\sim 0.5 - 1\%$. So, it is very unlikely that the experimentally observed patterns are generated by some featureless distribution because of statistical fluctuations. The interpretation by assigning the diffraction minimum at $\theta_{cm} \sim 13° - 14°$ is, thus, quite natural.

The best energy resolution of the ^{7}H ground state can be expected for the small-angle events from the first diffraction maximum. Indeed, by selecting 4 events with $\theta_{cm} < 10°$ we obtain a bit different mean energy $E_T = 2.1$ MeV and dispersion of 0.55 MeV (compared to results with the complete data). The dispersions of the ground state events for the small θ_{cm} (0.55 MeV) and for the complete data (0.6 MeV) are consistent with the Monte-Carlo estimated energy resolutions, see Table 1.

8.1.2 ^{3}H energy distribution in the ^{7}H rest frame

The emission dynamics of the true $4n$ nuclear decay is still a completely unexplored phenomenon. Our data for the first time provide access to this type of information. The commonly expected energy distribution of the ^{3}H fragments emitted at the ^{7}H ground state decay has the shape of a 5-body "phase space"

$$\frac{dW}{d\varepsilon} = \sqrt{\varepsilon(1-\varepsilon)^7}, \quad \varepsilon = \frac{7E_{3H}}{4E_T}, \tag{5}$$

where E_{3H} is the energy of ^{3}H in the ^{7}H rest frame. This distribution suggests that $\sim 92\%$ of events are located below $\varepsilon = 1/2$ and the mean ^{3}H energy value $\langle \varepsilon \rangle = 1/4$. Moreover, a realistic energy distribution obtained in the 5-body calculations of Ref. [81] has even more correlated character, with $\langle \varepsilon \rangle \sim 0.21 - 0.22$ for $E_T \sim 2 - 3$, see Fig. 35. This happens because in the decay via emission of 4 neutrons, at least 2 additional excitation quanta in the "neutron part"
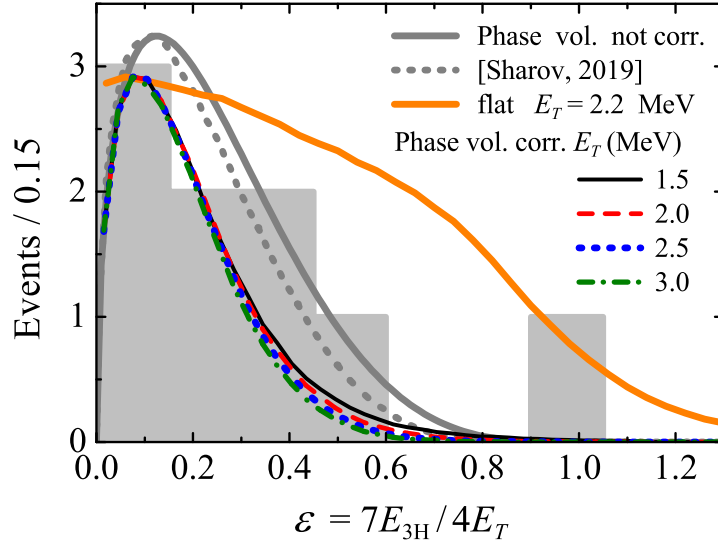
Figure 35: The energy distributions of the ^{3}H fragment in the ^{7}H center-of-mass: experiment (the ^{7}H ground state candidate events with $E_T < 3.2\,\mathrm{MeV}$) vs. Monte-Carlo simulation results for phase volume distribution of Eq. (5) at different decay energies of ^{7}H. The gray solid and dotted curves show (colors refers to different E_T values) theoretical (not corrected for experimental bias) phase volume distribution and realistic distribution from work [81], respectively.

of the wave function are needed to enable the antisymmetrization of the wave function. In this distribution $\sim 95\%$ of events are located below $\varepsilon = 1/2$. The regions where the absolute majority of the "physical" events should residue according to the above "phase space" argument are separated by the "$E_{3\mathrm{H}} = 2/7E_T$" lines in Figs. 29 a), 32 a) and 33 a).

Thus, the events with $\varepsilon > 0.5 - 0.6$ should be connected either with some sort of background or with poor resolution for the reconstructed energy of ^{3}H in the center-of-mass of ^{7}H, populated in the ^{2}H(^{8}He,^{3}He)^{7}H reaction. The observed ^{3}H energy distribution for the expected ^{7}H ground state events is shown in Fig. 35. This energy distribution is consistent with the expected correlated emission and highly inconsistent with uncorrelated situation, see the orange curve called "flat". The numerical information is also provided in Table 2. A more detailed discussion of the ^{3}H energy distributions is provided in Ref. [93].

8.1.3 ^{3}H-^{7}H angular distribution in the lab frame

From theoretical point of view, this distribution is directly connected with the energy distribution of ^{3}H in the ^{7}H frame discussed above. Moreover, it is obtained by projecting the ^{3}H momentum distribution on the transversal plane. However, from experimental point of view, this distribution is derived in methodologically different and more safe way because a reconstruction of the ^{3}H energy is not needed, only the reconstruction of ^{3}H direction. The Monte-Carlo calculations evaluated resolution of this angular distribution as quite good $\Delta\theta_{3\mathrm{H}\text{-}7\mathrm{H}} \lesssim 0.4°$.

The ^{3}H angular distribution relative to the ^{7}H direction in the lab frame in the experiment 2 is shown in Fig. 36 together with different predicted distributions. From this figure one may conclude that the experimental distribution is clearly inconsistent with the smallest considered
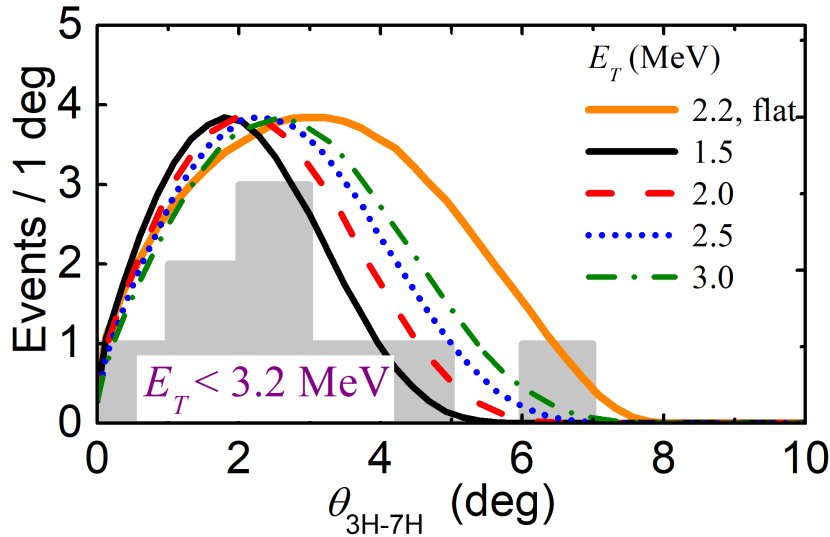
Figure 36: The angular distributions of ^{3}H fragments in the lab frame relative to the ^{7}H center-of-mass momentum vector. The ^{7}H ground state candidate events with $E_T < 3.2$ MeV are selected. a) Experimental data and theoretical predictions with experimental bias taken into account by Monte-Carlo simulation. b) Initial theoretical distributions based on phase volume are shown by colored dotted curves, and are presented for different excitation energies.

energy $E_T = 1.5$ MeV and with an uncorrelated distribution ("flat" curve). Finally, from information given in Table 2 one can find that both the energy and angular distributions of ^{3}H are consistent with the $E_T = 2.2(5)$ MeV energy inferred from the missing mass data.

8.2 First excited state as a doublet at 5.5 MeV and 7.5 MeV.

In the first experiment, the first excited state was found as a peak at ~ 6 MeV, with a possible interpretation as a $5/2^+$–$3/2^+$ doublet, see Section 7. For the discussion of this Section, we should assume (i) the possible width of the state and (ii) the profile of the resonance peak, which is also induced by this width. The relevant theoretical estimates are provided in Ref. [93]. Contrary to the ^{7}H ground state, which has a unique true $4n$ emission decay channel, the components of the $5/2^+$–$3/2^+$ doublet, located above $E_T \sim 4$ MeV, may undergo sequential emission of 2 neutrons via the ground state of ^{5}H: ^{7}H $\rightarrow$ ^{5}H+$2n$ $\rightarrow$ ^{3}H+$4n$. The alternative single neutron emission channel is assumed to be closed, because no ^{6}H states available for the sequential decay ^{7}H$\rightarrow$^{6}H+n were found in this work below the 6 MeV energy relative the ^{3}H+$3n$ threshold.

We start with overall "pessimistic" estimates for the resonance profile. The upper-limit width value of the sequential decay of the "2^+" state at 5.5 MeV via the ^{5}H ground state is

Table 2: Mean values of the ε and $\theta_{3H\text{-}7H}$ variables for the distributions of Figs. 35 and 36.

Value	flat	1.5	2.0	2.5	3.0	Exp.
ε	0.46(11)	0.28(6)	0.26(6)	0.24(6)	0.23(6)	0.31
$\theta_{3H\text{-}7H}$	3.5(6)	2.3(4)	2.6(4)	2.8(4)	3.0(4)	2.9

determined in Ref. [93] as $\Gamma = 0.75\,\text{MeV}$. We assume a conservative value of $\Gamma = 1.5\,\text{MeV}$. It can be seen in Fig. 37 a) that Lorentzian profile with such a width extends to the ground state position and may "shade" it. However, a realistic resonance profile should be corrected by a function of the width dependence on energy:

$$\frac{d\sigma}{dE_T} \sim \frac{\Gamma(E_T)}{(E_r - E_T)^2 + \Gamma(E_T)^2/4}. \tag{6}$$

Functions of this type were proved to be extremely precise in the description of the resonance profiles of three-body decays, see, e.g., Eq. (24) in Ref. [95] and Eq. (7) in Ref. [96]. The low-energy asymptotics of the "2^+" state should be $\sim E_T^4$. Let's assume the behavior $\sim E_T^3$. The energy resolution for the ground and the first excited states are expected to be ~ 1 and $\sim 0.8\,\text{MeV}$, respectively, see Table 1. Let us take 1.2 and 1 MeV. It can be found in Fig. 37 a) that even the "pessimistic" estimate of the resonance profile results in a pronounced deep between the ^{7}H ground and "2^+" states. So, clear experimental separation of the ground and "2^+" excited states of ^{7}H in our experiment is expected.

Some additional clue on another resonant state can be found on the right tail of the 5.5 MeV peak at about 7.5 MeV in Fig. 34, upper row. It could be just a statistical fluctuation of the data. However, one should keep in mind that if the 5.5 MeV peak is indeed the $5/2^+$ state of ^{7}H, than one may expect the $3/2^+$ member of this doublet to be located $\sim 1 - 2\,\text{MeV}$ above it. According to statistical argument, the $3/2^+$ state population should be two times smaller than the $5/2^+$ population. For the $3/2^+$ state at $E_T \sim 7.5\,\text{MeV}$ with width smaller than $1 - 1.5\,\text{MeV}$ we can show that the doublet components can be resolved by the setup of experiment 2, see Fig. 37 b), red dotted curve. Otherwise, we can expect some quite broad asymmetric "triangular" profile with "shoulder" for the $5/2^+$–$3/2^+$ doublet, see Fig. 37 b) orange dash-dotted curve.

So, we can not discriminate confidently between these two opportunities and contributions just from asymmetric broad right "shoulder" of the 5.5 MeV state, see Fig. 37 a). However, the idea about contribution from the $3/2^+$ doublet state is attractive, since it allows also to explain the disagreement with experiment 1. The $E_T = 6.5(5)\,\text{MeV}$ peak position found in [91] is consistent with the observation anticipated for a unresolved $5/2^+$–$3/2^+$ doublet $E_T = \{5.5, 7.5\}\,\text{MeV}$, as the resolution was considerably worse in experiment 1 compared to experiment 2. It can be found in Fig. 34 that a spectrum, consistent with the results of experiment 1, can be obtained for certain binning conditions, simulating deterioration of energy resolution.

8.3   Group of events at 11 MeV

The 11.0(5) MeV peak is well seen in all the data representations in Fig. 32 (b,d) and 34 (a-e). The search for this state at $\theta_{\text{cm}} > 18°$ loses sense, since this energy-angular range is expected to be contaminated with the background events, see Fig. 33 b). Question could be asked: what could be the nature of such quite a narrow states observed at such a high excitation energy? The disintegration of the ^{3}H cluster into $p+n+n$ is possible above $E_T = 8.48\,\text{MeV}$. Phenomenology of
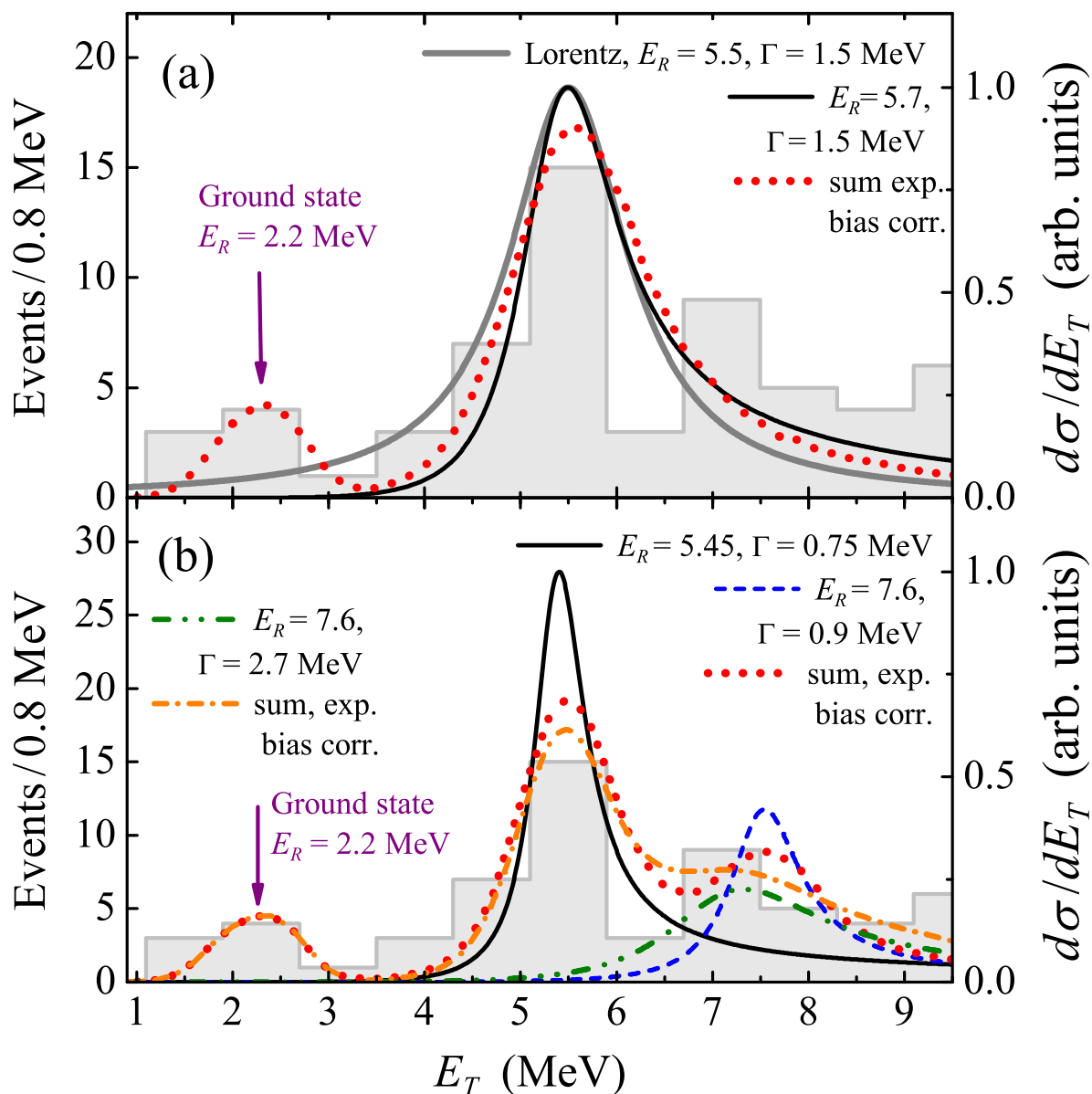
Figure 37: The energy profile of the ground and the first excited state(s) of ^{7}H. a) Broad state case. The gray solid curve shows pure Lorentzian profile with $\Gamma = 1.5$ MeV. The black solid curve shows the realistic profile with $\Gamma = 1.5$ MeV. The red dotted curve shows the realistic resonance profile with experimental resolution taken into account by the Monte-Carlo simulations. b) Narrow states case. Black solid, blue dashed, and olive dash-double-dotted curves show the $5/2^+$–$3/2^+$ doublet with the resonance energies of 5.5 and 7.5 MeV, but with different widths of the $3/2^+$. The red dotted and orange dash-dotted curves show the doublet spectra with experimental resolution taken into account by the Monte-Carlo simulations. The experimental ^{7}H missing mass spectrum with cutoff of the reaction angle $\theta_{cm} < 18°$ is shown in both panels by gray histograms.

nuclear states suggests that the states with definit clusterization are likely to be found near the corresponding cluster disintegration thresholds (both somewhat above and somewhat below). According to this systematics the 11 MeV state can be expected to have the structure with "dissolved" ^{3}H core: $p+6n$. It does not mean that such a state should be necessarily observed in the $p+6n$ decay channel. According to a penetrability argument, the ^{3}H+4n channel should still be a preferable decay path for such a state. Nevertheless, we performed a dedicated search for decay of this state into $p+6n$. Unfortunately, no significant concentration of such events was identified.

8.4 Neutron coincidence events

The neutron wall used in experiment 2 provided 4.5% energy resolution for neutron energy of ~ 1 MeV and the single neutron registration efficiency of $\sim 15\%$. The efficiency of the neutron registration in coincidence with ^{3}H and ^{3}He was around 2% taking into account that four neutrons are produced in each ^{7}H decay event. Such an efficiency is too low to expect statistically significant result. However, these events could be interesting as an additional consistency check of the data, see Fig. 32 a) and d). There are 8 triple-coincidence ^{3}H-^{3}He-n events. There are two events in the $E_T \sim 5.5$ MeV region, one event corresponding to ~ 7.5 MeV structure, and three events consistent with the 11 MeV state.

8.5 Reaction angle correlation

Such distributions of the direct reactions serve as one of standard tools of spin-parity identification in reaction theory. Due to the small statistics of our experiment, angular distributions can not provide a basis for reliable statements, but some conclusive remarks still can be done.

Fig. 32 c) shows the center-of-mass angle of events from the ^{2}H(^{8}He,^{3}He)^{7}H reaction versus the corresponding ^{7}H excitation energy taken from the experiment 2. For $E_T > 10$ MeV the available angular range rapidly shrinks: the kinematical cut defined by the maximum energy $E = 26$ MeV of reliable identification of ^{3}He recoils can be clearly seen. The angular distributions for different energy ranges of ^{7}H are presented in Fig. 38. The efficiency-corrected angular distributions converted to cross section values are shown in the upper panels of Fig. 38.

The angular distribution for the possible ^{7}H ground state energy range, shown in Fig. 38 a), was discussed in Section 8.1.1. Here we would like to point that the deduced cross sections are ~ 24 μb/sr for $\theta_{cm} \sim 5° - 9°$ and ~ 7 μb/sr for $\theta_{cm} \sim 15° - 19°$. For the first excited state, Fig. 38 b), the deduced cross sections are ~ 30 μb/sr for $\theta_{cm} \sim 5° - 18°$ and ~ 11 μb/sr for $\theta_{cm} \sim 18° - 30°$. The energy range $8.5 < E_T < 10.5$ MeV was excluded from consideration, because of the remarkable background found in the empty target experiment, see Fig. 33 b).

In general, we would like to comment the following. Within the available angular range and available statistics, the angular distributions of all the 4 ranges can be seen as qualitatively different. Thus, these distributions support the idea that the considered ranges contain physically different entities.
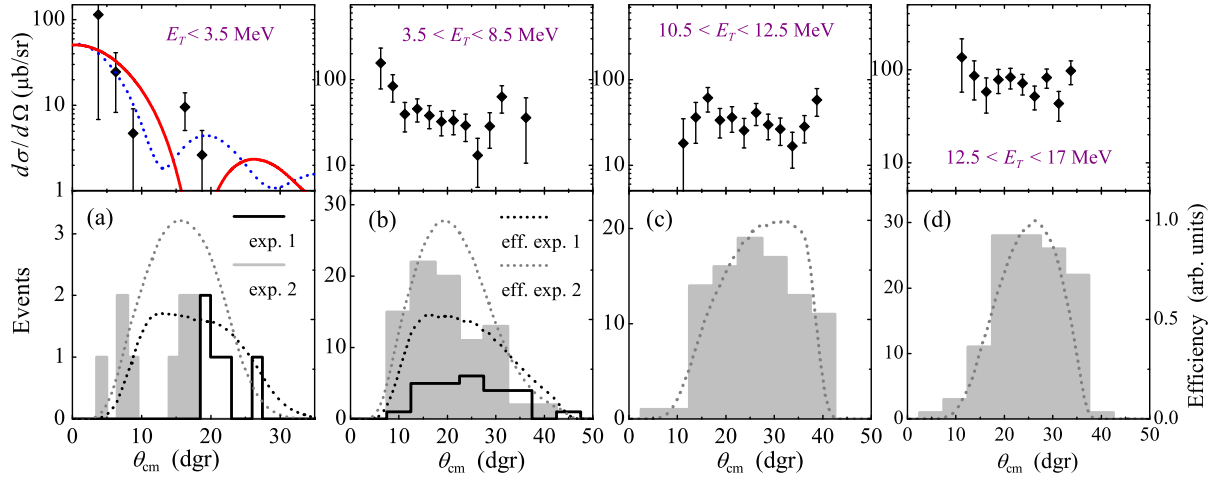
Figure 38: The center-of-mass angular distributions for the ^{2}H(^{8}He,^{3}He)^{7}H reaction in different ^{7}H missing mass energy ranges. Efficiency corrected angular distributions are shown in the upper part of each panel. a) The ^{7}H ground state with $0 < E_T < 3.2$ MeV and $E_{3H} < 4/7E_T$, the hollow black and filled gray histograms shows the data of experiments 1 and 2, respectively. The dotted curves of corresponding color show the detection efficiency which is given on the right axis. The red solid curve shows the FRESCO calculation results with standard parameters, see Section 4, the blue dashed curve shows the result of FRESCO calculation assuming the extreme peripheral transfer (both curves have arbitrary scaling). b) The first excited state (or doublet) with $3.2 < E_T < 8.5$ MeV. c) The 11 MeV excited state with $10.5 < E_T < 12.5$ MeV. d) High-energy part of the spectrum with $E_T > 12.5$ MeV.

8.6 ^{7}H summary

In conclusion, we once again refer to the previous works dedicated to the ^{7}H study. In our experiments the accepted condition of the occurred ^{2}H(^{8}He,^{3}He)^{7}H reaction was the coincidence detection of the recoil ^{3}He together with the ^{3}H nucleus emitted at the ^{7}H decay, and the ^{3}H momentum reconstruction allowed for using the kinematical triangle as a selection gate reduce significantly the missing mass background conditions. The efficiency of using the kinematical triangle selection is demonstrated by the comparison of our present results with the spectra obtained in the previous experiments where the same proton removal from ^{8}He was studied. In experiment [37] only the missing mass of ^{7}H was available, and background conditions were very poor: the missing mass spectrum extended into negative energy region down to -20 MeV, and more than 90% of the data were related to the background in the analysis. In experiment [44] also only the missing mass of ^{7}H was available, and background conditions were poor: the missing mass spectrum extended into the negative energy region down to -3 MeV, and $\sim 75\%$ of the data were related to the background reactions originated from the carbon component of the CD$_2$ target. In experiment [45] the missing mass spectrum, see Fig. 30, of ^{7}H was augmented by the requirement of the ^{3}He-^{3}H coincidence which drastically improved the background conditions. Still, some evidence of the background is visible, since the missing mass spectrum extends into the negative region beyond the values implied by the energy resolution of the experiment. In our experiments, the coincidence with ^{3}H and reconstruction of the ^{3}H momentum allow for using the "kinematical triangle" as a selection gate which reduced

significantly (down to 10% and 8% in our first and second runs, respectively) the background in the reconstructed obtained ^{7}H missing mass spectrum.

The results of two conducted experiments at ACCULINNA-2 are consistent with each other and, moreover, with the previous work [45]. Experiment one allowed to observe the first excited state as a bump at ~ 6 MeV and to get evidence for its ground state at ~ 2.2 MeV above the decay threshold into t+4n. In experiment 2 we collected the record statistics for the ^{2}H(^{8}He,^{3}He)^{7}H reaction (378 events). This allowed us to observe *four* peaks in the reconstructed missing mass spectrum of ^{7}H at 2.2(5), 5.5(3), 7.5(3), and 11.0(3) MeV. For each of these three datasets, because of the limited statistics, it is not impossible that these peaks are induced by statistical fluctuations on a top of some smooth continuous spectrum starting from $E_T \sim 5$ MeV. However, it is virtually impossible for statistical fluctuations to cause peaks at the same energies in the three totally independent experiments.

The observed ^{7}H ground state is populated with very low cross section in the ^{2}H(^{8}He,^{3}He)^{7}H reaction. So, our special concern in this work were the background conditions in the low-energy part of the obtained spectrum and the energy-resolution issues, which might make "contamination" in the ground state range by events from the higher-lying ^{7}H excitations. Both these aspects were found to be favorable for the ^{7}H ground state identification even by few events. All the observed in two experiments ground state events are consistent with the ^{7}H center-of-mass angular distribution expected for the $1/2^+$ ground state with diffraction minimum located between $\sim 10°$ and $\sim 15°$. They are also consistent with predicted energy distributions of the ^{3}H fragment in the ^{7}H center-of-mass system.

Summarizing, the conclusion about the observation of the ^{7}H states at 2.2(5) and 5.5(3) MeV is very reliable. The observation of the 7.5(3) MeV state is not statistically confident enough. Energy resolution of experiment 2 was high enough to resolve the possible 5.5 – 7.5 MeV doublet. However, we can not exclude that the observed separation of the 5.5 – 7.5 MeV peaks is actually a statistical fluctuation on the broad right tail of the 5.5 MeV state. Anyway, we conclude that the firmly ascertained 5.5(3) MeV state is the $5/2^+$ member of the ^{7}H excitation doublet. The 11 MeV peak is well exhibited at the ^{2}H(^{8}He,^{3}He)^{7}H reaction center-of-mass angles $\theta_{cm} \lesssim 20°$ where the available statistics is limited. It is also well seen at higher center-of-mass angles $\theta_{cm} \sim 20° - 35°$. However, in this energy-angular range a strong background contribution is expected, so caution is needed.

9   Results: experiment 2. d-^{4}He channel for ^{6}H population

The breakthrough results on ^{7}H studies were the demonstration of the high quality collected data and the effectiveness of the developed experimental methodics. Based on the latter, another reaction channel of direct transfer of deutron from the ^{8}H beam has been studied. This mechanism leads to the ^{6}H population which can be studied as a missing component of the ^{2}H(^{8}He, ^{4}He)^{6}H reaction. Although, similarly, the events of interest are characterized by the detection of low energy recoil ^{4}He and high energy ^{3}H, the data analysis is complicated by the expected higher level of the background. The reason for this is the high amount of the background ^{4}He, as a doubly magic nucleus. That is why, the missing mass spectrum interpretation required more thorough analysis of all data representations: the empty target events, triple coincidences ^{4}He-^{3}H-n, multiple angular correlations and simulations. As for the reference measurements, the results of the same reaction channel, occurred with the ^{10}Be beam are given in Ref. [97]. The obtained missing mass spectrum of populated ^{8}Li had the expected structure, which proved the effectiveness of the applied methodics for d-^{4}He reaction mechanism and reliability of the total setup calibration. However, due to the high amount of background alphas, originating from other intense reaction channels, the certain ^{8}Li structures were observed only in coincidence with high energy lithium isotopes, detected by the central telescope. The latter, was configured for triton registration in the main experimental run, and that is why did not allow to identify high (up to 320 MeV) lithium isotopes with good efficiency. The latter led to the relatively low collected statistics of the reconstructed missing mass spectrum of ^{8}Li. Never the less, the observed population of ^{8}Li in conjunction with the results, related to the ^{2}H(^{10}Be,^{3}He)^{9}Li reaction, given in Section 6, provided evidences for the data reliability and made the ^{6}H reconstruction method highly promising.

9.1 ^{6}H data

In total, during the main experimental run, we collected 4650 ^{4}He-^{3}H coincidence events, 130 of which are triple coincidences with neutron detection by the stilbene wall. Despite to such record statistics, as it was expected, it suffered from the poor background conditions. This background can be seen in the triton kinematical triangle, see Fig. 39 a), as the strong population of the $\{E_T, E_{3H}\}$ plane beyond the kinematical limit allowed for the ^{2}H(^{8}He,^{4}He)^{6}H reaction (E_{3H} is the ^{3}H energy in the ^{6}H center-of-mass frame). Especially for the low excitation energies, this background can be drastically reduced by using the triton kinematical triangle selection. This selection results in 3850 events shown by red dots in Fig. 39 c). At first glance, no certain resonance structure can be observed even in the ^{6}H spectrum cleaned by the ^{3}H condition (see in Fig. 39 b)). The clear sharp rise is observed in the region beginning at $E_T = 3.0 - 3.5$ MeV and going up to ≈ 6 MeV, where the spectrum remains flat within the energy range extending up to $E_T = 9$ MeV. Obviously, this spectrum shape can not be described just as a contribution of the 4-body phase space volume (see the orange dotted curve in the same panel), indicating the presence of some resonance states of ^{6}H lying at low energy above the ^{3}H+3n decay threshold.

a) Triton kinematical triangle

b) Spectrum for 1/2 cut-off

c) Reaction angle correlation

d) Spectrum with angular cut-off
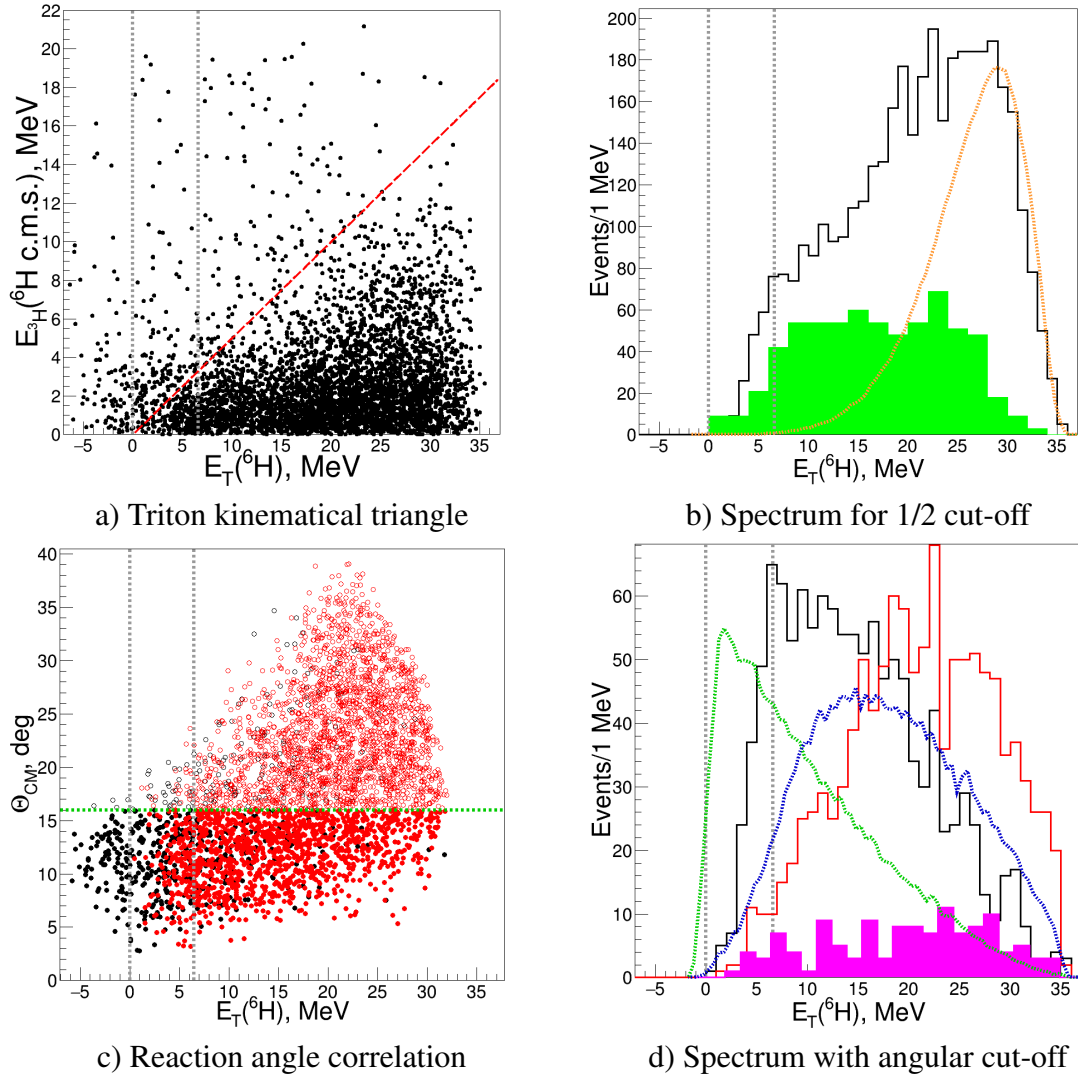
Figure 39: a) Correlation between the ^{3}H energy in the ^{6}H frame and the ^{6}H decay energy, mentioned in text as triton kinematical triangle. The kinematical border showing the $E_{3H} < 1/2E_T(^6$H$)$ relation is shown with the dashed red line. b) The ^{6}H missing spectrum projected from a) by using the triangle gate condition. The green-filled histogram shows the empty target measurement data, normalized by a factor of beam integrals ratio. The orange dotted curve illustrates the 4-body phase volume $\sim E_T^{7/2}$ convoluted with the setup bias. c) Correlation between the center-of-mass reaction angle and the ^{6}H missing mass energy. Events satisfying the triton kinematical triangle gate are colored in red. The horizontal green dotted line shows the condition applied for the selection of the small center-of-mass reaction angle events ($\Theta_{CM} < 16°$), see solid and open circles. d) The ^{6}H missing mass spectra, obtained by the projection of events below and above the green line in panel c). The black and red histograms correspond to the $\theta_{c.m.} < 16°$ and $\theta_{c.m.} > 16°$ selection, respectively. The magenta-filled histogram indicates the ^{4}He-^{3}H-n triple coincidence events. The green and red dotted curves show the calculated efficiency of the ^{4}He-^{3}H coincidence registration at low ($\theta_{c.m.} < 16°$) and high ($16° < \theta_{c.m.} < 22°$) center-of-mass reaction angles, respectively. The vertical gray dotted lines, drawn in all planes, correspond to the zero excitation energy and the suggested position of the ^{6}H resonant state at 6.8 MeV.

The position of the claimed resonance can be estimated by limiting the center-of-mass reaction angles, see the black-line histogram in Fig. 39 d). This limit was chosen based on the behavior of the missing mass spectrum at different angular ranges [97]. First of all, we are

focused only on the low-energy part of the reconstructed spectrum. The discussion of the ^{6}H spectrum obtained at E_T<10 MeV is much more convenient at small center-of-mass reaction angles, see the red-line and green-line dotted curve in Fig. 39 d). The red-line histogram in Fig. 39 d) shows that starting with $\theta_{\text{c.m.}} = 16°$, the reconstructed missing mass spectrum has no resonating behavior, only monotonous growth up to $E_T \sim 20$ MeV. This spectrum follows the behavior of the ^{4}He-^{3}H registration efficiency given by the blue dotted line in Fig. 39 d). This confirms its non-resonance nature. On the other hand, the same argument can not be applied to the black-line histogram being together with the efficiency curve given by the green dotted line. And the fact, that the position of the maximum efficiency value does not correspond to the suggested 6.8 MeV state is another evidence for the resonance existence in close-lying energy range. Here, we also would like to refer to the previous works, where authors claimed the population of ^{6}H at 2.6-2.9 MeV, for example [46, 47, 43]. Although our setup allowed to register such low-energy events, we clearly observe the absence of any possible states below 3.5 MeV. Such observation is an important result, leading to the solution of the questions related to the decay mechanisms of both ^{6,7}H in their ground states.

9.2 Center-of-mass reaction angle distribution

The cross section of the ^{2}H(^{8}He,^{4}He)^{6}H reaction populating the expected low-lying resonant states of ^{6}H was calculated using the FRESCO code for $\Delta l = 1$ momentum transfer provided in Section 4. The calculated cross section angular dependence is presented in Fig. 40. The obtained experimental count rate distribution, also shown in this Figure, demonstrates good agreement with the predicted behavior, see the gray-filled histogram.
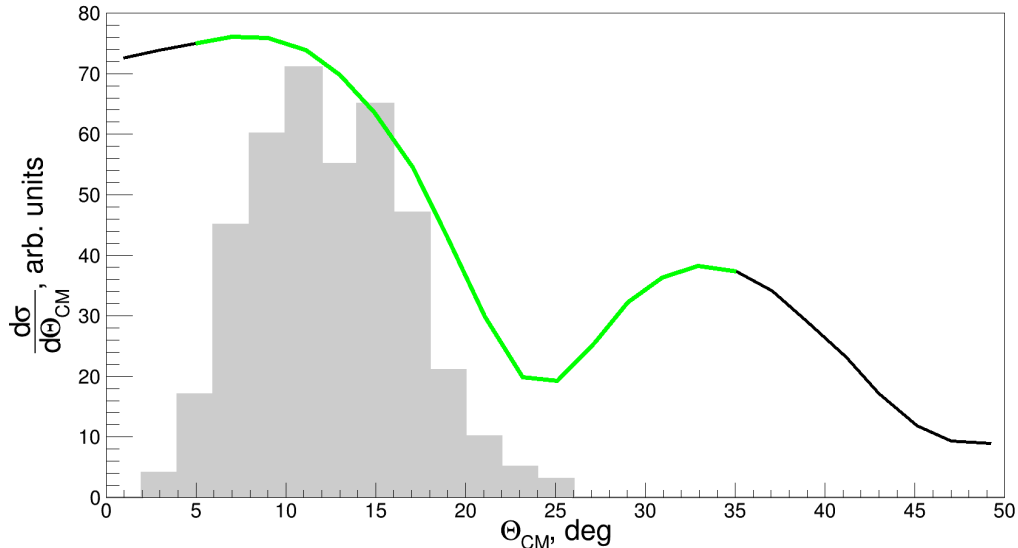
Figure 40: Angular cross section dependence calculated for the ^{2}H(^{8}He,^{4}He)^{6}H(g.s.) reaction. Green color refers to the angle areas covered by the detector setup. The gray-filled histogram shows the obtained in the experiment angular distribution for the low-energy ^{6}H event population (E_T<10 MeV).

Here we would like to mention that the ^{7}H data show the low-angle shift of the expected

diffraction minimum of the corresponded distribution, see Fig. 31 a). Both suggested explanations of this observation, strong absorption or extreme peripheral character of the reaction, lead to the idea that we may expect that such a parameter modification is needed also for the ^{2}H(^{8}He,^{4}He)^{6}H reaction calculations. However, the situation observed in Fig. 40 with diffraction minimum at about $\theta_{c.m.} \sim 24°$ and the hypothetic situation of the diffraction minimum shifted to smaller angles are qualitatively consistent with the observed absence of the 6.8 MeV bump in the experimental missing mass spectrum for $\theta_{c.m.} > 16°$, see the red-line spectrum in Fig. 39 d). Such angular dependence obtained in the range of $16° < \theta_{c.m.} < 20°$ may correspond either to diffraction minimum for the $\Delta l = 1$ cross section, or to the right slope of its low-angle forward peak.

9.3 Empty target subtraction

The background contribution can be further reduced by taking into account the empty target (deuterium gas out) data, see Fig. 41. The empty target measurement collected around 17% of the total obtained beam integral providing 280 events altogether, and 190 events within the triton triangle, presented in Fig. 41 a).

a)   b)
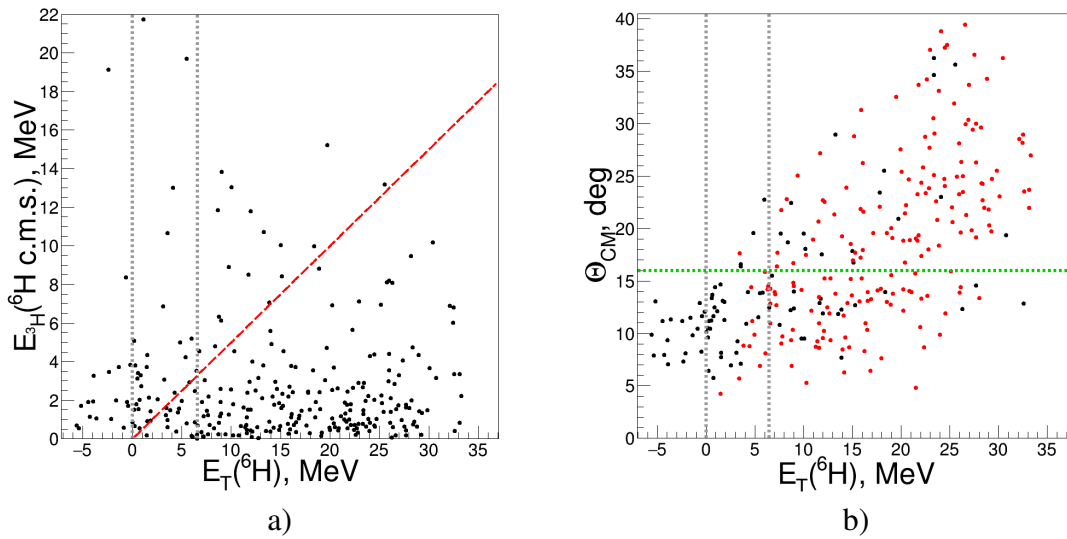
Figure 41: Empty target data for the ^{4}He-^{3}H coincidence events in representation of triton kinematical triangle and reaction angle correlation. a) Correlation between the ^{3}H energy in the ^{6}H center-of-mass frame E_{3H} and the ^{6}H excitation energy E_T. b) Correlation between the center-of-mass reaction angle and the ^{6}H missing mass energy. Those events satisfying the kinematic triangle selection are colored in red. The same as in Fig. 39 vertical gray lines correspond to the peak observed at 6.8 MeV, and to the zero-energy level above the t+3n decay threshold. The selected angular gate, $\Theta_{CM} < 16°$, is shown with the green dotted line.

First of all, we applied the primitive method to background subtraction. The background was subtracted just taking into account the beam integral factor equal to 6.25 in this case. Such subtraction was conducted both for the total spectrum and for its part obtained at low reaction angles ($\theta_{c.m.} < 16°$ (see black-line histograms in Figs. 39 b) and d)). Two resulting spectra of this procedure are presented in Fig. 43 a). The subtraction spectra in the energy range

$3.5 - 10\,\text{MeV}$ are consistent with each other and consistent with the declared $6.8\,\text{MeV}$ bump position as it is seen in the spectrum without any background subtraction. Moreover, all the presented spectra once again show the absence of any possible states below $3.5\,\text{MeV}$. So, the direct background subtraction made both in the total spectrum and in its part obtained at low center-of-mass angles produce consistent results and indicate that we understand the nature of the apparatus-induced backgrounds in our experiment. However, because of the low statistics of the empty target data the E_T bin size was to be set to quite a large value of $3\,\text{MeV}$. Despite the large bin size, the statistical error bars produced by the two used procedures are quite large and do not allow detailed quantitative conclusions. For that reason a more stable background subtraction procedure is developed, which is based on the smooth approximation of the empty target background data.
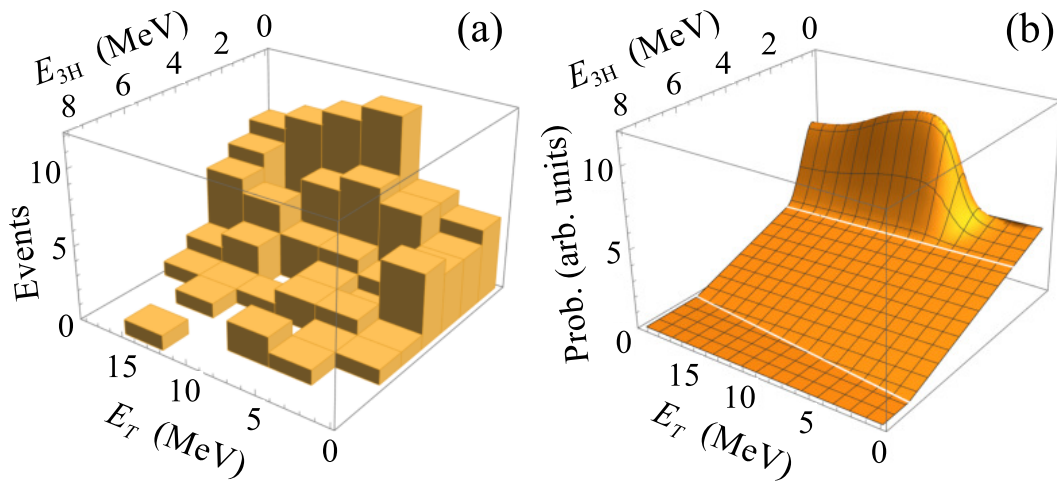
Figure 42: a) Empty target data in the correlation plane $\{E_T, E_{3\text{H}}\}$. b) Empty target data fit by a smooth analytical function.

The second subtraction procedure is conducted in the triton kinematical triangle space and is based on assumption that the empty target contribution is sufficiently smooth in the $\{E_T, E_{3\text{H}}\}$ coordinates. The proper presentation of the empty target data obtained in the triton kinematical triangle are given in Fig. 42 a). For analytical approximation we suggested that this background distribution has two components: the flat component, weakly depending on energy, and the relatively narrow "ridge" at small $E_{3\text{H}}$ values. The obtained smooth analytical function is shown in Fig. 42 b). We have used a Monte-Carlo procedure to subtract it from the experimental data. The subtraction results obtained with the empty-target data normalized to the ^8He incoming beam flux are shown in Fig. 43 b). The $6.8\,\text{MeV}$ bump is clearly seen in the obtained corrected missing mass spectrum. The deduced cross section turned out to be $\simeq 190(40)\,\mu\text{b/sr}$ for the center-of-mass reaction angular range $5° < \theta_{\text{c.m.}} < 16°$. This reasonably large cross section is consistent with the resonant population mechanism. This value is also in a very good agreement with the cross section obtained by FRESCO calculations, see Fig. 40. The steep rise of the spectrum at 3.0-$3.5\,\text{MeV}$ and the broad left tail of the $6.8\,\text{MeV}$ bump provide together an indication that another ^6H state may be located at about $4.5\,\text{MeV}$. These results once again em-

phasize that no indication on the $2.6 - 2.9$ MeV state (the ^{6}H ground state, as suggested in Refs. [46, 47, 43]) is found.
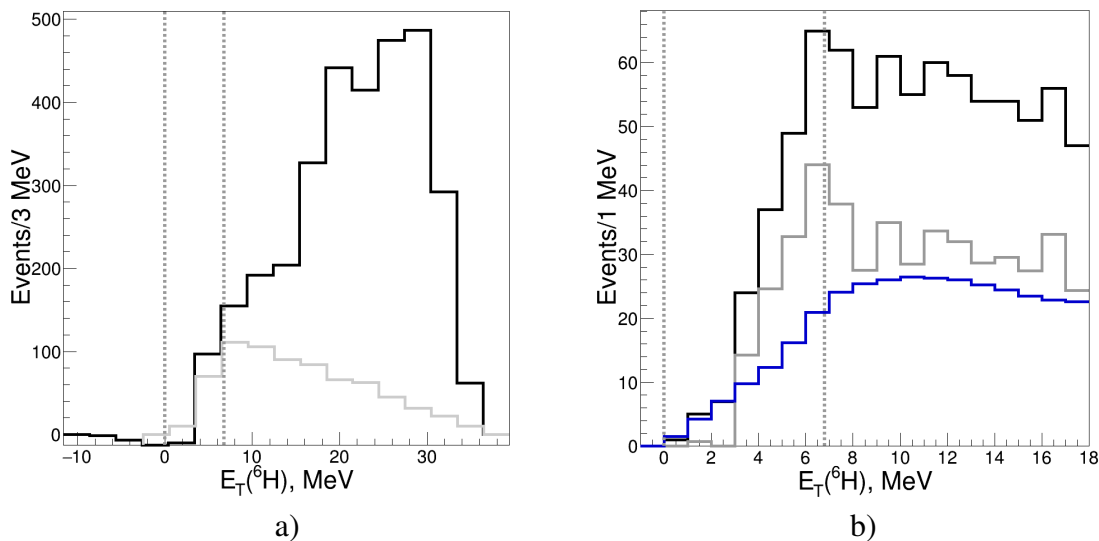
Figure 43: The ^{6}H missing mass spectra obtained after the background subtraction procedures. a) Scaled direct spectrum subtraction. The black- and gray-line histograms relate to the full and low angle ($\theta_{c.m.} < 16°$) data. b) Triton kinematical space subtraction. The black- and gray-line histograms show the spectra obtained before and after the subtraction procedure. The blue-line histogram presents the scaled background spectrum. As in the previous figures, the dotted gray lines correspond to the 6.8 MeV and zero level above the decay threshold.

9.4 Neutron coincidence data

Practically background-free ^{6}H data can be obtained by requesting the measured data coincidence with one of the neutrons emitted in the ^{6}H decay. The data on the ^{4}He-^{3}H-n coincidence events (130 in total) from the ^{2}H(^{8}He, ^{4}He)^{6}H reaction are shown in Fig. 44. Besides the already traditional triton kinematical triangle, here we also use the similarly built neutron triangle, as a correlation of the neutron energy in the ^{6}H center-of-mass frame of reference with the missing mass energy. The spectra in both triangles show that the triple coincidences data are almost free from the background, as far as practically all the events are located in the kinematically allowed region, see Figs. 44 a) and b). To be more specific, the background level of this spectrum can be estimated as $\lesssim 3\%$. The reaction center-of-mass angular distribution of the ^{4}He-^{3}H-n coincidence events is shown in Fig. 44 c). The projected missing mass spectra Fig. 44 d) show the clear evidence of a resonance state at 6.8 MeV. Moreover, the indication on the 4.5 MeV structure can be also found. As in the previous data analysis, data in Fig. 44 does not provide any indication related to the possible existence of the 2.6 MeV state: just one event is found in the 1.5 MeV energy bin around $E_T = 2.6$ MeV, which is statistically not significant to the total 14 events within the $E_T \sim 3 - 8$ MeV energy range assigned to the broad 6.8 MeV peak.
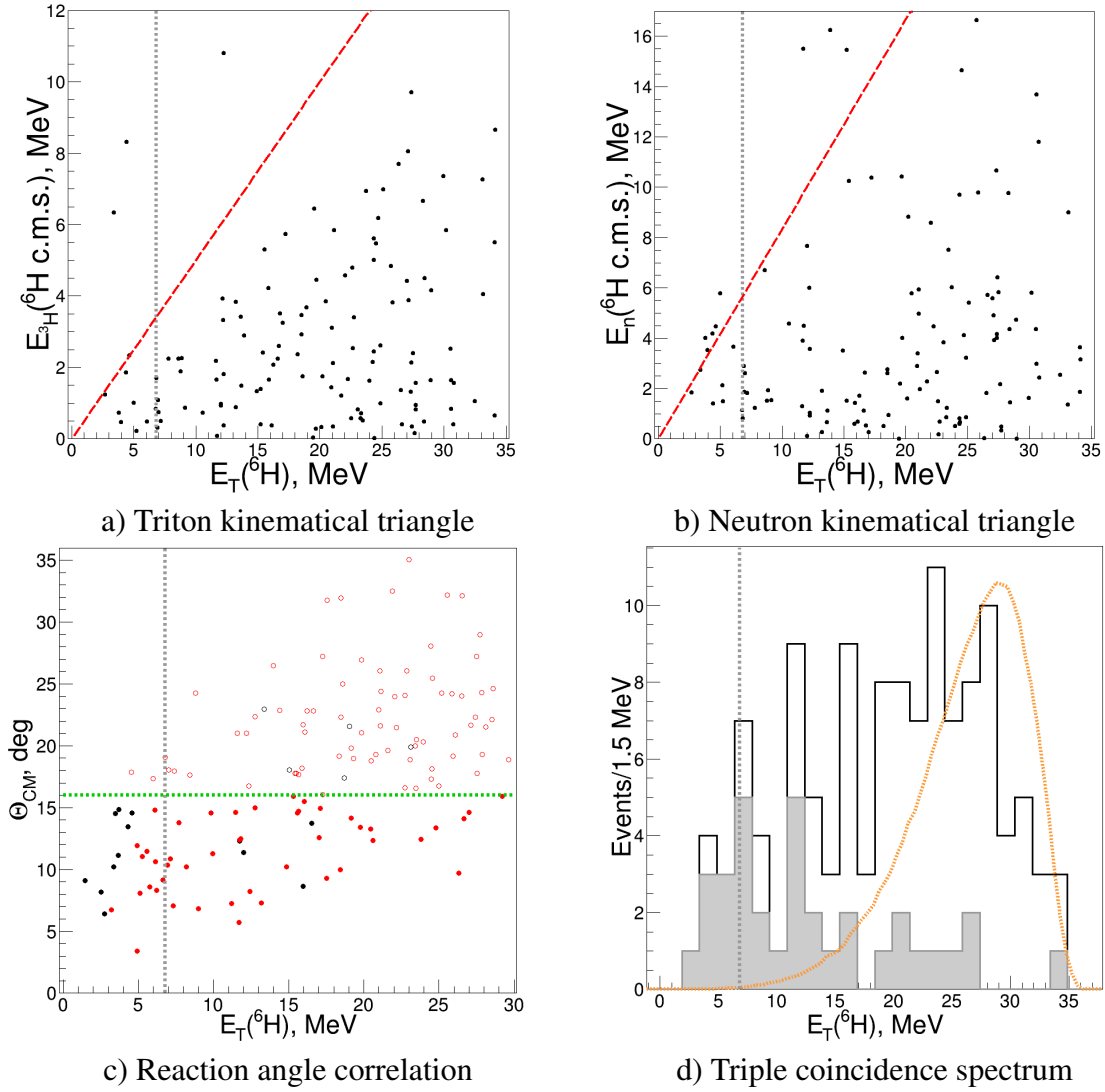
Figure 44: a) Triton kinematical triangle for the triple ^{4}He-^{3}H-n coincidence events. The red dashed line corresponds to the $E_{3H} < 1/2E_T(^6H)$ border. b) Neutron kinematical triangle for triple ^{4}He-^{3}H-n coincidence events. The red dashed line corresponds to the $E_n < 5/6E_T(^6H)$ border. c) Correlation between the center-of-mass reaction angle and the ^{6}H excitation energy. Events inside the triton kinematical triangle gate are colored in red. The horizontal green dotted line shows the applied gate for the selection of the small center-of-mass reaction angle events ($\Theta_{CM} < 16°$), see the solid and open circles. d) The ^{6}H missing mass spectra obtained for all triple coincidences (black-line histogram) and for low-angle events ($\theta_{c.m.} < 16°$). The orange dotted curve illustrates the 4-body phase volume $\sim E_T^{7/2}$ convoluted with the setup bias. The vertical gray dotted lines are drawn in all planes showing the suggested position of the ^{6}H resonant state at 6.8 MeV.

9.5 Background reaction channel correlation analysis

Another important question to be solved, before making missing mass spectrum interpretation, is whether the low-energy structures can be the artifacts, provided by other reaction mechanisms? How can we be sure, that those registered ^{4}He and ^{3}H nuclei were produced in the deutron transfer reaction from the ^{8}He beam nuclei, but not in a different channel? One can fairly assume that the same reaction products could be registered in such reactions as ^{2}H(^{8}He,^{5}He)^{5}H or ^{2}H(^{8}He,^{7}He)^{3}H. In this chapter, we provide the results of these channels investigation and

the correlations of the latter with the low-energy part of the ^{6}H missing mass spectrum.

9.5.1 d-^{7}He background channel

Let us consider, that the registered ^{4}He and ^{3}H nuclei were actually the products of the ^{2}H(^{8}He,^{7}He)^{3}H reaction. In this case, ^{7}He can be reconstructed as a missing component from the registered ^{3}H in the central telescope. The ^{7}He missing mass spectrum, reconstructed from the tritons in coincidence with alpha, registered in one of the side silicon telescopes is presented in Fig. 45 b). We have selected the ^{7}He low-energy part, see the green colored part, and analyzed the position of such events in the ^{6}H spectrum, see the green-line Fig. 45 a). The blue-line distributions relate to the inverse procedure and correspond to the events of the low-energy ^{6}H spectrum. The result of low energy spectra correlation analysis is that the low-energy events of ^{7}He are spread at the high-energy region of ^{6}H and do not form any pronounced peak. Thus, we conclude that our ^{6}H spectrum is very weakly affected by possible population of ^{7}He, produced in the d-^{7}He reaction.
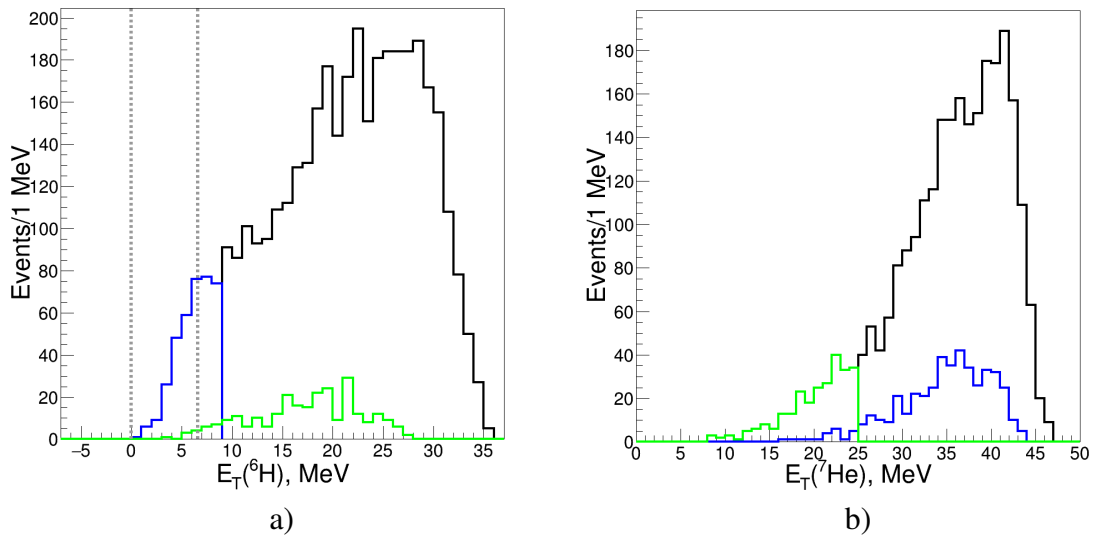
Figure 45: a) The ^{6}H missing mass spectra. b) The ^{7}He missing mass spectra. In both Figures: the low-energy part with $E_T(^6\text{H})<9$ MeV is colored in blue; the green-line spectra correspond to the events of low excitation energies of ^{7}He: $E_T(^7\text{He})<25$ MeV.

9.5.2 d-^{5}He background channel

This channel leads to the production of target-like ^{5}He and beam-like ^{5}H. The latter moves at forward angles and decays into t+2n, which does not allow to measure it directly. However, the recoil ^{5}He of smaller energies also lives not enough time to reach the silicon telescopes. That is why, the ^{2}H(^{8}He,^{5}He)^{5}H reaction can be studied only for triple ^{4}He-^{3}H-n coincidence events. For those, the recoil ^{5}He invariant mass is reconstructed from the measured alpha and neutron. The correlation of this spectrum with the ^{6}H, obtained for triple coincidence events is presented in Fig. 46.
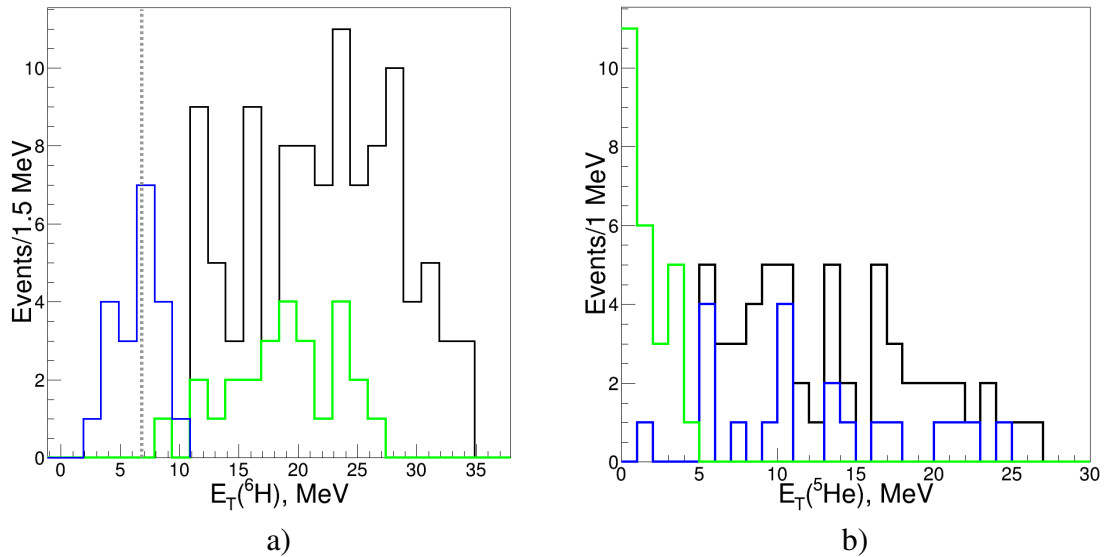
Figure 46: a) The ^{6}H missing mass spectra, reconstructed the recoil ^{4}He in triple ^{4}He-^{3}H-n coincidence events. b) The ^{5}He missing mass spectra, reconstructed from ^{5}H. In both Figures: the low-energy part with $E_T(^6$H$)<9$ MeV is colored in blue; the green line corresponds to the events of low excitation energies of ^{5}He: $E_T(^5$He$)<5$ MeV.

Thus, the conducted background reaction channel tests did not confirm the idea of a background nature of the low-energy structure of ^{6}H. This gives more confidence to the correct reaction channel identification and in conjunction with the previous chapters allows us to declare the observation of the ^{6}H resonance behavior.

9.6 ^{6}H spectrum interpretation

The suggested interpretations of the low-energy ^{6}H spectrum are illustrated in Fig. 47. In this figure the empty-target-corrected ^{4}He-^{3}H coincidence spectrum of Fig. 43 (a,b) and the ^{4}He-^{3}H-n coincidence spectrum of Fig. 44 (c,d) are also corrected for the experimental efficiency by a Monte-Carlo procedure. For consistency, the neutron coincidence spectrum in Fig. 47 (c,d) has the same $\theta_{\text{c.m.}} < 16°$ cutoff.

Obviously, non of the shown spectra can be interpreted as a pure phase volume, see the orange curves in Fig. 44 d). That is why, in order to explain the obtained missing mass spectra, especially at low-energy part of $E_T \sim 3 - 8$ MeV, some resonant contributions are also needed. The described spectrum analysis resulted in conclusion, that the suggestions of the resonance, located at the energies higher than 6.8 MeV are not acceptable, because those lead to the systematic underestimation of the low-energy data. Thus, the $E_T = 6.8$ MeV resonance energy can be regarded as an upper limit for the ^{6}H resonance energy.

For the spectrum interpretation we used the conventional Lorentz-like profiles, given as:

$$\frac{d\sigma}{dE_T} \sim \frac{\Gamma(E_T)}{(E_r - E_T)^2 + \Gamma(E_T)^2/4}$$

Important feature of our data is the nonobservation of the ^{6}H ground state at $E_T = 2.6 -$

a) Triton kinematical triangle

b) Neutron kinematical triangle

c) Reaction angle correlation

d) Triple coincidence spectrum
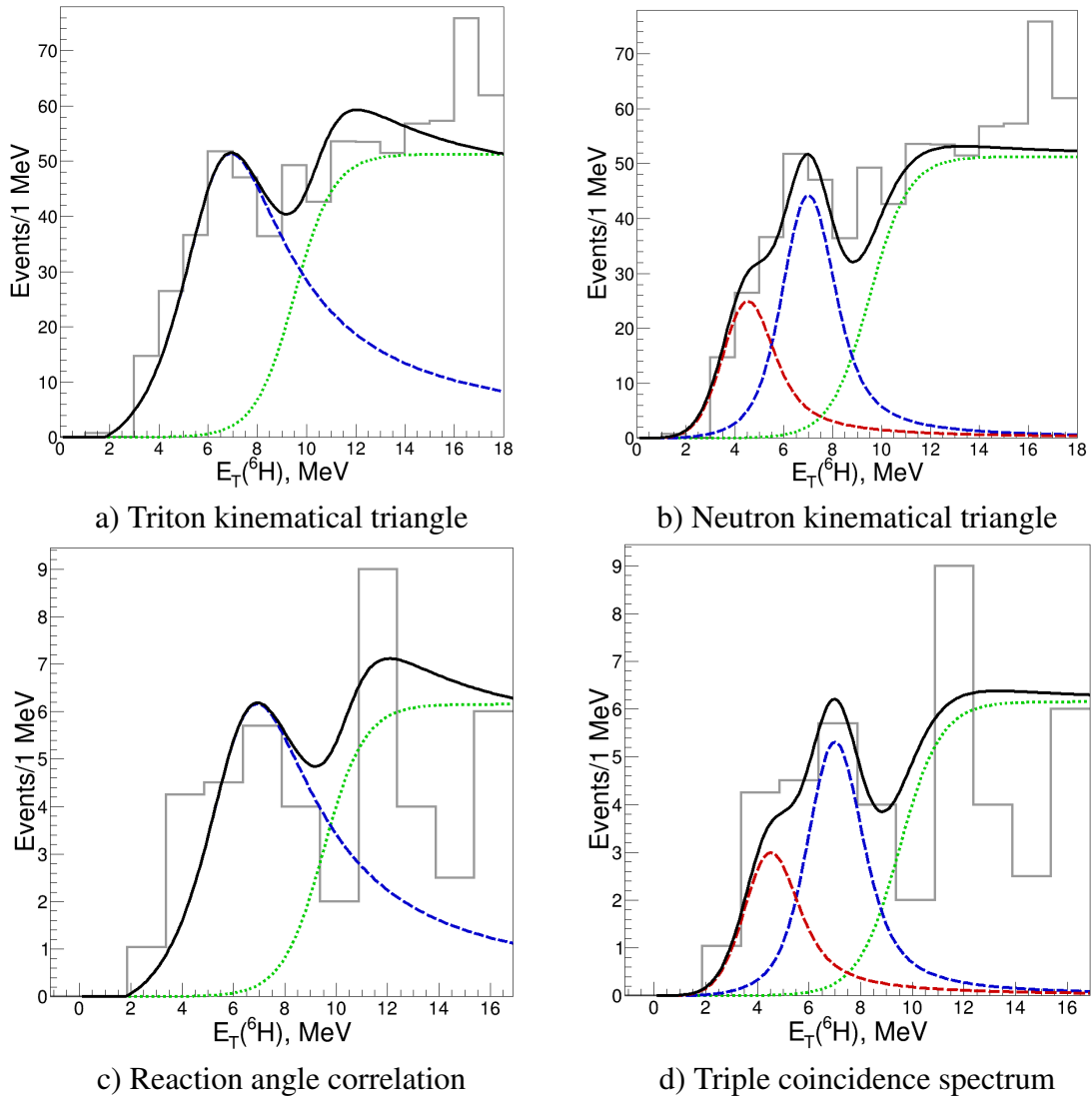
Figure 47: Two suggested interpretations of the ^{6}H spectrum with one broad (left figures) or two relatively narrow states (right figures). The gray histograms in a) and b) show the efficiency-corrected ^{4}He-^{3}H coincidence data based on Fig. 43 b). The bottom c) and d) histograms show represents similar data of triple ^{4}He-^{3}H-n coincidence events, based on Fig. 44 d). The red dashed and blue dotted curves correspond to the possible contributions of the low-energy ^{6}H states, the green curves are an option for the physical background approximated by the Fermi-type profile.

2.9 MeV, as it was proposed in the earlier works [46, 47, 43]. To quantify this conclusion we performed complete Monte-Carlo simulations for the isolated ground state assuming the $E_T = 2.6$ MeV resonance energy and angular distribution predicted by calculations of Fig. 40. The Monte-Carlo simulations of our setup efficiency, see Fig. 39 d), show that this energy and angular range $\theta_{c.m.} < 16°$ are most favorable for such a resonant state identification. However, according to the advanced subtraction procedure the obtained spectrum population is practically zero at $E_T < 3.5$ MeV, see Fig. 43 b). This led to the task of the lower limit for the resonance state admissible by our data. We imply that the population rate for such a state should be comparable for several possible low-lying states of ^{6}H populated by the $\Delta l = 1$ angular momentum transfer. The mentioned above reason of systematic disagreement of the suggested interpreta-

tion with the experimental data at low energies does not allow one to describe the spectrum in the region $E_T \sim 3 - 5$ MeV even for a quite broad state with $\Gamma = 3$ MeV, especially notice-able for the triple coincidence data in c) panel of Fig. 44. That is why, for the $E_T = 6.8$ MeV resonance of a smaller width (e.g. $\Gamma = 1.5$ MeV) the interpretation with two states is more preferable, see the blue and red profiles in Fig. 47 (b,d). In the assumption of several states, the illustrated $E_T = 4.5$ MeV peak is the lowest ^{6}H resonant state energy, which can be consistent with our data. However, one should keep in mind that more than two overlapping ^{6}H states may actually be expected in this energy range. That is why, the obtained spectra do not exclude the many states.
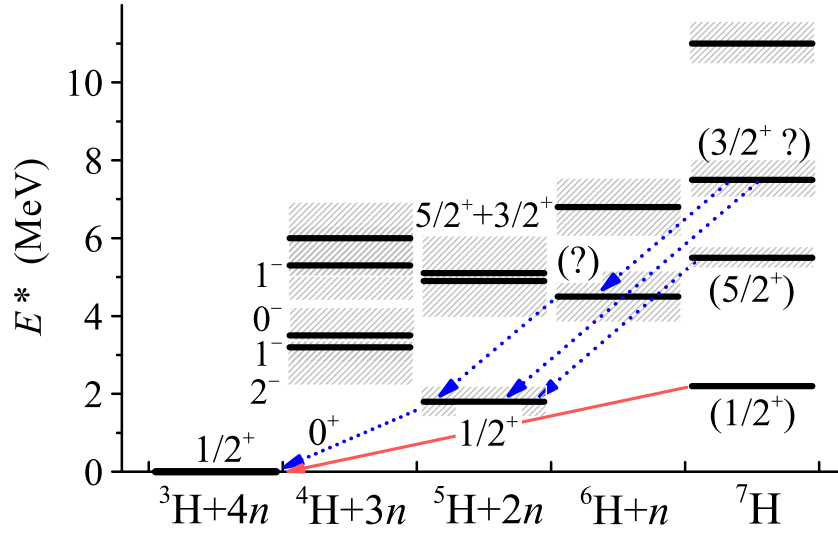
Figure 48: The level schemes of ^{6}H, and the known neighboring ^{4}H, ^{5}H [35, 98, 94], and ^{7}H [91, 92] systems, which are important for the discussions of this work. The solid red arrow illustrates the decay mechanism of the ground state of ^{7}H which is expected to be the "true" $4n$ emission. The dotted blue arrows illustrate the decay mechanism of the higher excitations in ^{7}H, which is expected to be the sequential $2n+2n$ and $2n+n+n$ emissions via the ^{5}H and ^{6}H excited states, respectively.

These obtained results on the ^{7}H and ^{6}H energy spectra also an evidence about the 5-body decay mechanism of the observed ^{7}H ground state at 2.2 MeV above the ^{3}H+4n threshold. Such conclusion comes from the hydrogen isotope energy level diagrams, presented in Fig. 48. It is clearly seen, that since the low-energy limit of the possible ^{6}H resonance is located at $E_T = 4.5$ MeV, the ^{7}H ground state decays directly into the t+4n.

As in the case of the ^{7}H data analysis, the analysis of the fragment energy distributions of ^{6}H provides unique information about its structure and properties of its subsystems. In particular, the analysis of the sequential decay ^{6}H$\rightarrow^5$H(g.s.)+n$\rightarrow^3$H+3n showed that the energy distribu-tion of the emitted ^{3}H demonstrates strong sensitivity to the correlations in the ^{5}H intermediate system. The calculations, described in details in Ref. [97], have been performed in assumption of the ^{6}H decay energy situated in a range between from 3.5 to 7.5 MeV, which corresponds to the observed resonance at 6.8 MeV. Two models were used for theoretical estimations: the uncorrelated decay, described with a phase volume model and the highly correlated dineutron

decay of the ^{5}H ground state. The obtained estimations were compared to the results of our experiment and the data of the ^{5}H work [94]. These resulting datasets are provided in Table 3 and led to the conclusion that the preferable interpretation of the data suggests the extremely correlated emission of two neutrons from the ^{5}H ground state intermediate system.

Table 3: Mean values of the $3E_{^3H}/2E_{^5H}$ distributions. The "th." columns show the theoretical results and the "bias" columns give the corresponding values corrected for the experimental bias via the Monte-Carlo procedure, see Ref. [97]. The "4-body p.v." is the four-body phase volume approximation of the true $3n$ emission from ^{6}H. Models for the sequential ^{6}H$\rightarrow$ ^{5}H(g.s.)$+n \rightarrow$ ^{3}H$+3n$ decay: "3-body p.v." — the uncorrelated three-body phase volume decay of the ^{5}H ground state, "realistic" — the experimental data of work [94], "dineutron" — the highly correlated dineutron decay of the ^{5}H ground state. The column "experiment" shows the obtained experimental data.

| Models: | 4-body p.v. | | 3-body p.v. | | realistic | | dineutron | | experiment | |
ranges (MeV)	th.	bias	th.	bias	th.	bias	th.	bias	^{4}He-^{3}H	^{4}He-^{3}H-n
$3.5 < E_T < 5.5$	1/3	0.30	0.29	0.28	0.33	0.30	0.43	0.39	0.42(3)	0.49(7)
$5.5 < E_T < 7.5$	1/3	0.28	0.27	0.24	0.31	0.26	0.39	0.33	0.33(2)	0.24(8)

As for the estimations of the cross section, one may find in Fig. 47 (a,c) that for the ^{6}H missing mass spectrum in the $E_T = 4-8$ MeV energy range up to $\sim 35\%$ of the population cross section can be related to background, corresponding to the tail of the higher energy excitations. For that reason the lower limit given for the uncertainty of the population cross section should be extended as $d\sigma/d\Omega_{\text{c.m.}} \simeq 190^{+40}_{-80}$ μb/sr.

9.7 ^{6}H summary

The data of this work obtained in the double ^{4}He-^{3}H coincidences have quite large statistics (among available data only for the ^{9}Be$(\pi^-,pd)^6$H reaction [40] statistics is better), and it allows for a good missing mass energy resolution for the ^{6}H spectrum and careful treatment of the backgrounds. The consistently reconstructed spectrum picture was obtained in the triple ^{4}He-^{3}H-n coincidence data, which provides much smaller statistical confidence but can be seen as practically background free. Such data quality was achieved using the kinematical triangle method, applied for both detected neutron and triton. Both statistical analysis and correlation analysis of all possible satellite reaction channels confirmed the resonance nature of the low-energy spectrum of ^{6}H. Thus, the derived from our data detailed information on the spectrum of ^{6}H for $E_T < 9$ MeV shed the light on the problems of ^{6}H structure, 5-body decay of ^{7}H and 3-body decay properties of ^{7}H.

The reconstructed from the ^{4}He data missing mass spectrum of ^{6}H has a broad bump at $E_T = 4-8$ MeV, which is populated with a cross section $d\sigma/d\Omega_{\text{c.m.}} \simeq 190^{+40}_{-80}$ μb/sr in the $5° < \theta_{\text{c.m.}} < 16°$ angular range. This is a reasonably large cross section, consistent with the resonant population mechanism. This bump can be interpreted as a broad ($\Gamma > 5$ MeV) resonant state at $E_T = 6.8$ MeV. Observation of such a states(s) is consistent with the data of Ref. [40], concerning the lowest ^{6}H state.

We have found no evidence of the $\approx 2.6 - 2.9\,\text{MeV}$ state in ^{6}H, which was reported in the pioneering work [46] and has got support in [47, 43]. The cross section limit $d\sigma/d\Omega_{\text{c.m.}} \lesssim 5$ μb/sr is set for the population of possible states with $E_T < 3.5\,\text{MeV}$. Also the existence of the ^{6}H ground state at $\approx 2.6 - 2.9\,\text{MeV}$ is hardly consistent, due to the pairing energy argument, with our observation of the ground stat of ^{7}H at $2.2(5)\,\text{MeV}$. There is no sensible structural argument explaining why the population of the possible $\approx 2.6 - 2.9$ MeV ground state could be suppressed in a very "simplistic" ^{2}H(^{8}He, ^{4}He)^{6}H transfer reaction and not observed in our data, while the ^{6}H spectrum at $E_T \gtrsim 3.5\,\text{MeV}$ is well populated. Therefore, we suggest that the position of the ^{6}H ground state is not yet established, and discussion of this issue should be continued.

The broad bump in the ^{6}H spectrum at $E_T = 4 - 8\,\text{MeV}$ can also be interpreted as overlap of several relatively narrow states. We suggest to resolve it into two overlapping states, at $E_T =$ 4.5 and 6.8 MeV of $\Gamma = 1.5\,\text{MeV}$ width. These states correspond to the lowest possible ^{6}H ground state energy admissible by our data. According to the energy systematics and the paring energy arguments, resonance with such an energy is a good candidate for the ^{6}H ground state.

The updated level scheme of all heavy hydrogen isotopes, illustrated in Fig. 48, clearly demonstrates the evidence of the true 5-body decay of ^{7}H in its ground state. Obviously, that the low-energy limit of the lowest ^{6}H resonance position, established as $E_T = 4.5\,\text{MeV}$, confirms that the ^{7}H ground state, observed at $E_T = 2.2\,\text{MeV}$, decays via the "true" (or simultaneous) $4n$ emission. Thus, ^{7}H is the first confirmed case of nucleus possessing this exclusive few-body dynamics of decay.

The momentum distribution of the ^{3}H decay fragments was reconstructed in the ^{6}H rest frame. The theoretical studies, described in work [97], of the four-body sequential ^{6}H$\rightarrow$ ^{5}H(g.s.)+$n \rightarrow$ ^{3}H+$3n$ decays were performed for the first time and provided unique results on the ^{5}H decay. Within the assumption of the ^{6}H sequential decay we have found that our data provide evidence that an extremely strong "dineutron-type" correlation is realized in the decay of the ^{5}H ground state.

Although in the frame of this work we do not establish the positions of the ^{6}H resonance states, but the demonstrated results and developed experimental methodics present the significant step towards resolving the ^{6}H problem, which can be applied for extracting information about the multi-particle nuclear decay dynamics. Never the less, in order to fulfill these tasks, more accurate measurements are needed for more solid conclusions.

10 Theoretical model

In this chapter we introduce the developed theoretical model allowed to perform the cross-section analysis of the ^{2}H(^{8}He,^{3}He)^{7}H(g.s.) reaction. As we have suggested the reason for the observed extremely low cross section value and the position of the first diffraction minimum at unexpectedly low angles is the extremely peripheral character of the ^{2}H(^{8}He,^{3}He)^{7}H(g.s.) reaction. The FRESCO calculation with the standard parameters showed provided the cross-section with a typical value of few millibarns at the zero angles, see the red solid curve in Fig. 38 a). But the deduced cross-section of ≈ 25 μb/sr for $\theta_{cm} \sim 5° - 9°$) indicated the uniqueness of the ^{7}H case and the inapplicability of the standard methods of the reaction theory.

In theoretical calculations accompanying the data we limited ourselves to very simple reaction mechanism populating ^{7}H: we considered sudden removal approximation for proton from the ^{8}He core to populate ^{7}H spectrum. Such process can be understood based on the plane-wave Born approximation model, which well reflects the "quasifree scattering" aspect of the process. Our goal is to describe the obtained in the experiment (Fig. 38 a)) distribution with the developed parametrization of the peripheral reaction behavior.

The sudden removal reaction mechanism corresponds to a situation where in the initial state we take into account only the potential between the transferring proton (further referred as participant) and ^{7}H (further referred as spectator), and in the final state we neglect all the interactions except the target-participant one. Thus, we assume that the interaction time is so short that it does not affect the spectator at all [99]. This approximation allows to factorize the cross section into product of the elastic cross section (on-shell T-matrix squared) and formfactor (squared). In this chapter we apply the mentioned formalism for the ^{2}H(^{8}He,^{3}He)^{7}H(g.s.) reaction.

10.1 Model

Let us use the following notations for the ^{2}H(^{8}He,^{3}He)^{7}H(g.s.) reaction:

- $\mathbf{K}_{in}$ is the momentum of the ^{8}He incoming beam in the laboratory frame of reference.

- $\mathbf{K}_{out} = \{\mathbf{K}'_{\parallel}, \mathbf{K}'_{\perp}\}$ is the laboratory momentum of the spectator ^{7}H. It is decomposed into longitudinal momentum $\mathbf{K}'_{\parallel}$ and transversal momentum $\mathbf{K}'_{\perp}$ (Z axis as parallel to the beam direction).

- $\mathbf{K}_{rec} = \mathbf{K}_{in} - \mathbf{K}_{out}$ is the laboratory momentum of the center of mass of the recoil ^{3}He.

- $\mathbf{K}_{spf} = \frac{M_s}{M_s + M_p}\mathbf{K}_{in}$ is the "spectator in projectile frame" momentum, i.e. the spectator momentum as a component of the initial ^{8}He projectile.

- $\mathbf{K} = \frac{M_t}{M_b + M_t}\mathbf{K}_{in}$ is the relative momentum in the incoming channel (beam-target). According to the definition of the conjugated radial variable, it is defined in such a way that this is the beam momentum in the center-of-mass frame of the whole system (beam+target), see Fig. 49.

- $\mathbf{K}' = \frac{M_s}{M_b + M_t}\mathbf{K}_{\text{in}} - \mathbf{K}_{\text{out}}$ is the relative momentum in the outgoing channel (spectator-recoil), accordingly, ^{7}He momentum in the center-of-mass frame of the outgoing system (spectator+recoil), see Fig. 49.

For reaction with 26.5 A MeV incoming ^{8}He beam

$$\mathbf{K}_{\text{in}} = 1785.15 \text{ MeV}, \qquad \mathbf{K}_{\text{spf}} = 1561.98 \text{ MeV}, \qquad \mathbf{K} = 357.79 \text{ MeV}. \tag{7}$$

The masses of the reaction components are:

- Beam: $M_b = M(^8\text{He}) = 7482.538$ MeV

- Target: $M_t = M(^2\text{H}) = 1875.612$ MeV

- Participant: $M_p = M(\text{proton}) = 938.272$ MeV

- Spectator: $M_s = M(^7\text{H}) = 6567.18$ MeV

- Recoil or "QFS subsystem": $M_r = M(^3\text{He}) = 2808.391$ MeV

- Reaction Q-value: $Q = (M_b + M_t) - (M_s + M_r) = -17.421$ MeV
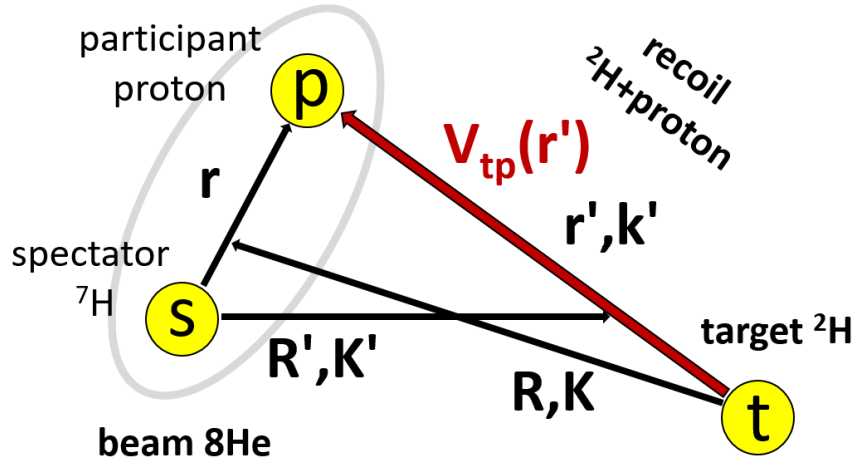
Figure 49: Scheme of the ^{2}H(^{8}He,^{3}He)^{7}H reaction in the quasi-free scattering approximation. Red arrow represents the target-participant potential the only one taking into account in the outgoing system.

The energy balance for incoming and outgoing channels is

$$M_b + \frac{K_{\text{in}}^2}{2M_b} + M_t = M_s + \frac{K_{\text{out}}^2}{2M_s} + M_r + \frac{K_{\text{rec}}^2}{2M_r} + E_T, \tag{8}$$

where E_T is the energy of ^{7}H above the ^{3}H+4n decay threshold.

From momentum conservation

$$\mathbf{K}_{\text{in}} = \mathbf{K}_{\text{out}} + \mathbf{K}_{\text{rec}}, \tag{9}$$

we define the total excitation energy available for spectator E_T and recoil system E_{rec}^* for the certain point in the kinematical plane $\{K'_{||}, K'_{\perp}\}$:

$$E_{\text{bal}}(K'_{||}, K'_{\perp}) \equiv E_T = \frac{K_{\text{in}}^2}{2M_b} + Q - \frac{K'^2_{||} + K'^2_{\perp}}{2M_s} - \frac{(K_{\text{in}} - K'_{||})^2 + K'^2_{\perp}}{2M_r}. \tag{10}$$

The energy balance function $E_{\text{bal}}(K'_{||}, K'_{\perp})$ is given in Fig. 50. For clarity, the experimental data is also presented.
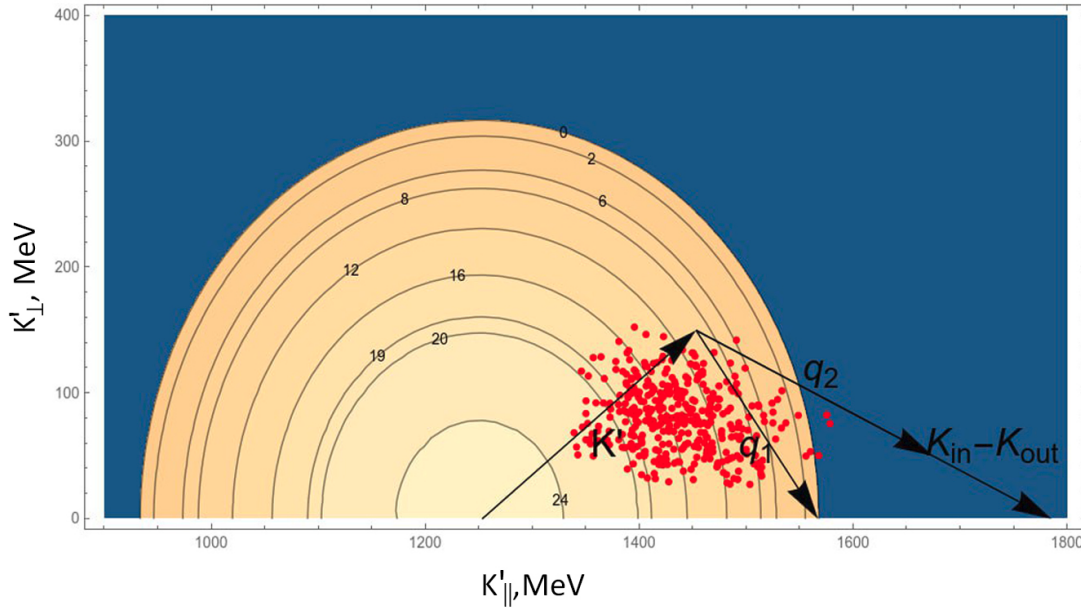
Figure 50: Kinematical locus and energy balance of the ^{2}H(^{8}He,^{3}He)^{7}H(g.s.) reaction. The red color dots correspond to the data of the second experimental run discussed in Section 8. Vertical and horizontal axes correspond respectively to the longitudinal and transversal momenta of the spectator ^{7}H.

We consider the system of three particles, "spectator" s (^{7}H inside the ^{8}He beam projectile), participant p (proton inside ^{8}He), and "target" t (^{2}H). Let us denote $\mathbf{r}$ the internal coordinate of ^{8}He, the vector directed from spectator fragment to the participant, and $\mathbf{R}$ is vector pointing from ^{2}H target to the center-of-mass of the beam. In the exit channel the applied approximation requires another Jacobi set of variables — $\mathbf{r}'$ and $\mathbf{R}'$, see Fig. 49. The vector $\mathbf{r}'$ is the internal coordinate of the final state spectator, and $\mathbf{R}'$ is the vector directed from the spectator to the center-of-mass of the recoil ^{3}He.

There is a linear transformation from the initial state $\{\mathbf{R}, \mathbf{r}\}$ to the final state $\{\mathbf{R}', \mathbf{r}'\}$ coordinate sets:

$$\mathbf{r}' = \mathbf{R} + \frac{M_s}{M_s + M_p}\mathbf{r} = \mathbf{R} + \alpha\mathbf{r} \tag{11}$$

$$\mathbf{R}' = -\frac{M_t}{M_t + M_p}\mathbf{R} + \frac{M_p(M_t + M_p + M_s)}{(M_s + M_p)(M_t + M_p)}\mathbf{r} = -\beta\mathbf{R} + \gamma\mathbf{r}$$

We use the model with two major related physical assumptions — quasifree and plane wave

73

in the in- and out-channels:

> • Quasifree assumption: only one potential is taken into account in the T-matrix
> — the potential between target and participant fragment.
>
> • Plane wave assumption: plane wave motion is assumed in the initial state coor-
> dinate and conjugated momenum $\{\mathbf{R}, \mathbf{K}\}$ and final state coordinate and conju-
> gated momenum $\{\mathbf{R}', \mathbf{K}'\}$. This approximation makes the explicit factorization
> of the cross section possible and makes consequent derivations purely analyti-
> cal.

The transition amplitude in the T-matrix formalism and within the frame of the quasi-free assumption has the form:

$$T_{fi}(\mathbf{K}', \mathbf{k}', \mathbf{K}) = \int d^3 r \, d^3 R \, \Psi_{tp}^*(\mathbf{k}', \mathbf{r}') \Psi_{s(tp)}^*(\mathbf{K}', \mathbf{R}') V_{tp}(\mathbf{r}') \Psi_{sp}(\mathbf{r}) \Psi_{t(sp)}(\mathbf{K}, \mathbf{R}), \qquad (12)$$

where $V_{tp}(\mathbf{r}')$ is the target-participant interaction potential, see Fig. 49.

In the plane wave approximation we use

$$\Psi_{t(sp)}(\mathbf{K}, \mathbf{R}) = e^{i\mathbf{K}\mathbf{R}} \quad , \quad \Psi_{s(tp)}^*(\mathbf{K}', \mathbf{R}') = e^{-i\mathbf{K}'\mathbf{R}'}. \qquad (13)$$

Inserting the unity operator in the form

$$\hat{1} = \int \frac{d^3 k}{(2\pi)^3} \int d^3 r'' e^{i\mathbf{k}(\mathbf{r}'' - \mathbf{r}')}, \qquad (14)$$

we can effectively split the "prime" and "initial" variables in Equation (12)

$$T_{fi}(\mathbf{K}', \mathbf{k}', \mathbf{K}) = \int \frac{d^3 k}{(2\pi)^3} \int d^3 r'' \, \psi_{tp}^*(\mathbf{k}', \mathbf{r}'') V_{tp}(\mathbf{r}'') e^{i\mathbf{k}\mathbf{r}''} \int d^3 r \, d^3 R \, e^{-i\mathbf{k}\mathbf{r}'} e^{-i\mathbf{K}'\mathbf{R}'} \Psi_{sp}(\mathbf{r}) e^{i\mathbf{K}\mathbf{R}}, \qquad (15)$$

$$\mathbf{K}\mathbf{R} - \mathbf{k}\mathbf{r}' - \mathbf{K}'\mathbf{R}' = \mathbf{R}(\mathbf{K} - \mathbf{k} + \beta\mathbf{K}') - \mathbf{r}(\alpha\mathbf{k} + \gamma\mathbf{K}'),$$

and using the definition of the T-matrix for the quasi-free channel

$$T_{\text{QFS}}(\mathbf{k}, \mathbf{k}') = \int d^3 r \, e^{-i\mathbf{k}\mathbf{r}} V_{tp}(\mathbf{r}) \, \psi_{tp}(\mathbf{k}', \mathbf{r}), \qquad [\text{fm}^3 \text{ MeV}] \qquad (16)$$

we get expression for the T-matrix:

$$T_{fi}(\mathbf{K}', \mathbf{k}', \mathbf{K}) = \int \frac{d^3 k}{(2\pi)^3} T_{\text{QFS}}^\dagger(\mathbf{k}', \mathbf{k}) \int d^3 R \, e^{i(\mathbf{K} - \mathbf{k} + \beta\mathbf{K}')\mathbf{R}} \int d^3 r \, e^{-i(\alpha\mathbf{k} + \gamma\mathbf{K}')\mathbf{r}} \Psi_{sp}(\mathbf{r}). \qquad (17)$$

The momentum formfactor for the initial state spectator-participant relative motion wave function is

$$\Phi_{sp}(\mathbf{q}) = \int d^3 r \, e^{-i\mathbf{q}\mathbf{r}} \Psi_{sp}(\mathbf{r}) \qquad [\text{fm}^{3/2}] \qquad (18)$$

For the plane wave assumption we get:

$$T_{fi}(\mathbf{K}',\mathbf{k}',\mathbf{K}) = \int \frac{d^3k}{(2\pi)^3} \, T_{\mathrm{QFS}}^{\dagger}(\mathbf{k}',\mathbf{k}) \, (2\pi)^3 \, \delta(\mathbf{K}-\mathbf{k}+\beta\mathbf{K}') \, \Phi_{sp}(\alpha\mathbf{k}+\gamma\mathbf{K}') \,. \tag{19}$$

$$[\mathrm{fm}^3] \, [\mathrm{MeV}] \, [\mathrm{fm}^{3/2}] = [\mathrm{fm}^{9/2} \, \mathrm{MeV}]$$

After intermediate momentum integration

$$T_{fi}(\mathbf{K}',\mathbf{k}',\mathbf{K}) = T_{\mathrm{QFS}}^{\dagger}(\mathbf{k}',\mathbf{K}+\beta\mathbf{K}') \, \Phi_{sp}\left(\alpha\mathbf{K}+(\alpha\beta+\gamma)\mathbf{K}'\right) \,, \tag{20}$$

where there is very simple relation

$$\alpha\beta + \gamma \equiv 1 \,.$$

We can see that there are two very special "transferred momenta" in the model, which are illustrated in Fig. 50.

$$\begin{aligned}
\mathbf{q}_1 &= \alpha\mathbf{K}+\mathbf{K}' = \frac{M_s}{M_s+M_p}\mathbf{K}_{\mathrm{in}} - \mathbf{K}_{\mathrm{out}} = \mathbf{K}_{\mathrm{spf}} - \mathbf{K}_{\mathrm{out}} \,, \\
\mathbf{q}_2 &= \mathbf{K}+\beta\mathbf{K}' = \frac{M_t}{M_t+M_p}(\mathbf{K}_{\mathrm{in}} - \mathbf{K}_{\mathrm{out}}) = \frac{M_t}{M_t+M_p}\mathbf{K}_{\mathrm{rec}} \,.
\end{aligned} \tag{21}$$

Specifically for the ^{2}H(^{8}He,^{3}He) transfer reaction the transferred momenta can be expressed as

$$\begin{aligned}
\mathbf{q}_1 &= \mathbf{K}+\mathbf{K}' = \frac{7}{8}\mathbf{K}_{\mathrm{in}} - \mathbf{K}_{\mathrm{out}} = \mathbf{K}_{\mathrm{spf}} - \mathbf{K}_{\mathrm{out}} \,, \\
\mathbf{q}_2 &= \mathbf{K}+\frac{2}{3}\mathbf{K}' = \frac{2}{3}(\mathbf{K}_{\mathrm{in}} - \mathbf{K}_{\mathrm{out}}) = \frac{2}{3}\mathbf{K}_{\mathrm{rec}} \,.
\end{aligned} \tag{22}$$

Final expression for the T-matrix in explicitely factorized form is

$$T_{fi}(\mathbf{K}',\mathbf{k}',\mathbf{K}) = T_{fi}(\mathbf{K}_{\mathrm{out}},\mathbf{k}',\mathbf{K}_{\mathrm{in}}) = T_{\mathrm{QFS}}^{\dagger}(\mathbf{k}',\mathbf{q}_2) \, \Phi_{sp}(\mathbf{q}_1) \,. \tag{23}$$

The "universal" expression for cross section is

$$d\sigma = \frac{1}{v} \, \left|T(\mathbf{k_1}'...\mathbf{k_n}',\mathbf{k})\right|^2 \, d\rho_f \,, \tag{24}$$

where the density of the continuum final states is defined by the universal recipy:

$$d\rho_f = (2\pi) \, \delta(E_1'+...+E_n'-E) \prod_{i=1}^{n} \frac{d^3k_i'}{(2\pi)^3} \,. \tag{25}$$

where $n = N-1$ is number of "dynamical" Jacobi momenta in the final state, which is by 1 smaller then the number of particles N in the final state.

Specifically for elastic scattering case we gets

$$\frac{d\sigma^{(\text{el})}}{d\Omega_{k'}} = \frac{1}{v}\int |T(\mathbf{k}',\mathbf{k})|^2 (2\pi)\,\delta(E'-E)\,\frac{k'^2\,dk'}{(2\pi)^3} = \frac{M^2}{(2\pi)^2}\,|T(\mathbf{k}',\mathbf{k})|^2 \equiv |f(\mathbf{k}',\mathbf{k})|^2 , \quad (26)$$

where M denotes the reduced mass of the system; $|\mathbf{k}'| \equiv |\mathbf{k}|$. This equation also provides connection between $2 \to 2$ scattering T-matrix and elastic scattering amplitude $f(\mathbf{k}',\mathbf{k})$.

For inelastic excitation of the final state $|\mathbf{k}'| \neq |\mathbf{k}|$ one gets the expression

$$\frac{d\sigma^{(\text{inel})}}{d\Omega_{k'}} = \frac{M^2}{(2\pi)^2}\,\frac{k'}{k}\,|T(\mathbf{k}',\mathbf{k})|^2 . \quad (27)$$

For transfer reactions the in- and out-channel masses are also not equal and one gets the expression

$$\frac{d\sigma^{(\text{trans})}}{d\Omega_{k'}} = \frac{M_{\text{in}} M_{\text{out}}}{(2\pi)^2}\,\frac{k'}{k}\,|T(\mathbf{k}',\mathbf{k})|^2 . \quad (28)$$

The transfer reaction T-matrix, squared and summed over all magnetic quantum numbers

$$\sum_{m_{j_r}\mu_s M_i\mu_t} |T_{fi,j_r m_{j_r}\mu_s,J_i M_i\mu_t}|^2 = (4\pi)^3 \sum_{m_{j_r}\mu_s M_i\mu_t} |T_{j_r l_r s_r}(E'_r,q_2)|^2\,|\phi_{sp,0}(q_1)|^2 \times$$

$$\times \sum_{m\mu_p\mu_r}\sum_{\tilde{m}\tilde{\mu}_p\tilde{\mu}_r} C^{J_i M_i}_{s_s\mu_s s_p\mu_p} C^{j_r m_{j_r}}_{l_r m s_r\mu_r} C^{s_r\mu_r}_{s_t\mu_t s_p\mu_p} C^{J_i M_i}_{s_s\mu_s s_p\tilde{\mu}_p} C^{j_r m_{j_r}}_{l_r\tilde{m}s_r\mu_r} C^{s_r\tilde{\mu}_r}_{s_t\mu_t s_p\tilde{\mu}_p} Y^*_{lm}(\hat{q}_2) Y_{l\tilde{m}}(\hat{q}_2) = \quad \to \quad (29)$$

where we used the notations: J(j) - total angular momentum; l - orbital angular momentum; s - spin; m - projection of the angular momentum; μ_j - projection of the total angular momentum; μ - projection of the spin; indexes i,t,s,p correspond to ^{8}He, ^{2}H, ^{7}H and proton respectively.

By using

$$\sum_{M_i\mu_s} C^{J_i M_i}_{s_s\mu_s s_p\tilde{\mu}_p} C^{J_i M_i}_{s_s\mu_s s_p\mu_p} = \frac{2J_i+1}{2s_p+1}\,\delta_{\tilde{\mu}_p\mu_p} , \qquad \sum_{\mu_t\mu_p} C^{s_r\mu_r}_{s_t\mu_t s_p\mu_p} C^{s_r\tilde{\mu}_r}_{s_t\mu_t s_p\mu_p} = \delta_{\tilde{\mu}_r\mu_r} ,$$

one gets

$$\to \quad = (4\pi)^3 \frac{2J_i+1}{2s_p+1} |T_{j_r l_r s_r}(E'_r,q_2)|^2\,|\phi_{sp,0}(q_1)|^2 \sum_{m_{j_r}}\sum_{m\tilde{m}\mu_r} C^{j_r m_{j_r}}_{l_r m s_r\mu_r} C^{j_r m_{j_r}}_{l_r\tilde{m}s_r\mu_r} Y^*_{lm}(\hat{q}_2) Y_{l\tilde{m}}(\hat{q}_2) = \quad \to$$

by using

$$\sum_{m_{j_r}\mu_r} C^{j_r m_{j_r}}_{l_r m s_r\mu_r} C^{j_r m_{j_r}}_{l_r\tilde{m}s_r\mu_r} = \frac{2j_r+1}{2l+1}\,\delta_{\tilde{m}m} , \qquad \sum_m Y^*_{lm}(\hat{q}_2) Y_{lm}(\hat{q}_2) = \frac{2l+1}{4\pi} ,$$

one gets the T-matrix averaged over initial magnetic quantum number

$$\frac{1}{(2J_i+1)(2s_t+1)} \sum_{m_{j_r}\mu_s M_i\mu_t} |T_{fi,j_r m_{j_r}\mu_s,J_i M_i\mu_t}|^2 = \frac{(4\pi)^2(2j_r+1)}{(2s_p+1)(2s_t+1)} |T_{j_r l_r s_r}(E'_r,q_2)\,\phi_{sp,0}(q_1)|^2 . (30)$$

So, we get the transfer cross section as

$$\frac{d\sigma}{d\Omega_{\text{cm}}} = 4 M_{s(tp)} M_{bt} \frac{K'}{K} \frac{(2j_r+1)}{(2s_p+1)(2s_t+1)} \left| \phi_{sp,0}(q_1) \, T_{j_r l_r s_r}(E'_r, q_2) \right|^2 . \tag{31}$$

The angular dependence in the frame of reference attached to the center of mass of the system is realized via the dependencies of the transferred momenta $\mathbf{q}_1$ and $\mathbf{q}_2$. Using Equation (21) the transferred momenta can be easily constructed as the function of E_T and θ_{cm}

$$
\begin{aligned}
q_1 &= \sqrt{(K' \sin \theta_{\text{cm}})^2 + \left(K' \cos \theta_{\text{cm}} - \frac{M_s}{M_b} K \right)^2} \quad \text{and} \\
q_2 &= \sqrt{\left(\frac{M_t}{M_t + M_p} K' \sin \theta_{\text{cm}} \right)^2 + \left(\frac{M_t}{M_t + M_p} K' \cos \theta_{\text{cm}} - K \right)^2} ,
\end{aligned} \tag{32}
$$

where

$$K = \frac{M_t}{M_t + M_b} K_{\text{in}} , \qquad K_{\text{in}} = \sqrt{2 M_b E_{\text{beam}}} , \qquad K' = \sqrt{\frac{M_s(M_t + M_p)}{M_s + M_t + M_p} (E_K + Q - E_T)} .$$

10.2 Peripheral cut parametrization

In our approach we used the assumption of rectangular shape of both spectator-participant and target-participant potentials. This treatment simplifies simplify the solution of the Schrödinger equation for the participant wave function in the initial (Ψ_{sp}) and final states (Ψ_{tp}) and includes in the T-matrix definition, see Equation (16).

For the plane wave representation we use the following partial wave decomposition:

$$\psi_{pw}(\mathbf{k}, \mathbf{r}) = e^{i\mathbf{k}\mathbf{r}} = 4\pi \sum_l i^l \frac{F_l(kr)}{kr} \sum_m Y^*_{lm}(\hat{k}) \, Y_{lm}(\hat{r}) , \tag{33}$$

where F_l is regular at the origin Bessel-Rikatti function, trivially connected with spherical Bessel functions and characterized by the corresponding asymptotics

$$F_l(kr) = (kr) \, j_l(kr) , \qquad F_l(kr) \to \sin\left(kr - l\frac{\pi}{2}\right) .$$

The behavior of the wave function beyond the potential barrier is denoted as K_l and expressed as follows:

$$K_l(r \to \infty) = \sqrt{\frac{2kr}{\pi}} K_{l+1/2}(kr) \sim \exp(-kr) ,$$

where $K_{l+1/2}(kr)$ is a modified Bessel function.

We assume the square well behavior for both $V_{tp}(\mathbf{r})$, $V_{sp}(\mathbf{r})$. These potentials were chosen so the Ψ_{tp} and Ψ_{sp} functions satisfy the continuity equation on the barrier borders and provide the correct result of the root-mean-square nuclear charge radii. The radii of ^{8}He and ^{3}He are 1.924
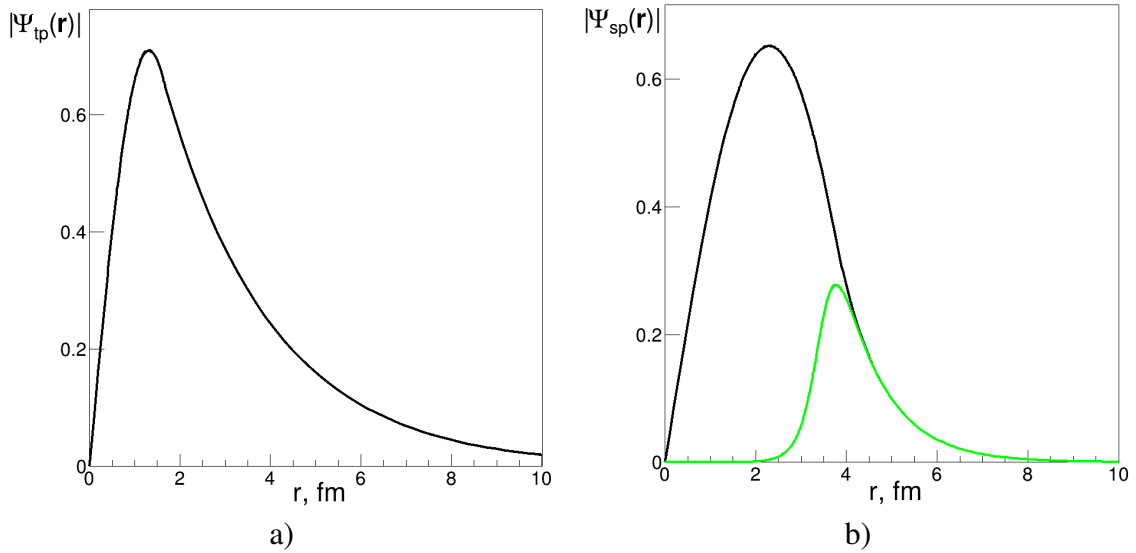
Figure 51: The participant (proton) wave functions $\Psi_{tp}(\mathbf{r})$ and $\Psi_{sp}(\mathbf{r})$ obtained in the square potential wells of ^{3}He ($V_{tp}(\mathbf{r})$) and ^{8}He ($V_{sp}(\mathbf{r})$). The green-line distribution illustrates the applied peripheral cut for the $\Psi_{sp}(\mathbf{r})$ function.

and 1.966 fm, taken from Ref. [100]. In the spherical coordinate system $\Psi_{tp}(\mathbf{r})$ and $\Psi_{sp}(\mathbf{r})$ obtained in this way as a functions of radius are presented in Fig. 51. The implementation of the peripheral behavior of the participant in its initial state is shown with the green-line function. The presented cut is realized by multiplying the initial "black" wave function by the Fermi-function and thus is characterized by two corresponded parameters: cut range and its diffusion.

The cut of the $\Psi_{sp}(\mathbf{r})$ function subsequently transforms the momentum formfactor $\Phi_{sp}(\mathbf{q})$ calculated using formula 18. Both formfactors as a functions of q_1, before and after peripheral cut, are presented in Fig. 52 a). Using the dependence of $q_1(\Theta_{CM})$, given in formula 32 and shown in Fig. 52 b) the simple visual analysis at this step tells about the behavior of the cross-section of the ground state population. Here and in the following discussion we suggest the ground state energy $E_T = 2.2(3)$ MeV, which corresponds to the observations, see Section 8.

The second factor of the formula 31 is the T-matrix calculated in the quasi-free approximation. From the Fig. 53 one may see its monotone decreasing behavior with increasing q_2, and therefore Θ_{CM}. That is why in the studied angular range $\Theta_{CM} < 45°$ the T-matrix does not affect the cross-section structure, but decrease its absolute value with the rising angle.

10.3   Results

For the two mentioned tasks two sets of cut range(R_{wf})-cut sigma (σ_{wf}) were obtained.

The cross-section, provided by the FRESCO calculations and presented in Section 4 has been reproduced with R_{wf}=6.1 fm and σ_{wf}=0.23 fm. The obtained cross-section with such parameters in compare with the one in Fig. 9 a) is presented in Fig. 54.

One may see that the developed model allowed to reproduce the center-of-mass angular distribution calculated by the FRESCO code with standard parameters for the reaction

a)   b)
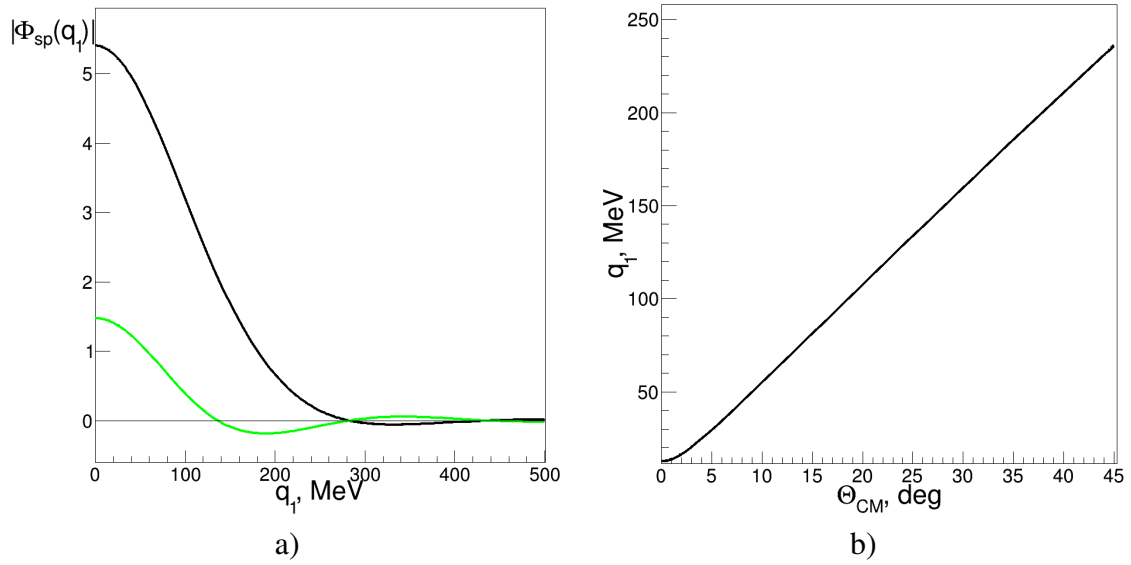
Figure 52: a) The proton formfactor $\Phi_{sp}(\mathbf{q_1})$ as a function of the transferred momentum q_1. The black and green-line distributions correspond to the initial and cut $\Psi_{sp}(\mathbf{r})$ function, see Fig. 51 b). b) The q_1 transferred momentum dependence on the reaction angle Θ_{CM} shown in the experimentally covered angles: 0-45°, see Fig. 32 c). Those q_1, and hence Θ_{CM}, at which $\Phi_{sp}(\mathbf{q})$ turns to zero correspond to the position of the cross-section minimums.

a)   b)
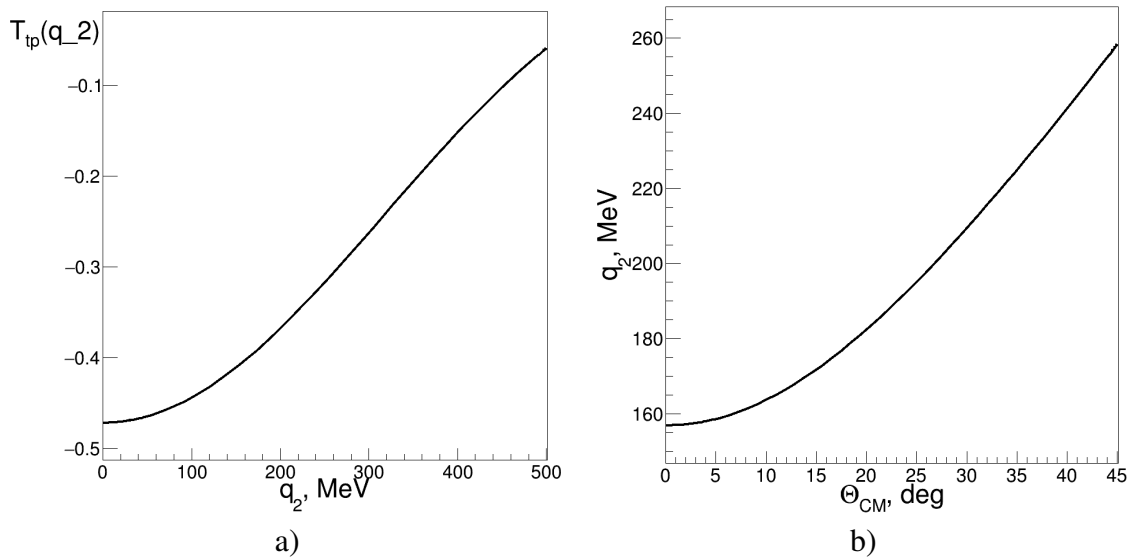
Figure 53: a) The proton T-matrix as a function of the transferred momentum q_2 calculated in the quasi-free assumption. b) The q_2 transferred momentum dependence on the reaction angle Θ_{CM}.

a)   b)
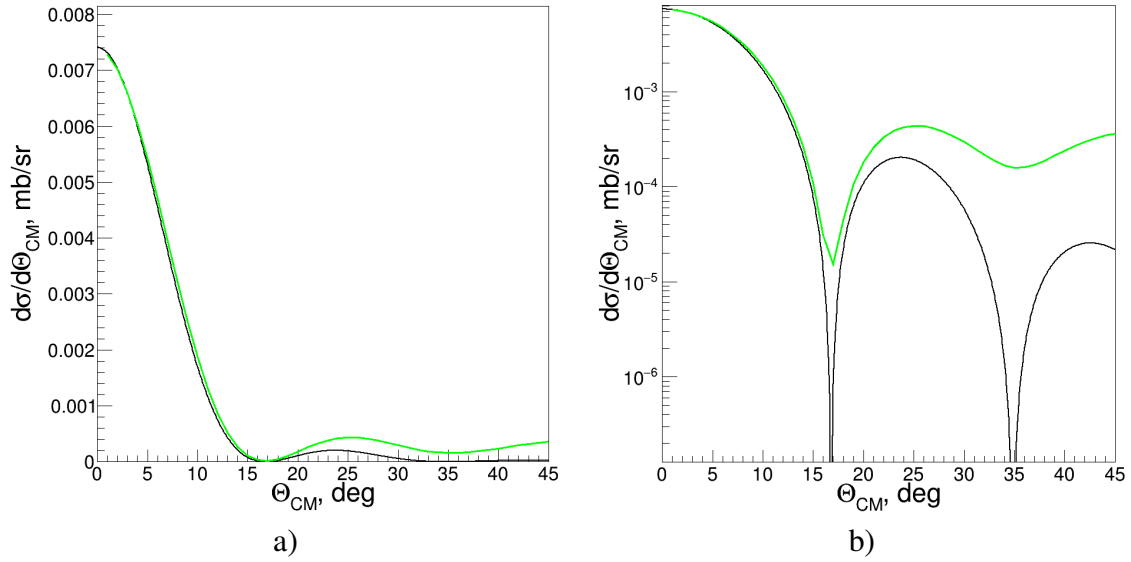
Figure 54: ^{2}H(^{8}He,^{3}He)^{7}H(g.s.) reaction angular distribution obtained by the developed model with R_{wf}=6.1 fm and σ_{wf}=0.23 fm is shown with black line function. The initial FRESCO results taken from Fig. 9 is presented with the green line function. Both functions are shown in the linear a) and logarithmic b) scale.

^{2}H(^{8}He,^{3}He)^{7}H(g.s.). The position of the first minimum as well as the cross-section absolute values at forward angles is reproduced with high precision. This result confirms the efficiency of the developed model, which makes it possible to choose the certain set of R_{wf} and σ_{wf} parameters and analyze the suggested extreme peripheral character of the ^{2}H(^{8}He,^{3}He)^{7}H reaction based on the experimentally observed results.

Due to the low collected statistics of the ^{7}H ground state population (14 events in two experiments) the observed center-of-mass angular distribution was reproduced with big errors. That is why criterion of results consistency should be agreement of the theoretical model with the data in both representations: before and after interpolation. The unexpected extremely low cross-section contradicting the FRESCO prediction implies the larger cut range R_{wf}. The model results for the selected parameters R_{wf}=8.79 fm and σ_{wf}=0.2 fm which best interpretates the collected data is presented in Fig. 55.

One may see that the structure of the obtained center-of-mass angular distribution (the black-line in Fig. 55) corresponds to the collected experimental data on all studied angular range. The important feature of the result is the lower the first and the second cross-section-minimum positions, which is obviously better fits the observation than the FRESCO result obtained in the similar peripheral cut assumption. The absolute cross-section values shown in b) panel are in good agreement with the FRESCO result. Thus, we may conclude that the developed model based on the plane-wave Born approximation is in agreement with both results: experimental and calculated by FRESCO, which confirms the suggestion of the extreme peripheral reaction character.

The Fig. 56 shows the reproduced Θ_{CM}-E$_T$ correlation with the embedded experimental data. In the above discussion we assumed that the E$_T$(^{7}H(g.s.))=2.2 MeV. The reproduced Θ_{CM}-E$_T$ gives the opportunity to analyze the cross-section for different excitation energies of the
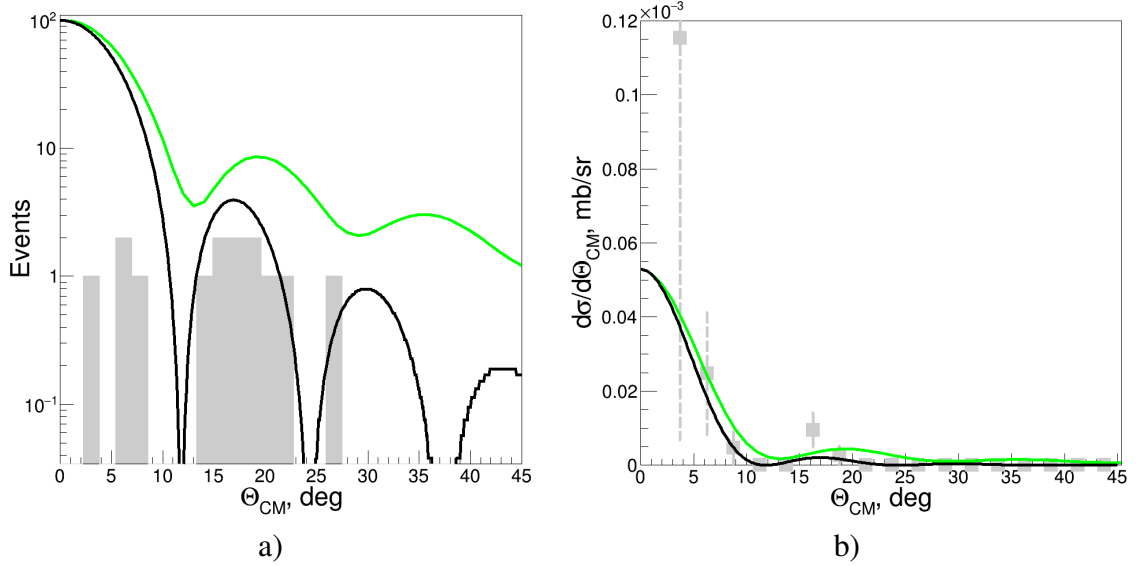
Figure 55: The center-of-mass angular distribution for the ^{2}H(^{8}He,^{3}He)^{7}H reaction reconstructed with R_{wf}=8.79 fm and σ_{wf}=0.2 fm. a) The ^{7}H ground state events collected in two experiments are shown with filled gray histograms. The black solid curve shows the theoretical calculations, which has arbitrary scaling here. b) The theoretical model result presented in the linear scale with overlaying efficiency corrected experimental data given in Fig. 38 a). The experimental data points are drawn with squares with the calculated errors. In both figures the FRESCO results performed in assumption of the extreme peripheral transfer (given as the blue dotted line in Fig. 9 a)) is shown with the green-line function.

studied system, which in conjunction with all presented results, makes the developed model a powerful tool for the direct transfer reaction studies.
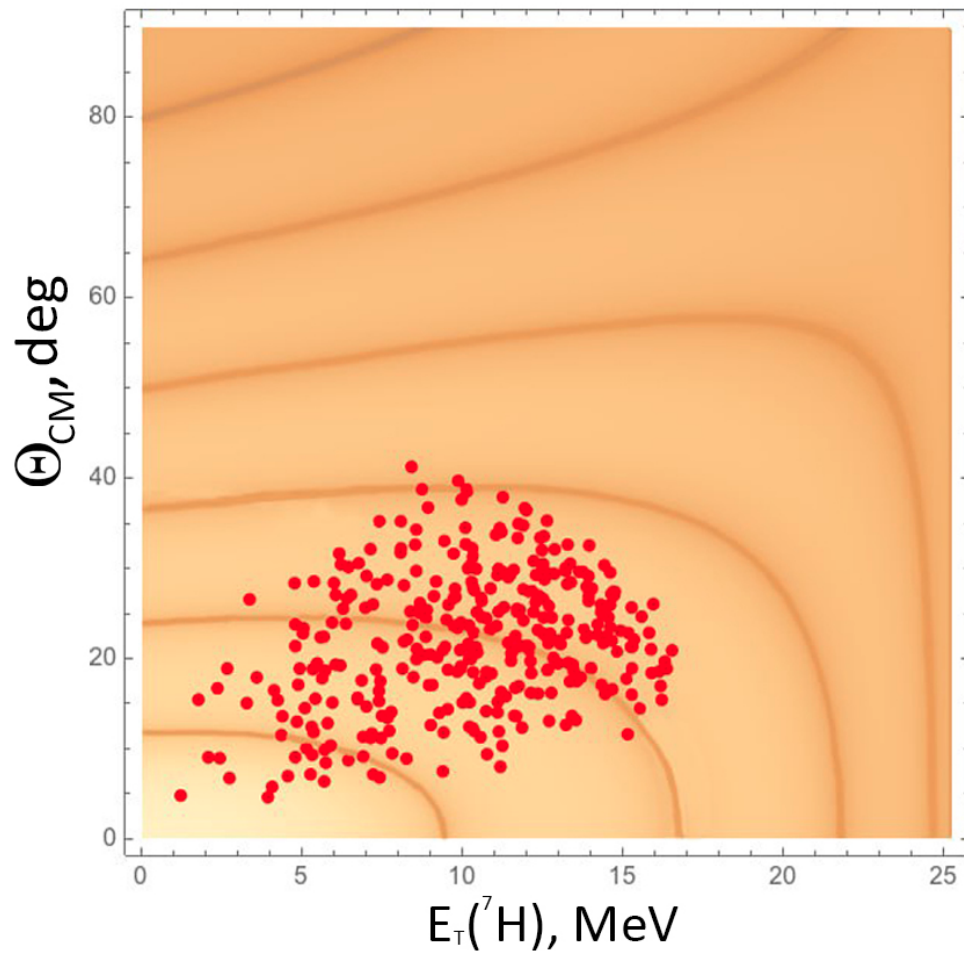
Figure 56: Correlation between the center-of-mass reaction angle and the ^{7}H excitation energy calculated within the developed model. The Z axis is shown in logarithmic scale for clarity of the cross-section structures at large angles and excitation energies. The red color dots correspond to the data of the second experimental run taken from Fig. 32 c).

11 Conclusions

This thesis reports the results of two experiments performed with the fragment separator ACCULINNA-2 in Flerov Laboratory of Nuclear Reactions, Joint Institute for Nuclear Research, Dubna. During both experiments we used the cryogenic gaseous deuterium target of 30 K at atmospheric pressure and the secondary beam of ^{8}He ions with energy of 26 AMeV. The latter was produced in the interaction of ^{11}B primary beam of 33.4 AMeV with beryllium target and separated by the in-flight technique. Having the the intensity of the primary beam of ≈ 1 pμA, ACCULINNA-2 facility produced ≈ 10 pps of ^{8}He ions. As a result of the ^{8}He-^{2}H interaction, the properties of ^{7}H populated in the proton transfer ^{2}H(^{8}He,^{3}He)^{7}H reaction and ^{6}H populated in deutron transfer ^{2}H(^{8}He,^{4}He)^{6}H reaction were investigated. Both ^{7}H and ^{6}H were studied by the missing mass method and reconstructed from the recoil ^{3}He and ^{4}He respectively. The beam diagnostic system consists of two BC404 plastic scintillators and two pairs of multiwire proportional chambers. The scintillators detectors provided the time-of-flight and energy loss information, used for the particle identification and the beam energy reconstruction. The charged reaction products were identified and measured by the ΔE-E telescopes. We used three layer ΔE-E-E (20 μm-1 mm-1 mm) telescopes consisted of silicon strip detectors for the low-energy recoil detection. The higher energy tritons produced in the ^{6}H or ^{7}H decay was measured by the the telescope consisted of one 1.5 mm-thick double-sided silicon strip detector followed by a square array of 16 CsI(Tl) crystals. During the second experimental run the emitted neutrons were measured by the time-of-flight scintillator stilbene modules placed behind the reaction chamber.

In addition to the main experimental runs with ^{8}He beam, just after experiment 2 the reference measurement with a 42 AMeV ^{10}Be secondary beam was conducted. It was performed with the same setup configuration as in the second run and allowed to test the methodics of the proton transfer reaction on the ^{2}H(^{10}Be,^{3}He)^{9}Li reaction, to control calibration parameters, and to estimate the missing mass resolution for the ^{7}H system.

For the interpretation of the experimental data on the ^{7}H ground state cross-section we developed a theoretical model based on the plane-wave Born approximation describing the sudden removal character of the ^{2}H(^{8}He,^{3}He)^{7}H(g.s.) reaction. The parameterization of the extremely peripheral character of this reaction was implemented into the model. We focused on both experimental data and the results obtained by the FRESCO code.

- For the first time the ground and the low-lying excited ^{7}H states were discovered at 2.2(5), 5.5(3), 7.5(3) MeV above the t+4n decay threshold. The recorded statistics of 483 events related to the ^{7}H population of was collected in two experimental runs. The results obtained in two conducted experiments are consistent with each other and the previous work [45]. The suggested reason for the poor ^{7}H ground state population with the cross-section ~ 24 μb/sr is the extreme peripheral character of this reaction. Although only 14 events of ^{7}H ground state population were collected, the applied kinematical triangle selection in conjunction with the consistency with the ^{7}H center-of-mass angular distribution, ^{3}H

energy distributions in the ^{7}H center-of-mass system and neutron coincidences allowed us to declare with confidence the ground state observation. The first excited state populated with cross section $\sim 30\,\mu$b/sr was observed at 5.5(3) MeV and interpreted as the 5/2 + member of the ^{7}H excitation doublet. Due to the low statistics and rising background contribution at ^{7}H higher energies, we could only suggest that the observed 7.5(3) MeV peak is the second 5/2+;3/2+ doublet member. For the same reason for the interpretation of the observed 11 MeV peak more investigation is needed.

- The idea of peripheral character of the ^{7}H ground state population was confirmed by the developed theoretical model. The calculated ^{2}H(^{8}He,^{3}He)^{7}H(g.s.) reaction cross section reproduced the FRESCO result and well described the experimental data. The demonstrated model efficiency gave us grounds to declare the prospects of this tool for the future direct reaction investigations.

- The ^{6}H resonance state at $E_T = 6.8$ MeV was observed in the reconstructed missing mass spectrum. The higher level of the background caused by the recoil ^{4}He detection requires additional analysis. The statistical analysis, the study of possible interfering reaction channels, in conjunction with the empty target (deuterium gas out) data confirmed the declared ^{6}H state observation. The deduced cross section of its population is $\simeq 190^{+40}_{-80}$ μb/sr. The observed peak can be a single state or can be an overlap of several relatively narrow states. Our suggestion is for two overlapping states, at $E_T =$4.5 and 6.8 MeV, which sets the minimum for the possible ^{6}H states. That is why in contradiction to the early works [46, 47, 43] our results indicate the absence of the ^{6}H resonances with $E_T <$ 3.5 MeV with the cross section limit $\lesssim 5\,\mu$b/sr. This result serves as an evidence of the true 5-body decay of ^{7}H in its ground state and an extremely strong "dineutron-type" correlation in the decay of the ^{5}H ground state.

- In the ^{2}H(^{10}Be,^{3}He)^{9}Li reaction the ^{9}Li ground state (3/2-) and its first excited state (2.69 MeV, 1/2-) were clearly observed in the low-energy region of its excitation spectrum. The cross-section values of $d\sigma/dE_T d\Omega \sim$7–10 mb/sr at forward angles in the center-of-mass system were deduced from these data for the reaction populating the ^{9}Li ground state. The Monte-Carlo simulation reproduced the observed ^{9}Li(g.s.) peak with the resolution of $\approx$2.2 MeV (FWHM). The latter corresponds to the resolution of the low-energy ^{7}H spectrum of $\approx$1.1 MeV. The obtained results provide the strong evidence of the reliability of the data interpretation of both ^{7}H and ^{6}H systems. In addition the collected results on the reference experiment is the subject of a separate investigation.

- In the frame of this work multiple experimental methodics were developed.

  i Employment of the 20-μm thick silicon strip detectors for the low-energy charged particle identification and reconstruction [86].

  ii Neutron measurement with the developed neutron spectrometer based on stilbene crystals. The demonstrated confident n-γ discrimination and energy reconstruction

from the neutron time-of-flight provided unique information on the studied ^{6,7}H systems.

iii The applied data analysis methods (kinematical triangle selection gate, correlation channels analysis, background subtraction procedure, etc.) demonstrated their efficiency and are a significant tool for the experimental nuclear physics.

iv Thus, these results showed the great potential of the ACCULINNA-2 fragment separator and allowed to substantially expand the experimental capabilities and, at a qualitatively new level, to carry out correlation experiments with radioactive beams.

References

[1] L. V. Grigorenko, M. S. Golovkov, S. A. Krupko, S. I. Sidorchuk, G. M. Ter-Akopian, A. S. Fomichev, and V. Chudoba. Studies of light exotic nuclei in the vicinity of neutron and proton drip lines at flnr jinr. *Physics-Uspekhi*, 59(4):321, 2016.

[2] L. V. Grigorenko, B. Yu. Sharkov, A. S. Fomichev, A. L. Barabanov, W. Bart, A. A. Bezbakh, S. L. Bogomolov, M. S. Golovkov, A. V. Gorshkov, S. N. Dmitriev, V. K. Eremin, S. N. Ershov, M. V. Zhukov, I. V. Kalagin, A. V. Karpov, T. Katayama, O. A. Kiselev, A. A. Korsheninnikov, S. A. Krupko, T. V. Kulevoy, Yu. A. Litvinov, E. V. Lychagin, I. P. Maksimkin, I. N. Meshkov, I. G. Mukha, E. Yu. Nikolskii, Yu. L. Parfenova, V. V. Parkhomchuk, S. M. Polozov, M. Pfutzner, S. I. Sidorchuk, H. Simon, R. S. Slepnev, G. M. Ter-Akopian, G. V. Trubnikov, V. Chudoba, C. Scheidenberger, P. G. Sharov, P. Yu. Shatunov, Yu. M. Shatunov, V. N. Shvetsov, N. B. Shulgina, A. A. Yukhimchuk, and S. Yaramyshev. Scientific program of DERICA – prospective accelerator and storage ring facility for radioactive ion beam research. *Physics-Uspekhi*, 62(7):675–690, jul 2019.

[3] P.G. Hansen and B. Jonson. The neutron halo of extremely neutron-rich nuclei. *Europhys. Lett.*, 4:409, 1987.

[4] Isao Tanihata, Herve Savajols, and Rituparna Kanungo. Recent experimental progress in nuclear halo structure studies. *Progress in Particle and Nuclear Physics*, 68:215–313, 2013.

[5] A.A. Korsheninnikov, E.Yu. Nikolskii, C.A. Bertulani, S. Fukuda, T. Kobayashi, E.A. Kuzmin, S. Momota, B.G. Novatskii, A.A. Ogloblin, A. Ozawa, V. Pribora, I. Tanihata, and K. Yoshida. Scattering of radioactive nuclei 6he and 3h by protons: Effects of neutron skin and halo in 6he, 8he, and 11li. *Nuclear Physics A*, 617(1):45–56, 1997.

[6] D.F. Geesaman, C.K. Gelbke, R.V.F. Janssens, and B.M. Sherrill. Physics of a rare isotope accelerator. *Annual Review of Nuclear and Particle Science*, 56(1):53–92, 2006.

[7] M. V. Zhukov, B.V. Danilin, D.V. Fedorov, J.M. Bang, I.J. Thompson, and J.S.Vaagen. Bound state properties of the borromean halo nuclei: ^{6}he and ^{11}li. *Phys. Rep.*, 231:151–199, 1993.

[8] L. V. Grigorenko. Theoretical study of two-proton radioactivity. status and predictions and and applications. *Physics of Particles and Nuclei*, 40:674–714, 2009.

[9] L.V. Grigorenko, K. Langanke, N.B. Shul'gina, and M.V. Zhukov. Soft dipole mode in ^{17}Ne and the astrophysical $2p$ capture on ^{15}O. *Physics Letters B*, 641(3):254–259, 2006.

[10] L. V. Grigorenko and M. V. Zhukov. Three-body resonant radioactive capture reactions in astrophysics. *Phys. Rev. C*, 72:015803, 2005.

[11] H. Schatz, A. Aprahamian, J. Gorresa, M. Wiescher, T. Rauscherb, J.F. Rembges, F.-K. Thielemann, P. Mtjller B. Pfeiffer, K.-L. Kratz, H. Herndld, B.A. Brown, and H. Rebel. rp-process nucleosynthesis at extreme temperature and density conditions. *Physics Reports*, 294:167–263, 1998.

[12] Joachim Görres, Michael Wiescher, and Friedrich-Karl Thielemann. Bridging the waiting points: The role of two-proton capture reactions in the rp process. *Phys. Rev. C*, 51:392–400, Jan 1995.

[13] V.I. Zagrebaev. *Heavy Ion Reactions at Low Energies*. Springer International Publishing.

[14] Ian Thompson and Filomena Nunes. *Nuclear Reactions for Astrophysics*. 07 2009.

[15] G.R. Satchler. *Direct nuclear reactions*. United Kingdom: Clarendon Press 1983.

[16] Norman K. Glendenning. *Direct nuclear reactions*. New York: Academic Press 1983.

[17] Yu. E. Penionzhkevich and R. G. Kalpakchieva. *Light Exotic Nuclei Near the Boundary of Neutron Stability*. WORLD SCIENTIFIC, 2021.

[18] S. I. Sidorchuk, A. A. Bezbakh, V. Chudoba, I. A. Egorova, A. S. Fomichev, M. S. Golovkov, A. V. Gorshkov, V. A. Gorshkov, L. V. Grigorenko, P. Jalůvková, G. Kaminski, S. A. Krupko, E. A. Kuzmin, E. Yu. Nikolskii, Yu. Ts. Oganessian, Yu. L. Parfenova, P. G. Sharov, R. S. Slepnev, S. V. Stepantsov, G. M. Ter-Akopian, R. Wolski, A. A. Yukhimchuk, S. V. Filchagin, A. A. Kirdyashkin, I. P. Maksimkin, and O. P. Vikhlyantsev. Structure of ^{10}He low-lying states uncovered by correlations. *Phys. Rev. Lett.*, 108:202502, May 2012.

[19] Z. Kohley, J. Snyder, T. Baumann, G. Christian, P. A. DeYoung, J. E. Finck, R. A. Haring-Kaye, M. Jones, E. Lunderberg, B. Luther, S. Mosby, A. Simon, J. K. Smith, A. Spyrou, S. L. Stephenson, and M. Thoennessen. Unresolved question of the ^{10}He ground state resonance. *Phys. Rev. Lett.*, 109:232501, Dec 2012.

[20] M. D. Jones, Z. Kohley, T. Baumann, G. Christian, P. A. DeYoung, J. E. Finck, N. Frank, R. A. Haring-Kaye, A. N. Kuchera, B. Luther, S. Mosby, J. K. Smith, J. Snyder, A. Spyrou, S. L. Stephenson, and M. Thoennessen. Further insights into the reaction ^{14}Be(CH$_2$,x)^{10}He. *Phys. Rev. C*, 91:044312, Apr 2015.

[21] A. Matta, D. Beaumel, H. Otsu, V. Lapoux, N. K. Timofeyuk, N. Aoi, M. Assié, H. Baba, S. Boissinot, R. J. Chen, F. Delaunay, N. de Sereville, S. Franchoo, P. Gangnant, J. Gibelin, F. Hammache, Ch. Houarner, N. Imai, N. Kobayashi, T. Kubo, Y. Kondo, Y. Kawada, L. H. Khiem, M. Kurata-Nishimura, E. A. Kuzmin, J. Lee, J. F. Libin, T. Motobayashi, T. Nakamura, L. Nalpas, E. Yu. Nikolskii, A. Obertelli, E. C. Pollacco, E. Rindel, Ph. Rosier, F. Saillant, T. Sako, H. Sakurai, A. M. Sánchez-Benítez, J-A.

Scarpaci, I. Stefan, D. Suzuki, K. Takahashi, M. Takechi, S. Takeuchi, H. Wang, R. Wol-ski, and K. Yoneda. New findings on structure and production of ^{10}He from ^{11}Li with the $(d,^3\text{He})$ reaction. *Phys. Rev. C*, 92:041302, Oct 2015.

[22] H. T. Johansson, Yu. Aksyutina, T. Aumann, K. Boretzky, M. J. G. Borge, A. Chatil-lon, L. V. Chulkov, D. Cortina-Gil, U. Datta Pramanik, H. Emling, C. Forssen, H. O. U. Fynbo, H. Geissel, G. Ickert, B. Jonson, R. Kulessa, C. Langer, M. Lantz, T. LeBleis, K. Mahata, M. Meister, G. Munzenberg, T. Nilsson, G. Nyman, R. Palit, S. Paschalis, W. Prokopowicz, R. Reifarth, A. Richter, K. Riisager, G. Schrieder, N. B. Shulgina, H. Simon, K. Summerer, O. Tengblad, H. Weick, and M. V. Zhukov. Three-body corre-lations in the decay of ^{10}he and ^{13}li. *Nucl. Phys. A*, 847:66, 2010.

[23] Z. Kohley, E. Lunderberg, P. A. DeYoung, A. Volya, T. Baumann, D. Bazin, G. Christian, N. L. Cooper, N. Frank, A. Gade, C. Hall, J. Hinnefeld, B. Luther, S. Mosby, W. A. Peters, J. K. Smith, J. Snyder, A. Spyrou, and M. Thoennessen. First observation of the ^{13}li ground state. *Phys. Rev. C*, 87:011304, Jan 2013.

[24] A. Spyrou, Z. Kohley, T. Baumann, D. Bazin, B. A. Brown, G. Christian, P. A. DeYoung, J. E. Finck, N. Frank, E. Lunderberg, S. Mosby, W. A. Peters, A. Schiller, J. K. Smith, J. Snyder, M. J. Strongman, M. Thoennessen, and A. Volya. First observation of ground state dineutron decay: ^{16}Be. *Phys. Rev. Lett.*, 108:102501, Mar 2012.

[25] S. Leblond, F. M. Marqués, J. Gibelin, N. A. Orr, Y. Kondo, T. Nakamura, J. Bonnard, N. Michel, N. L. Achouri, T. Aumann, H. Baba, F. Delaunay, Q. Deshayes, P. Door-nenbal, N. Fukuda, J. W. Hwang, N. Inabe, T. Isobe, D. Kameda, D. Kanno, S. Kim, N. Kobayashi, T. Kobayashi, T. Kubo, J. Lee, R. Minakata, T. Motobayashi, D. Murai, T. Murakami, K. Muto, T. Nakashima, N. Nakatsuka, A. Navin, S. Nishi, S. Ogoshi, H. Otsu, H. Sato, Y. Satou, Y. Shimizu, H. Suzuki, K. Takahashi, H. Takeda, S. Takeuchi, R. Tanaka, Y. Togano, A. G. Tuff, M. Vandebrouck, and K. Yoneda. First observation of ^{20}B and ^{21}B. *Phys. Rev. Lett.*, 121:262502, Dec 2018.

[26] Z. Kohley, T. Baumann, D. Bazin, G. Christian, P. A. DeYoung, J. E. Finck, N. Frank, M. Jones, E. Lunderberg, B. Luther, S. Mosby, T. Nagi, J. K. Smith, J. Snyder, A. Spyrou, and M. Thoennessen. Study of two-neutron radioactivity in the decay of ^{26}O. *Phys. Rev. Lett.*, 110:152501, Apr 2013.

[27] C. Caesar, J. Simonis, T. Adachi, Y. Aksyutina, J. Alcantara, S. Altstadt, H. Alvarez-Pol, N. Ashwood, T. Aumann, V. Avdeichikov, M. Barr, S. Beceiro, D. Bemmerer, J. Benlliure, C. A. Bertulani, K. Boretzky, M. J. G. Borge, G. Burgunder, M. Caa-mano, E. Casarejos, W. Catford, J. Cederkäll, S. Chakraborty, M. Chartier, L. Chulkov, D. Cortina-Gil, U. Datta Pramanik, P. Diaz Fernandez, I. Dillmann, Z. Elekes, J. Enders, O. Ershova, A. Estrade, F. Farinon, L. M. Fraile, M. Freer, M. Freudenberger, H. O. U. Fynbo, D. Galaviz, H. Geissel, R. Gernhäuser, P. Golubev, D. Gonzalez Diaz, J. Hagdahl,

T. Heftrich, M. Heil, M. Heine, A. Heinz, A. Henriques, M. Holl, J. D. Holt, G. Ickert, A. Ignatov, B. Jakobsson, H. T. Johansson, B. Jonson, N. Kalantar-Nayestanaki, R. Kanungo, A. Kelic-Heil, R. Knöbel, T. Kröll, R. Krücken, J. Kurcewicz, M. Labiche, C. Langer, T. Le Bleis, R. Lemmon, O. Lepyoshkina, S. Lindberg, J. Machado, J. Marganiec, V. Maroussov, J. Menéndez, M. Mostazo, A. Movsesyan, A. Najafi, T. Nilsson, C. Nociforo, V. Panin, A. Perea, S. Pietri, R. Plag, A. Prochazka, A. Rahaman, G. Rastrepina, R. Reifarth, G. Ribeiro, M. V. Ricciardi, C. Rigollet, K. Riisager, M. Röder, D. Rossi, J. Sanchez del Rio, D. Savran, H. Scheit, A. Schwenk, H. Simon, O. Sorlin, V. Stoica, B. Streicher, J. Taylor, O. Tengblad, S. Terashima, R. Thies, Y. Togano, E. Uberseder, J. Van de Walle, P. Velho, V. Volkov, A. Wagner, F. Wamers, H. Weick, M. Weigand, C. Wheldon, G. Wilson, C. Wimmer, J. S. Winfield, P. Woods, D. Yakorev, M. V. Zhukov, A. Zilges, M. Zoric, and K. Zuber. Beyond the neutron drip line: The unbound oxygen isotopes ^{25}o and ^{26}o. *Phys. Rev. C*, 88:034313, Sep 2013.

[28] Y. Kondo, T. Nakamura, R. Tanaka, R. Minakata, S. Ogoshi, N. A. Orr, N. L. Achouri, T. Aumann, H. Baba, F. Delaunay, P. Doornenbal, N. Fukuda, J. Gibelin, J. W. Hwang, N. Inabe, T. Isobe, D. Kameda, D. Kanno, S. Kim, N. Kobayashi, T. Kobayashi, T. Kubo, S. Leblond, J. Lee, F. M. Marqués, T. Motobayashi, D. Murai, T. Murakami, K. Muto, T. Nakashima, N. Nakatsuka, A. Navin, S. Nishi, H. Otsu, H. Sato, Y. Satou, Y. Shimizu, H. Suzuki, K. Takahashi, H. Takeda, S. Takeuchi, Y. Togano, A. G. Tuff, M. Vandebrouck, and K. Yoneda. Nucleus ^{26}O: A barely unbound system beyond the drip line. *Phys. Rev. Lett.*, 116:102503, Mar 2016.

[29] D. S. Ahn, N. Fukuda, H. Geissel, N. Inabe, N. Iwasa, T. Kubo, K. Kusaka, D. J. Morrissey, D. Murai, T. Nakamura, M. Ohtake, H. Otsu, H. Sato, B. M. Sherrill, Y. Shimizu, H. Suzuki, H. Takeda, O. B. Tarasov, H. Ueno, Y. Yanagisawa, and K. Yoshida. Location of the neutron dripline at fluorine and neon. *Phys. Rev. Lett.*, 123:212501, Nov 2019.

[30] H. T. Fortune. Structure of exotic light nuclei: Z = 2, 3, 4. *Eur. Phys. J. A*, 54:51, 2018.

[31] A. I. Baz', V. I. Goldansky, V. Z. Goldberg, and Ya. B. Zeldovich. *Light and intermediate nuclei near the border of nuclear stability*. Nauka, Moscow, Moscow, 1972.

[32] K.K. Seth. Pionic probes for exotic nuclei. (81-09-655), 1981.

[33] V.S. Evseev, V.S. Kurbatov, V.M. Sidorov, V.B. Belyaev, J. Wrzecionko, M. Daum, R. Frosch, J. McCulloch, and E. Steiner. Experimental study of π^- double charge exchange with ^{7}li. *Nuclear Physics A*, 352(3):379 – 387, 1981.

[34] M. S. Golovkov, L. V. Grigorenko, A. S. Fomichev, Yu. Ts. Oganessian, Yu. I. Orlov, A. M. Rodin, S. I. Sidorchuk, R. S. Slepnev, S. V. Stepantsov, G. M. Ter-Akopian, and R. Wolski. Estimates of the ^{7}h width and lower decay energy limit. *Phys. Lett. B*, 588:163, 2004.

[35] A. A. Korsheninnikov, M. S. Golovkov, I. Tanihata, A. M. Rodin, A. S. Fomichev, S. I. Sidorchuk, S. V. Stepantsov, M. L. Chelnokov, V. A. Gorshkov, D. D. Bogdanov, R. Wolski, G. M. Ter-Akopian, Yu. Ts. Oganessian, W. Mittig, P. Roussel-Chomaz, H. Savajols, E. A. Kuzmin, E. Yu. Nikolskii, and A. A. Ogloblin. Superheavy hydrogen ^5h. *Phys. Rev. Lett.*, 87:092501, Aug 2001.

[36] N. K. Timofeyuk. Shell model approach to construction of a hyperspherical basis for a identical particles: Application to hydrogen and helium isotopes. *Phys. Rev. C*, 65:064306, May 2002.

[37] A. A. Korsheninnikov, E. Yu. Nikolskii, E. A. Kuzmin, A. Ozawa, K. Morimoto, F. Tokanai, R. Kanungo, I. Tanihata, N. K. Timofeyuk, M. S. Golovkov, A. S. Fomichev, A. M. Rodin, M. L. Chelnokov, G. M. Ter-Akopian, W. Mittig, P. Roussel-Chomaz, H. Savajols, E. Pollacco, A. A. Ogloblin, and M. V. Zhukov. Experimental evidence for the existence of ^{7}H and for a specific structure of ^{8}He. *Phys. Rev. Lett.*, 90:082501, Feb 2003.

[38] S. Aoyama and N. Itagaki. Systematic analyses on h- and he-isotopes by using an extended amd approach. *Nuclear Physics A*, 738:362 – 366, 2004. Proceedings of the 8th International Conference on Clustering Aspects of Nuclear Structure and Dynamics.

[39] S. Aoyama and N. Itagaki. Di-neutron correlations in ^{7}H. *Phys. Rev. C*, 80:021304, Aug 2009.

[40] Yu.B. Gurov, B.A. Chernyshev, S.V. Isakov, V. S. Karpukhin, S.V. Lapushkin, I. V. Laukhin, V. A. Pechkurov, N. O. Poroshin, and V.G. Sandukovsky. Search for superheavy hydrogen isotopes ^{6}h and ^{7}h in stopped π-absorption reactions. *The European Physical Journal A*, 32(3):261–266, 2007.

[41] Yu.B. Gurov, S.V. Lapushkin, B.A. Chernyshev, and V.G. Sandukovsky. Search for superheavy hydrogen isotopes in pion absorption reactions. *Physics of Particles and Nuclei*, 40(4):558–581, 2009.

[42] M. Caamaño, D. Cortina-Gil, W. Mittig, H. Savajols, M. Chartier, C. E. Demonchy, B. Fernández, M. B. Gómez Hornillos, A. Gillibert, B. Jurado, O. Kiselev, R. Lemmon, A. Obertelli, F. Rejmund, M. Rejmund, P. Roussel-Chomaz, and R. Wolski. Resonance state in ^{7}H. *Phys. Rev. Lett.*, 99:062502, Aug 2007.

[43] M. Caamaño, D. Cortina-Gil, W. Mittig, H. Savajols, M. Chartier, C. E. Demonchy, B. Fernández, M. B. Gómez Hornillos, A. Gillibert, B. Jurado, O. Kiselev, R. Lemmon, A. Obertelli, F. Rejmund, M. Rejmund, P. Roussel-Chomaz, and R. Wolski. Experimental study of resonance states in ^{7}H and ^{6}H. *Phys. Rev. C*, 78:044001, Oct 2008.

[44] S. Fortier, E. Tryggestad, E. Rich, D. Beaumel, E. Becheva, Y. Blumenfeld, F. Delaunay, A. Drouart, A. Fomichev, N. Frascaria, S. Gales, L. Gaudefroy, A. Gillibert, J. Guillot,

F. Hammache, K. W. Kemper, E. Khan, V. Lapoux, V. Lima, L. Nalpas, A. Obertelli, E. C. Pollacco, F. Skaza, U. Datta Pramanik, P. Roussel-Chomaz, D. Santonocito, J. A. Scarpaci, O. Sorlin, S. V. Stepantsov, G. M. Ter Akopian, and R. Wolski. Search for resonances in 4n, 7h and 9he via transfer reactions. *AIP Conference Proceedings*, 912(1):3–12, 2007.

[45] E. Yu. Nikolskii, A. A. Korsheninnikov, H. Otsu, H. Suzuki, K. Yoneda, H. Baba, K. Yamada, Y. Kondo, N. Aoi, A. S. Denikin, M. S. Golovkov, A. S. Fomichev, S. A. Krupko, M. Kurokawa, E. A. Kuzmin, I. Martel, W. Mittig, T. Motobayashi, T. Nakamura, M. Niikura, S. Nishimura, A. A. Ogloblin, P. Roussel-Chomaz, A. Sanchez-Benitez, Y. Satou, S. I. Sidorchuk, T. Suda, S. Takeuchi, K. Tanaka, G. M. Ter-Akopian, Y. Togano, and M. Yamaguchi. Search for ^{7}H in ^{2}H$+^8$He collisions. *Phys. Rev. C*, 81:064606, Jun 2010.

[46] D.V. Aleksandrov, E.A. Ganza, Yu.A.Glukhov, B.G.Novatsky, A.A.Ogloblin, and D.N.Stepanov. Observation of nonstable heavy hydrogen isotope 6h in the reaction 7li(7li, 8b). *Yad. Fiz.*, 39:513, 1984.

[47] A.V. Belozyorov, C. Borcea, Z. Dlouhy, A.M. Kalinin, R. Kalpakchieva, Nguyen Hoai Chau, Yu.Ts. Oganessian, and Yu.E. Penionzhkevich. Search for 4h, 5h and 6h nuclei in the 11b-induced reaction on 9be. *Nuclear Physics A*, 460:352–360, 1986.

[48] B. Parker, Kamal K. Seth, and R. Soundranayagam. Search for superheavy hydrogen-6. *Physics Letters B*, 251(4):483–487, 1990.

[49] A. V. Germanov A. M. Gorbatov P. V. Komarov, P. Yu. Nikishov and D. V. Nechaev. *Sov. J. Nucl. Phys.*, 50:962, 1989. [Yad. Fiz. 1551].

[50] Ya. B. Zeldovich. On existence of new isotopes of light nuclei and neutron equation of state. *Sov. Phys. JETP*, 38:1123, 1960.

[51] V. I. Goldansky. On neutron-deficient isotopes of light nuclei and the phenomena of proton and two-proton radioactivity. *Nucl. Phys.*, 19:482–495, 1960.

[52] H.B. Willard, J.K. Bair, and C.M. Jones. N-d scattering: A search for effects due to the dineutron. *Physics Letters*, 9(4):339–341, 1964.

[53] A.V. Belozyorov, C. Borcea, Z. Dlouhy, A.M. Kalinin, Nguyen Hoai Chau, and Yu.E. Penionzhkevich. Search for the tri- and tetra-neutron in reactions induced by 11b and 9be ions on 7li. *Nuclear Physics A*, 477(1):131–142, 1988.

[54] F. M. Marqués, M. Labiche, N. A. Orr, J. C. Angélique, L. Axelsson, B. Benoit, U. C. Bergmann, M. J. G. Borge, W. N. Catford, S. P. G. Chappell, N. M. Clarke, G. Costa, N. Curtis, A. D'Arrigo, E. de Góes Brennand, F. de Oliveira Santos, O. Dorvaux, G. Fazio, M. Freer, B. R. Fulton, G. Giardina, S. Grévy, D. Guillemaud-Mueller,

F. Hanappe, B. Heusch, B. Jonson, C. Le Brun, S. Leenhardt, M. Lewitowicz, M. J. López, K. Markenroth, A. C. Mueller, T. Nilsson, A. Ninane, G. Nyman, I. Piqueras, K. Riisager, M. G. Saint Laurent, F. Sarazin, S. M. Singer, O. Sorlin, and L. Stuttgé. Detection of neutron clusters. *Phys. Rev. C*, 65:044006, Apr 2002.

[55] K. Kisamori, S. Shimoura, H. Miya, S. Michimasa, S. Ota, M. Assie, H. Baba, T. Baba, D. Beaumel, M. Dozono, T. Fujii, N. Fukuda, S. Go, F. Hammache, E. Ideguchi, N. Inabe, M. Itoh, D. Kameda, S. Kawase, T. Kawabata, M. Kobayashi, Y. Kondo, T. Kubo, Y. Kubota, M. Kurata-Nishimura, C. S. Lee, Y. Maeda, H. Matsubara, K. Miki, T. Nishi, S. Noji, S. Sakaguchi, H. Sakai, Y. Sasamoto, M. Sasano, H. Sato, Y. Shimizu, A. Stolz, H. Suzuki, M. Takaki, H. Takeda, S. Takeuchi, A. Tamii, L. Tang, H. Tokieda, M. Tsumura, T. Uesaka, K. Yako, Y. Yanagisawa, R. Yokoyama, and K. Yoshida. Candidate resonant tetraneutron state populated by the ^{4}He(^{8}He,^{8}Be) reaction. *Phys. Rev. Lett.*, 116:052501, Feb 2016.

[56] Steven C. Pieper. Can modern nuclear hamiltonians tolerate a bound tetraneutron? *Phys. Rev. Lett.*, 90:252501, Jun 2003.

[57] N K Timofeyuk. Do multineutrons exist? *Journal of Physics G: Nuclear and Particle Physics*, 29(2):L9–L14, Jan 2003.

[58] Michael D. Higgins, Chris H. Greene, A. Kievsky, and M. Viviani. Comprehensive study of the three- and four-neutron systems at low energies. *Phys. Rev. C*, 103:024004, Feb 2021.

[59] A. M. Shirokov, G. Papadimitriou, A. I. Mazur, I. A. Mazur, R. Roth, and J. P. Vary. Prediction for a four-neutron resonance. *Phys. Rev. Lett.*, 117:182502, Oct 2016.

[60] A. S. Fomichev, L. V. Grigorenko, S. A. Krupko, S. V. Stepantsov, and G. M. Ter-Akopian. The acculinna-2 project: The physics case and technical challenges. *The European Physical Journal A*, 54(6):97, Jun 2018.

[61] H. Geissel, P. Armbruster, K.H. Behr, A. Brünle, K. Burkard, M. Chen, H. Folger, B. Franczak, H. Keller, O. Klepper, B. Langenbeck, F. Nickel, E. Pfeng, M. Pfützner, E. Roeckl, K. Rykaczewski, I. Schall, D. Schardt, C. Scheidenberger, K.-H. Schmidt, A. Schröter, T. Schwab, K. Sümmerer, M. Weber, G. Münzenberg, T. Brohm, H.-G. Clerc, M. Fauerbach, J.-J. Gaimard, A. Grewe, E. Hanelt, B. Knödler, M. Steiner, B. Voss, J. Weckenmann, C. Ziegler, A. Magel, H. Wollnik, J.P. Dufour, Y. Fujita, D.J. Vieira, and B. Sherrill. The gsi projectile fragment separator (frs): a versatile magnetic system for relativistic heavy ions. *Nuclear Instruments and Methods in Physics Research Section B: Beam Interactions with Materials and Atoms*, 70(1):286–297, 1992.

[62] H. Geissel, H. Weick, M. Winkler, G. Münzenberg, V. Chichkine, M. Yavor, T. Aumann, K.H. Behr, M. Böhmer, A. Brünle, K. Burkard, J. Benlliure, D. Cortina-Gil, L. Chulkov,

A. Dael, J.-E. Ducret, H. Emling, B. Franczak, J. Friese, B. Gastineau, J. Gerl, R. Gernhäuser, M. Hellström, B. Jonson, J. Kojouharova, R. Kulessa, B. Kindler, N. Kurz, B. Lommel, W. Mittig, G. Moritz, C. Mühle, J.A. Nolen, G. Nyman, P. Roussell-Chomaz, C. Scheidenberger, K.-H. Schmidt, G. Schrieder, B.M. Sherrill, H. Simon, K. Sümmerer, N.A. Tahir, V. Vysotsky, H. Wollnik, and A.F. Zeller. The super-frs project at gsi. *Nuclear Instruments and Methods in Physics Research Section B: Beam Interactions with Materials and Atoms*, 204:71–85, 2003. 14th International Conference on Electromagnetic Isotope Separators and Techniques Related to their Applications.

[63] M. Winkler, H. Geissel, H. Weick, B. Achenbach, K.-H. Behr, D. Boutin, A. Brünle, M. Gleim, W. Hüller, C. Karagiannis, A. Kelic, B. Kindler, E. Kozlova, H. Leibrock, B. Lommel, G. Moritz, C. Mühle, G. Münzenberg, C. Nociforo, W. Plass, C. Scheidenberger, H. Simon, K. Sümmerer, N.A. Tahir, A. Tauschwitz, M. Tomut, J.S. Winfield, and M. Yavor. The status of the super-frs in-flight facility at fair. *Nuclear Instruments and Methods in Physics Research Section B: Beam Interactions with Materials and Atoms*, 266(19):4183–4187, 2008. Proceedings of the XVth International Conference on Electromagnetic Isotope Separators and Techniques Related to their Applications.

[64] B.S. Gao, M.A. Najafi, D.R. Atanasov, K. Blaum, F. Bosch, C. Brandau, X.C. Chen, I. Dillmann, Ch. Dimopoulou, Th. Faestermann, P.-M. Hillenbrand, H. Geissel, R. Gernhäuser, C. Kozhuharov, O. Kovalenko, S.A. Litvinov, Yu.A. Litvinov, L. Maier, F. Nolden, J. Piotrowski, M.S. Sanjari, U. Spillmann, M. Steck, Th. Stöhlker, Ch. Trageser, X.L. Tu, H. Weick, N. Winckler, H.S. Xu, T. Yamaguchi, X.L. Yan, Y.H. Zhang, and X.H. Zhou. Experiments with stored highly charged ions at the border between atomic and nuclear physics. *Physics Procedia*, 66:28–38, 2015. The 23rd International Conference on the Application of Accelerators in Research and Industry - CAARI 2014.

[65] Toshiyuki Kubo. In-flight ri beam separator bigrips at riken and elsewhere in japan. *Nuclear Instruments and Methods in Physics Research Section B: Beam Interactions with Materials and Atoms*, 204:97–113, 2003. 14th International Conference on Electromagnetic Isotope Separators and Techniques Related to their Applications.

[66] G. Cuttone, L. Celona, F. Chines, G. Cosentino, E. Messina, M. Re, D. Rizzo, V. Scuderi, F. Tudisco, A. Amato, L. Calabretta, G. De Luca, A. Pappalardo, S. Passarello, D. Rifuggiato, and A. Rovelli. Excyt: The rib project at infn-lns. *Nuclear Instruments and Methods in Physics Research Section B: Beam Interactions with Materials and Atoms*, 261(1):1040–1043, 2007. The Application of Accelerators in Research and Industry.

[67] The grand accélérateur national ions lourds (ganil). http://www.ganil-spiral2.eu/.

[68] Isolde. https://isolde.cern/.

[69] A.V. Gorshkov, S.G. Belogurov, D. Biare A.A. Bezbakh, W. Beekman, V. Chudoba, A.S. Fomichev, M.S. Golovkov, E.M. Gazeeva, L.V. Grigorenko, G. Kaminski, S.A.

Krupko, B. Mauyey, I.A. Muzalevsky, E.Yu. Nikolskii, Yu.L. Parfenova, A. Serikov, S.I. Sidorchuk, R.S. Slepnev, P.G. Sharov, G.M. Ter-Akopian, R.Wolski, and B. Zalewski. Current status of the new fragment separator acculinna-2 and the first-day experiments. *Eurasian journal of physics and functional materials*, 3(1):46–52, march 2019.

[70] A. A. Bezbakh, S. G. Belogurov, R. Wolski, E. M. Gazeeva, M. S. Golovkov, A. V. Gorshkov, G. Kaminski, M. Yu. Kozlov, S. A. Krupko, I. A. Muzalevsky, E. Yu. Nikolskii, E. V. Ovcharenko, R. S. Slepnev, G. M. Ter-Akopian, A. S. Fomichev, P. G. Sharov V. Chudoba, and V. N. Schetinin. A neutron spectrometer for experiments with radioactive beams on the acculinna-2 fragment separator. *Instruments and Experimental Techniques*, 61:631–638, 2018.

[71] H.G. Essel and N. Kurz. The general purpose data acquisition system mbs. *Nuclear Science, IEEE Transactions on*, 47:337–339, 05 2000.

[72] Fresco. http://www.fresco.org.uk/index.htm.

[73] O.F. Nemets. *Nucleonic Associations in Atomic Nuclei and Nuclear Reactions of Multinucleon Transfer*. Kiev, 1988. in Russian.

[74] W. W. Daehnick, J. D. Childs, and Z. Vrcelj. Global optical model potential for elastic deuteron scattering from 12 to 90 mev. *Phys. Rev. C*, 21:2253–2274, Jun 1980.

[75] D. Y. Pang, W. M. Dean, and A. M. Mukhamedzhanov. Optical model potential of $a = 3$ projectiles for $1p$-shell nuclei. *Phys. Rev. C*, 91:024611, Feb 2015.

[76] C.M. Perey and F.G. Perey. Compilation of phenomenological optical-model parameters 1969-1972. *Atomic Data and Nuclear Data Tables*, 13(4):293–337, 1974.

[77] Simone. http://aculina.jinr.ru/simone.html. accessed: 2014-01-31.

[78] National nuclear data center, brookhaven national laboratory. https://www.nndc.bnl.gov/.

[79] L.D. Landau and E.M. Lifshitz. *Mechanics: Volume 1*. Number 1. 1. Elsevier Science, 1982.

[80] I. S. Shapiro. Some problems in the theory of nuclear reactions at high energies. *Usp. Fiz. Nauk*, 92(8):549–582, 1967.

[81] P.G. Sharov, L.V. Grigorenko, A.N. Ismailova, and M.V. Zhukov. Pauli-principle driven correlations in four-neutron nuclear decays. *JETPh Lett.*, 110:5–14, 2019.

[82] W.R. Leo. *Techniques for Nuclear and Particle Physics Experiments: A How-to Approach*. Springer, 1994.

[83] Root:a data analysis framework. http://root.cern.ch. accessed 2014-01-31.

[84] Geant4: A simulation toolkit. https://geant4.web.cern.ch/. accessed august 15, 2019.

[85] Silicon strip detector calibration. http://er.jinr.ru/si_detector_calibration.html.

[86] I.A. Muzalevskii, V. Chudoba, S.G. Belogurov, D. Biare A.A. Bezbakh, A.S. Fomichev, S.A. Krupko, E.M.Gazeeva, M.S.Golovkov, A.V.Gorshkov, L.V.Grigorenko, G.Kaminski, O.Kiselev, D.A.Kostyleva, M.Yu.Kozlov, B.Mauyey, I.Mukha, E.Yu.Nikolskii, Yu.L.Parfenova, W.Piatek, A.M.Quynh, V.N.Schetinin, A.Serikov, S.I.Sidorchuk, P.G.Sharov, R.S.Slepnev, S.V.Stepantsov, A.Swiercz, P.Szymkiewicz, G.M.Ter-Akopian, R.Wolski, and B.Zalewski. Detection of the low energy recoil 3he in the reaction 2h(8he, 3he)7h. *Bulletin of the Russian Academy of Sciences: Physics*, 84:500–504, 2020.

[87] Ian J. Thompson. Coupled reaction channels calculations in nuclear physics. *Computer Physics Reports*, 7(4):167–212, 1988.

[88] I. Brida, Steven C. Pieper, and R. B. Wiringa. Quantum monte carlo calculations of spectroscopic overlaps in $a \leqslant 7$ nuclei. *Phys. Rev. C*, 84:024319, Aug 2011.

[89] Cenxi Yuan, Toshio Suzuki, Takaharu Otsuka, Furong Xu, and Naofumi Tsunoda. Shell-model study of boron, carbon, nitrogen, and oxygen isotopes with a monopole-based universal interaction. *Phys. Rev. C*, 85:064324, Jun 2012.

[90] L. V. Grigorenko, I. G. Mukha, C. Scheidenberger, and M. V. Zhukov. Two-neutron radioactivity and four-nucleon emission from exotic nuclei. *Phys. Rev. C*, 84:021303, Aug 2011.

[91] A. A. Bezbakh, V. Chudoba, S. A. Krupko, S. G. Belogurov, D. Biare, A. S. Fomichev, E. M. Gazeeva, A. V. Gorshkov, L. V. Grigorenko, G. Kaminski, O. A. Kiselev, D. A. Kostyleva, M. Yu. Kozlov, B. Mauyey, I. Mukha, I. A. Muzalevskii, E. Yu. Nikolskii, Yu. L. Parfenova, W. Piatek, A. M. Quynh, V. N. Schetinin, A. Serikov, S. I. Sidorchuk, P. G. Sharov, R. S. Slepnev, S. V. Stepantsov, A. Swiercz, P. Szymkiewicz, G. M. Ter-Akopian, R. Wolski, B. Zalewski, and M. V. Zhukov. Evidence for the first excited state of ^{7}H. *Phys. Rev. Lett.*, 124:022502, Jan 2020.

[92] I. A. Muzalevskii, A. A. Bezbakh, E. Yu. Nikolskii, V. Chudoba, S. A. Krupko, S. G. Belogurov, D. Biare, A. S. Fomichev, E. M. Gazeeva, A. V. Gorshkov, L. V. Grigorenko, G. Kaminski, O. Kiselev, D. A. Kostyleva, M. Yu. Kozlov, B. Mauyey, I. Mukha, Yu. L. Parfenova, W. Piatek, A. M. Quynh, V. N. Schetinin, A. Serikov, S. I. Sidorchuk, P. G. Sharov, N. B. Shulgina, R. S. Slepnev, S. V. Stepantsov, A. Swiercz, P. Szymkiewicz, G. M. Ter-Akopian, R. Wolski, B. Zalewski, and M. V. Zhukov. Resonant states in ^{7}H: Experimental studies of the ^{2}H(^{8}He,^{3}He) reaction. *Phys. Rev. C*, 103:044313, Apr 2021.

[93] L.V. Grigorenko, P.G. Sharov, R. Wolski, I.A. Muzalevskii, A.A. Bezbakh, V. Chudoba, A.S. Fomichev, I. Mukha, E. Yu. Nikolskii, G. M. Ter-Akopian, and M. V. Zhukov. Resonant states in ^{7}h. ii. theoretical background. *(to be submitted)*, 2023.

[94] M. S. Golovkov, L. V. Grigorenko, A. S. Fomichev, S. A. Krupko, Yu. Ts. Oganessian, A. M. Rodin, S. I. Sidorchuk, R. S. Slepnev, S. V. Stepantsov, G. M. Ter-Akopian, R. Wolski, M. G. Itkis, A. S. Denikin, A. A. Bogatchev, N. A. Kondratiev, E. M. Kozulin, A. A. Korsheninnikov, E. Yu. Nikolskii, P. Roussel-Chomaz, W. Mittig, R. Palit, V. Bouchat, V. Kinnard, T. Materna, F. Hanappe, O. Dorvaux, L. Stuttgé, C. Angulo, V. Lapoux, R. Raabe, L. Nalpas, A. A. Yukhimchuk, V. V. Perevozchikov, Yu. I. Vinogradov, S. K. Grishechkin, and S. V. Zlatoustovskiy. Correlation studies of the ^{5}H spectrum. *Phys. Rev. C*, 72:064612, Dec 2005.

[95] L. V. Grigorenko, T. D. Wiser, K. Mercurio, R. J. Charity, R. Shane, L. G. Sobotka, J. M. Elson, A. H. Wuosmaa, A. Banu, M. McCleskey, L. Trache, R. E. Tribble, and M. V. Zhukov. Three-body decay of ^{6}be. *Phys. Rev. C*, 80:034602, Sep 2009.

[96] L. V. Grigorenko and M. V. Zhukov. Continuum excitations of ^{26}O in a three-body model: 0^+ and 2^+ states. *Phys. Rev. C*, 91:064617, Jun 2015.

[97] E. Yu. Nikolskii, I. A. Muzalevskii, A. A. Bezbakh, V. Chudoba, S. A. Krupko, S. G. Belogurov, D. Biare, A. S. Fomichev, E. M. Gazeeva, A. V. Gorshkov, L. V. Grigorenko, G. Kaminski, M. Khirk, O. Kiselev, D. A. Kostyleva, M. Yu. Kozlov, B. Mauyey, I. Mukha, Yu. L. Parfenova, W. Piatek, A. M. Quynh, V. N. Schetinin, A. Serikov, S. I. Sidorchuk, P. G. Sharov, N. B. Shulgina, R. S. Slepnev, S. V. Stepantsov, A. Swiercz, P. Szymkiewicz, G. M. Ter-Akopian, R. Wolski, B. Zalewski, and M. V. Zhukov. ^{6}H states studied in the ^{2}H(^{8}He,^{4}He) reaction and evidence of an extremely correlated character of the ^{5}H ground state. *Phys. Rev. C*, 105:064605, Jun 2022.

[98] M. S. Golovkov, L. V. Grigorenko, A. S. Fomichev, S. A. Krupko, Yu. Ts. Oganessian, A. M. Rodin, S. I. Sidorchuk, R. S. Slepnev, S. V. Stepantsov, G. M. Ter-Akopian, R. Wolski, M. G. Itkis, A. A. Bogatchev, N. A. Kondratiev, E. M. Kozulin, A. A. Korsheninnikov, E. Yu. Nikolskii, P. Roussel-Chomaz, W. Mittig, R. Palit, V. Bouchat, V. Kinnard, T. Materna, F. Hanappe, O. Dorvaux, L. Stuttgé, C. Angulo, V. Lapoux, R. Raabe, L. Nalpas, A. A. Yukhimchuk, V. V. Perevozchikov, Yu. I. Vinogradov, S. K. Grishechkin, and S. V. Zlatoustovskiy. Observation of excited states in ^{5}H. *Phys. Rev. Lett.*, 93:262501, Dec 2004.

[99] I. Slaus, R.G. Allas, L.A. Beach, R.O. Bondelid, E.L. Petersen, J.M. Lambert, P.A. Treado, and R.A. Moyle. Quasifree processes in the 2h+3he interaction. *Nuclear Physics. A*, 286(1):67–88, Aug 1977.

[100] I. Angeli and K.P. Marinova. Table of experimental nuclear ground state charge radii: An update. *Atomic Data and Nuclear Data Tables*, 99(1):69 – 95, 2013.